A Quasi-Optical Astronomical Receiver.

A thesis submitted for the
degree of Doctor of Philosophy of
the University of London

by

James Christopher George Lesurf, B.Sc.(London)

Department of Physics
Queen Mary College
London.

February 1981

TELESCOPE BEAM PORT
(HIDDEN FACE)

FIXING
SCREWS

DOUBLER
PORT

MIXER COUPLING
RING

FIXING
SCREWS

MIXER
PORT

TUNING
MICROMETER

UKIRT SYSTEM-A DIPLEXER

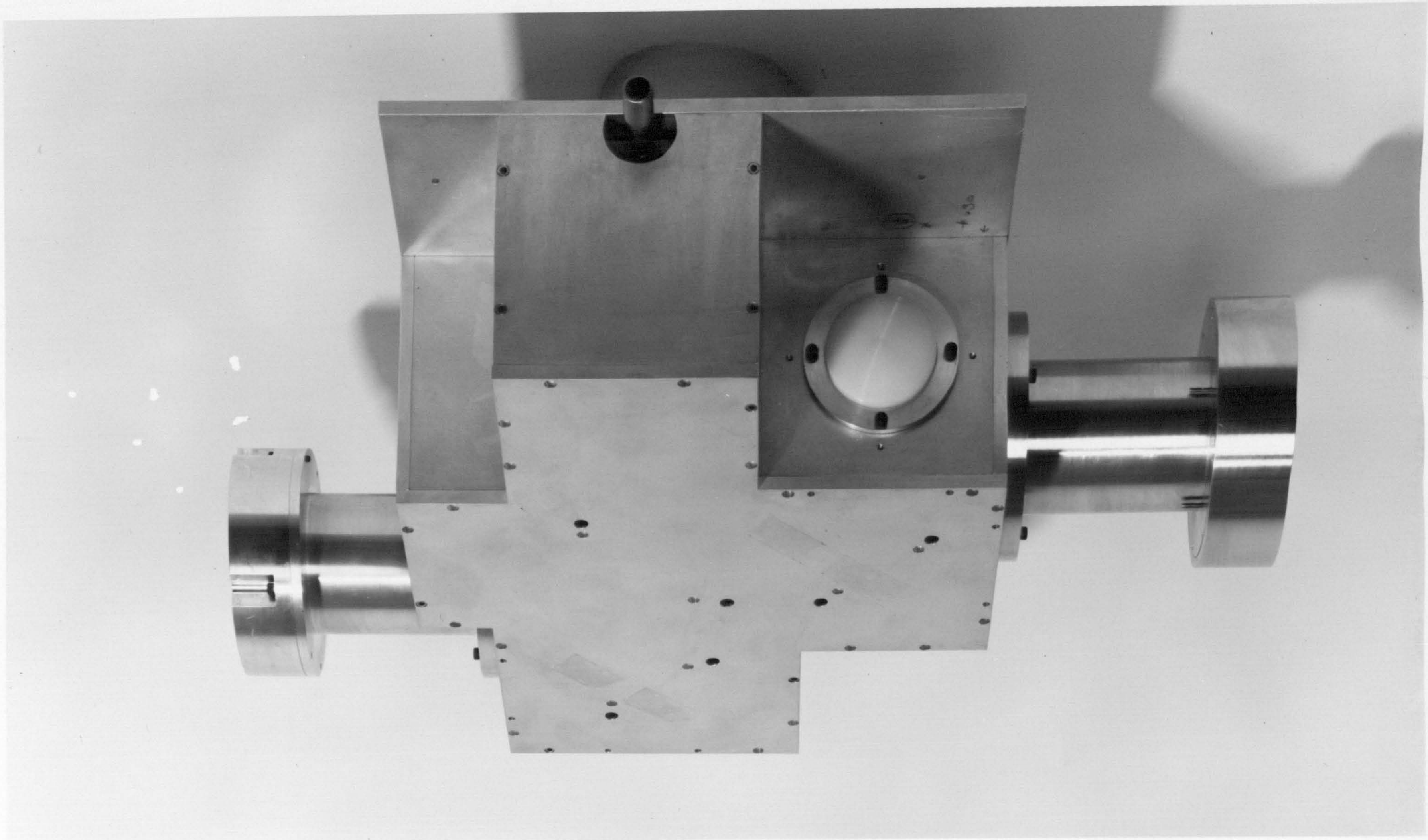

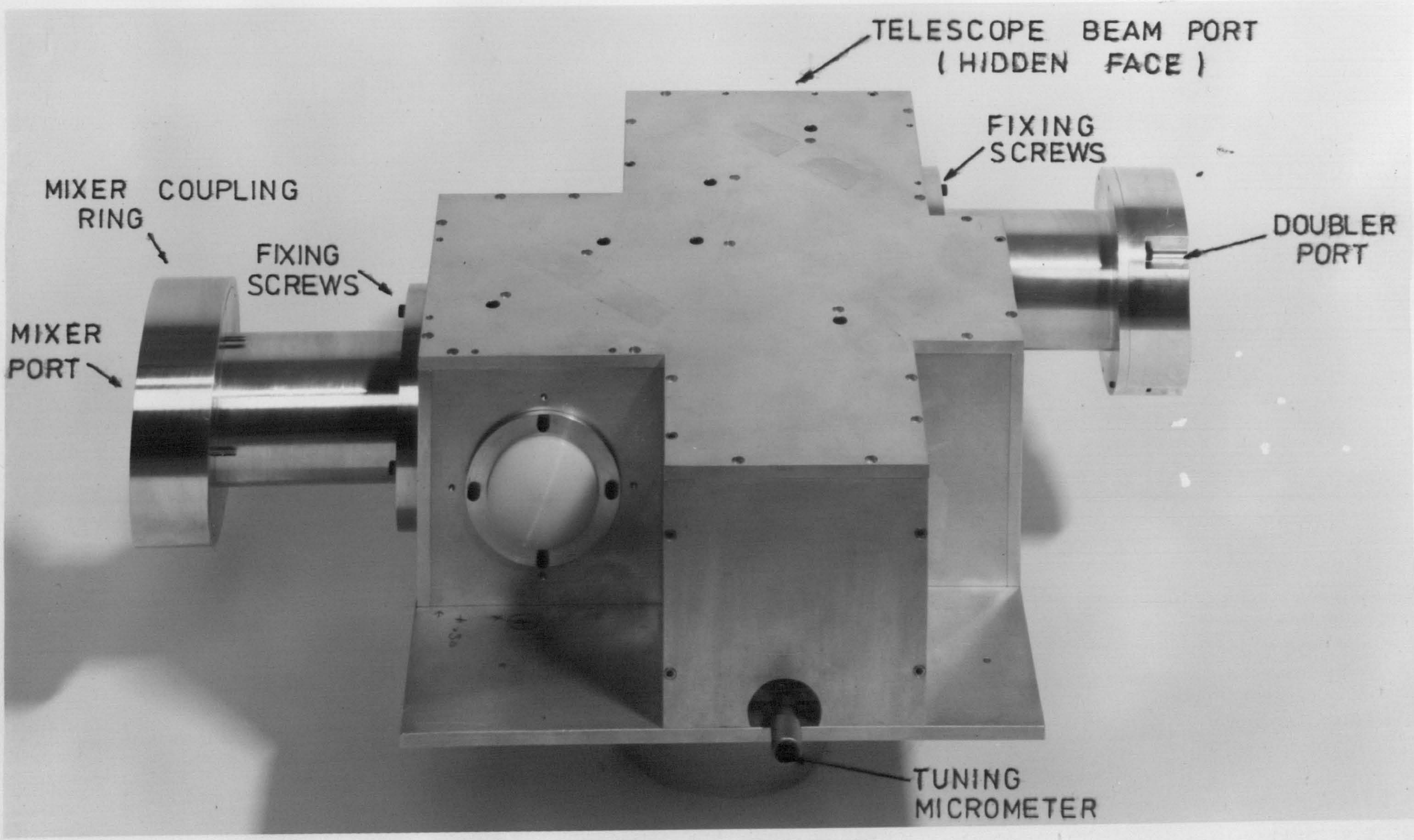

UKIRT SYSTEM-A DIPLEXER

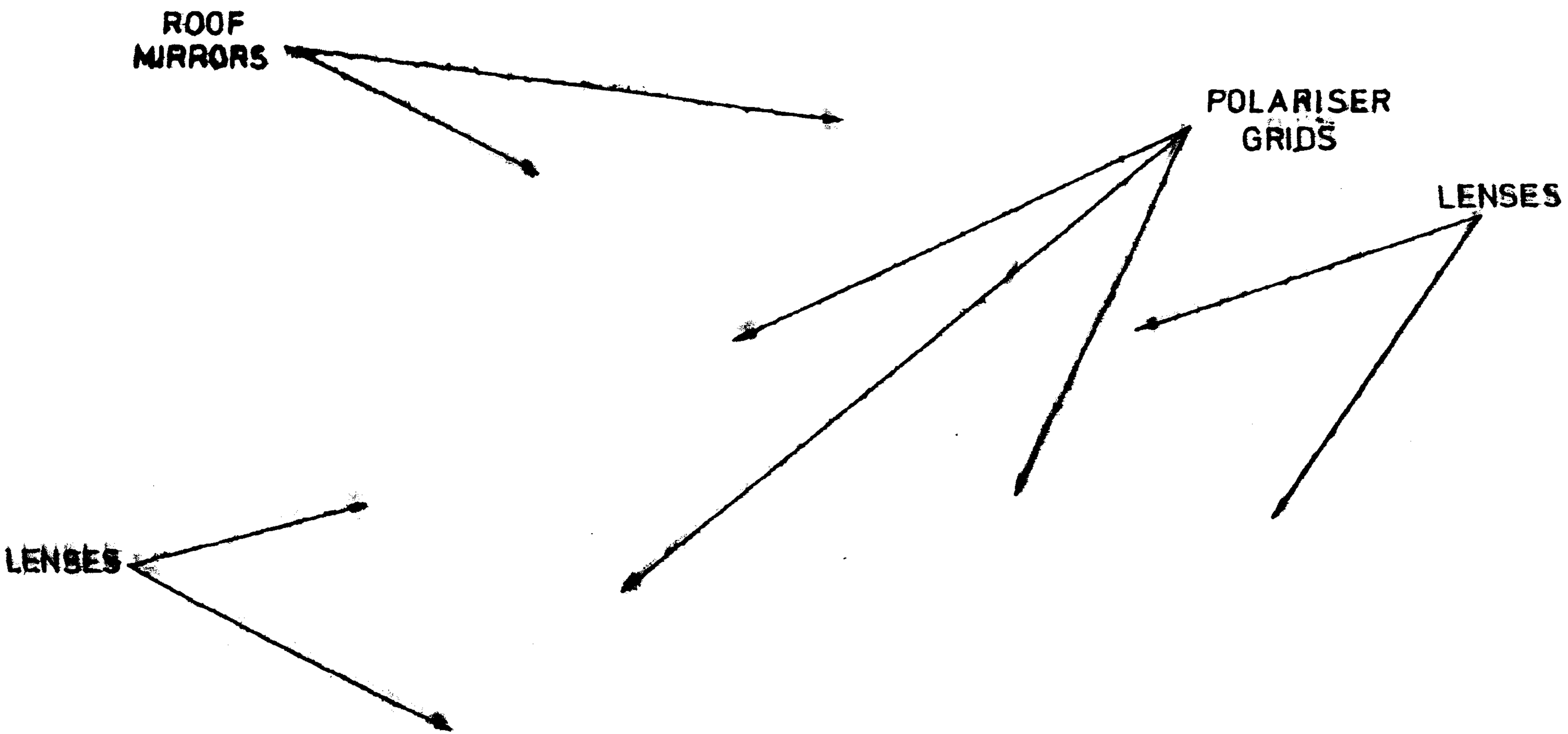
ROOF
MIRRORS
POLARISER
GRIDS
LENSES
LENSES

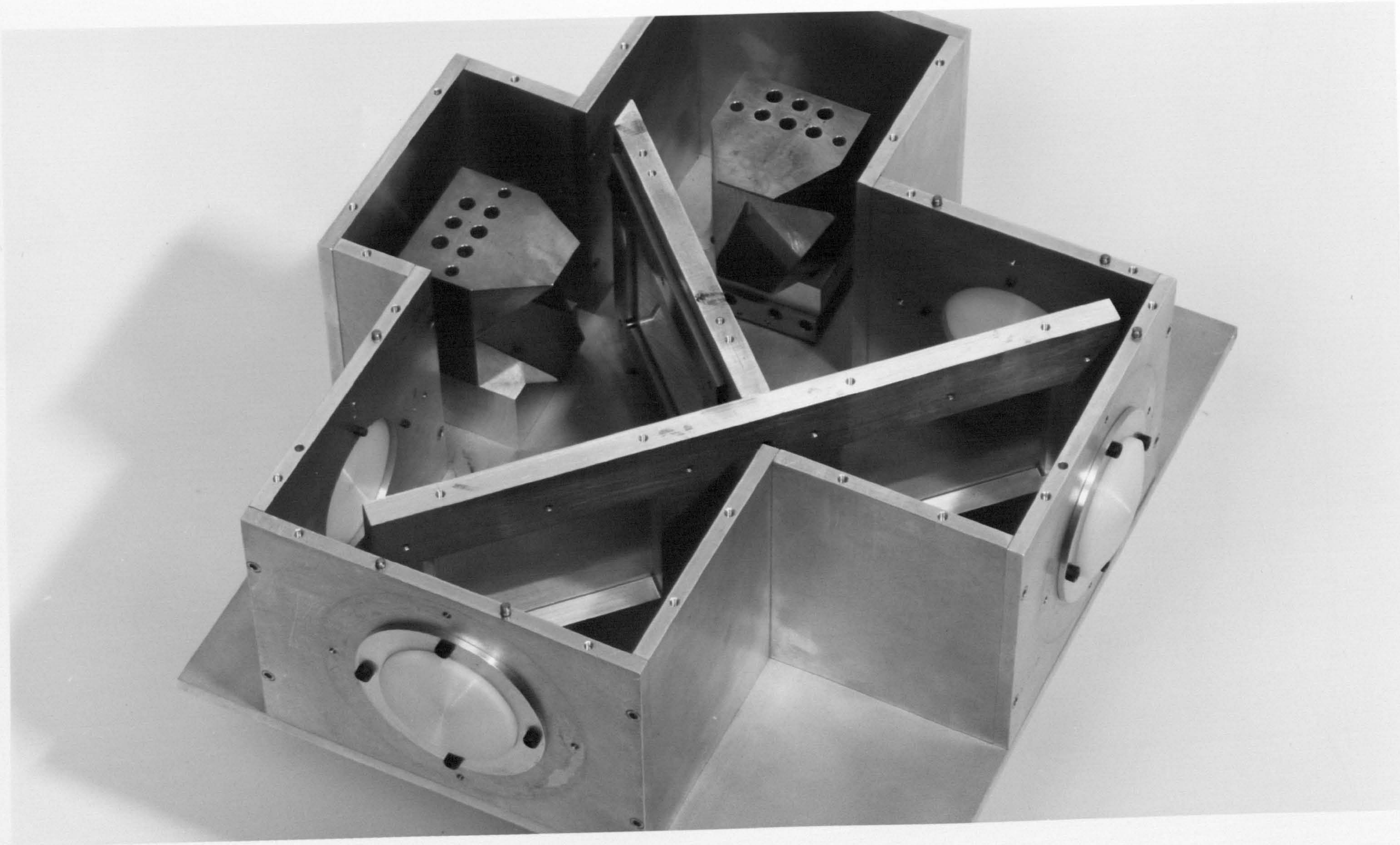

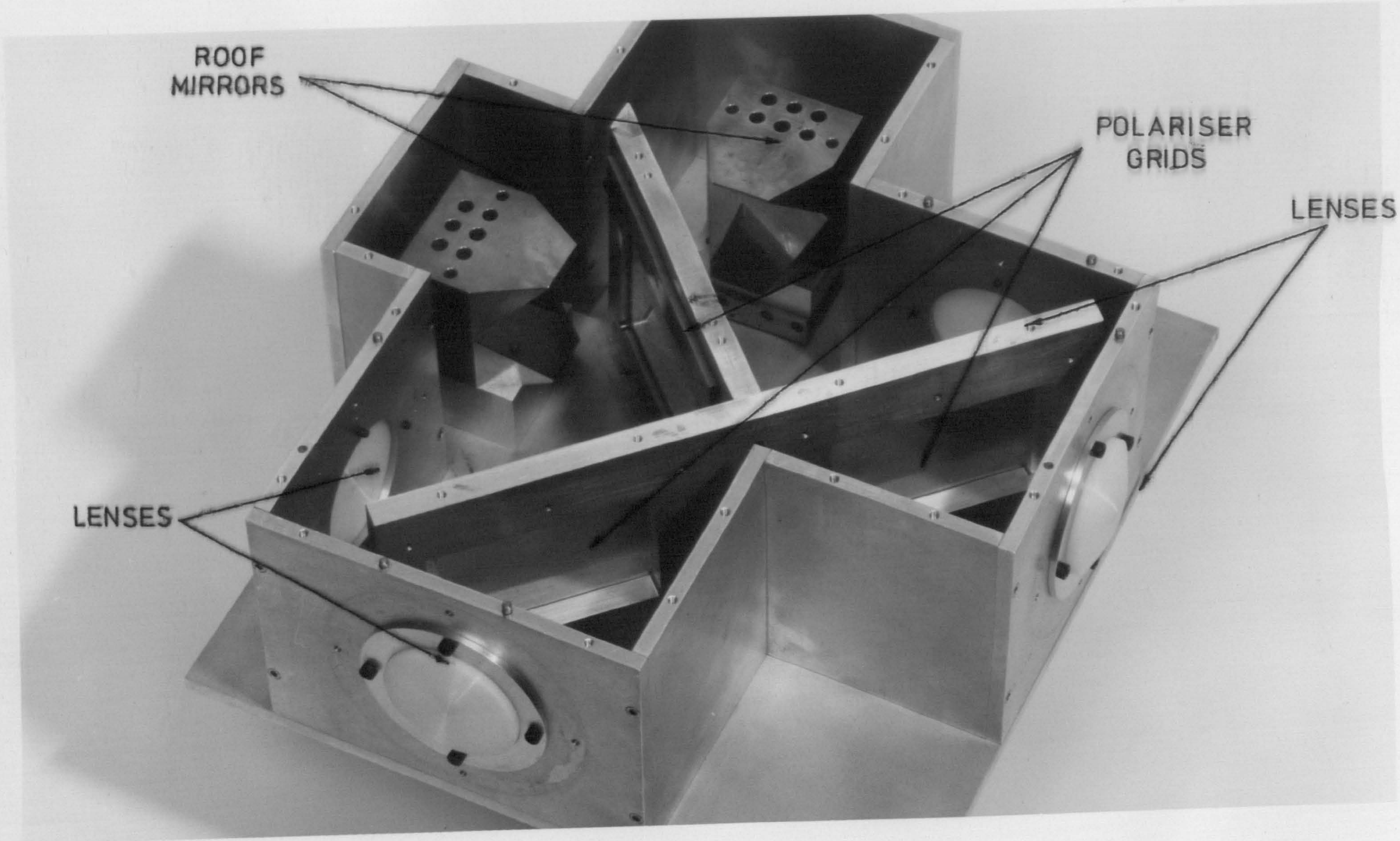
ROOF
MIRRORS
POLARISER
GRIDS
LENSES
LENSES

ABSTRACT.

This thesis describes the work undertaken in producing the passive radio-frequency section of a heterodyne receiver for use on the United Kingdom Infra-Red Telescope at signal frequencies in the 200-300 GHz range. This is a Quasi-Optical system, comprised of a Martin-Puplet polarising interferometer employed as a diplexer and the lenses and feed horns by which the diplexer was coupled to the telescope, local oscillator, and mixer.

The Gaussian beam-mode approach was employed to develop a theoretical basis for understanding the operation of such a system upon coherent paraxial beams. Quasi-Optical systems were then designed and their performance predicted by the application of this extension of Gaussian optics.

Two such systems were constructed and their performance determined by laboratory measurements to be as predicted. One of these systems was then installed on the telescope where it was shown to function as designed.

As part of the calibration and test routine on the telescope a number of astronomical measurements were made, including a determination of the apparent temperatures of the planets Jupiter and Saturn by a method different to that employed for results previously published.

The Quasi-Optical receiver was successfully calibrated and commissioned as a common-user instrument. As such it will continue to be used in a variety of astronomical research programs undertaken by various groups.

ACKNOWLEDGEMENTS

Above all others I must thank Professor D.H. Martin for all his advice and assistance. Without his help this thesis would never have been written. I am also grateful to Professor J.A. Bastin who acted as my supervisor during the first years of my graduate research.

Thanks are also due to all the technical staff of the Physics Department, both for their skill and for the enthusiasm with which they tackle difficult manufacturing problems.

Grateful thanks also to my parents for their unending encouragement and support.

Finally, I am endebted to the Science Research Council for a research studentship.

J.C.G.L.

List of Contents.

SECTION 1

INTRODUCTION

A heterodyne radio receiver is of the general form illustrated in Fig Ia.

In such a system the input signal, containing spectral information, is combined and mixed with a locally generated waveform to produce an output - generally at a lower frequency - which preserves the spectral information of the initial signal. This conversion of information to lower frequencies is useful for a number of reasons. For example, no adjustments are necessary to the intermediate frequency and spectral analysis sections of the system when it is desired to change the signal frequency to which the receiver is sensitive.

Where the filtering and analysis sections are complex this is a great practical advantage and for this reason the heterodyne receiver is widely employed even at relatively low frequencies (down to 100kHz). In addition, at very high frequencies amplification is generally impractical as the available amplifiers become increasingly noisy, insensitive, and band-limited as the frequency increases. Hence it is of advantage to convert received spectral information down into the frequency regions where good amplifiers are readily available.

At low frequencies(typically less than a few GHz)conventional wired circuitry may be employed throughout the receiver and the system might be as indicated in Fig Ib. Here the function of the diplexer is performed by the LC band-pass filters tuned to the signal, local oscillator, and intermediate frequencies. These ensure that all of the available signal and local oscillator power is conveyed to the mixer. i.e. none of the signal power is dissipated in the local oscillator circuitry, and vice-versa.

At higher frequencies, up to approximately 200GHz, wired-circuit

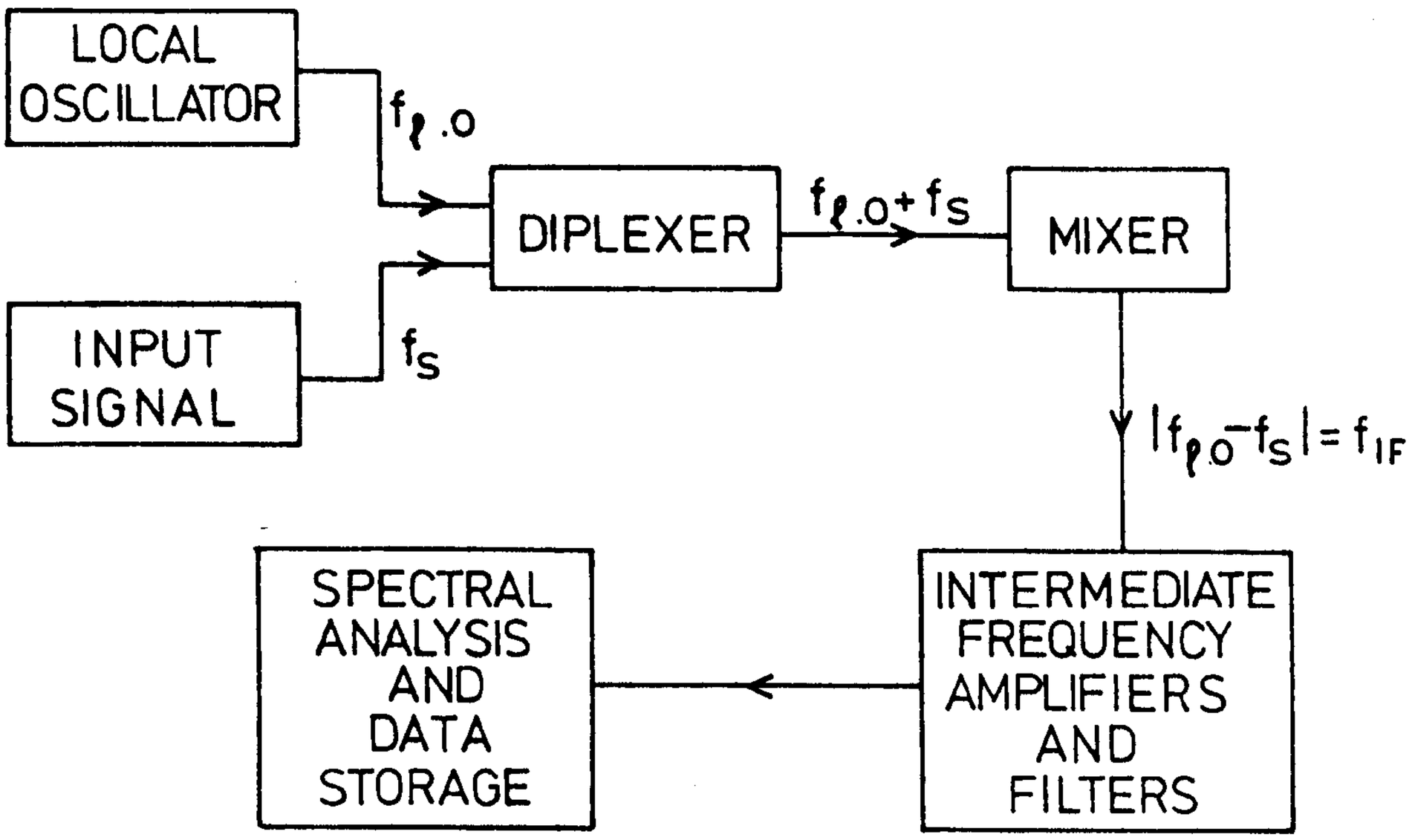

Fig. 1a.

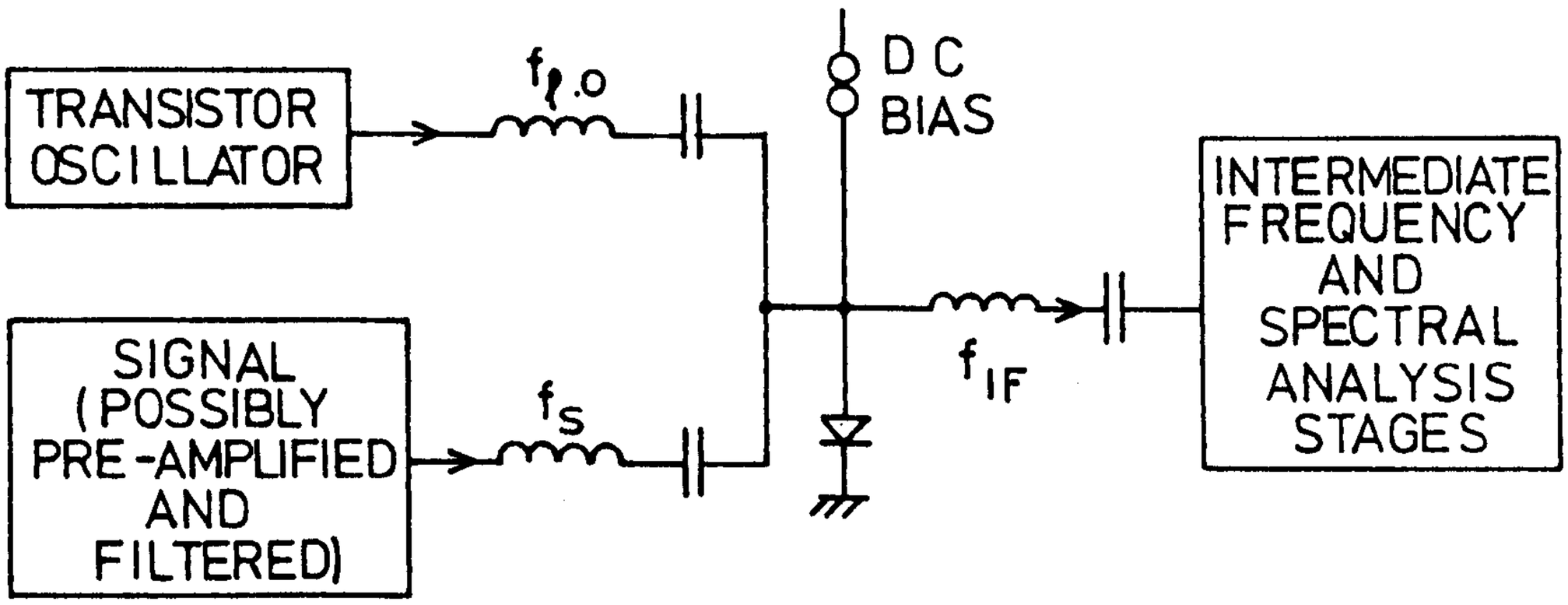

Fig. 1b.

Heterodyne receiver schematic.

techniques must be replaced with waveguide alternatives.

For example, the LC filters can be replaced by tuning stubs, posts, or irises, and the transistor oscillator by a klystron or a Gunn or impatt diode.

Receivers employing conventional waveguide methods have been used for many years and are well understood. However at the relatively high frequencies considered in this thesis(200 GHz and above) waveguide devices become inefficient due to the difficulties of accurately machining the small structures required and the increasing skin-impedance losses of metallic structures. It therefore becomes advantageous to replace waveguide devices with optical equivalents.

The central objective of the work described in this thesis was to design an effective receiver front-end for the 2-300 GHz frequency region which would prove to be robust and convenient to use. The system is hence based upon the application of optical rather than waveguide techniques.

1.2. Choice of diplexer form and method of analysis.

As one requirement of practical convenience the optical part of the system should not be unmanageably large, preferably the diameters of the optical components(and consequently the beam passing through them)should be no more than a few centimetres.

Geometrical optics depends upon the assumption that the radiation wavelength is insignificant in comparison with the sizes of the optical components. Here the components are no more than a few tens of wavelengths in diameter and so geometrical optics is inappropriate.

A less restrictive form of analysis is to be found in the methods of Gaussian-beam optics. Here the principle requirement is that the radiation may be considered as propagating along

paraxial beams whose angle of divergence or convergence, θ, is sufficiently small that we may regard $\theta = \sin(\theta) = \tan(\theta)$. (A more detailed consideration of this method will be given in Section 2.)

Gaussian optics has for some time been applied to the analysis of masers and resonator cavities and as a result of work discussed in this thesis it may be seen to be a powerful and effective method for the design and analysis of devices for use in the millimetre wavelength region. Along with some of the other forms of analysis employed during this work it frequently produces results similar to those obtained by conventional geometric optics(although marked differences occur in some situations). These various methods have therefore been gathered under the general title 'quasi-optics' and the receiver may as a consequence be described as being of a 'quasi-optical' form.

The use of quasi-optical devices in radio receivers is not in itself new. For example the Fabry-Perot resonator has been employed in the 100 GHz region and above(see, for example, Wannier et al, Rev. Sci. Instrum. 47 56 (1976)).

The Fabry-Perot, however, possesses a number of disadvantages which limit its performance in the millimetre-wavelength region. The metal meshes from which they are constructed are fragile and inherently lossy. In addition, Fabry-Perot's suffer from a form of loss known as 'walk-off'(Arnaud et al, IEEE MTT-22 486 (1974))which causes power to be coupled out of the beam. This reduces their throughput efficiency and degrades their frequency selectivity.

The problems encountered in the Fabry-Perot are a product of

its multi-pass, resonant method of operation and can be avoided by the use of a divice which is not of a multi-pass form. Such a device is the Michelson interferometer.

Erickson(IEEE MTT-25 865 (1977))has described the use of one form of the Michelson interferometer employed as a diplexer. However this device uses a mylar beamsplitter which limits the performance. The mylar film does not have a 50% reflectivity at any frequency and its reflectivity is strongly frequency dependent, relying upon constructive interference between the reflected waves from each of the film surfaces. The mylar also absorbes some of the incident radiation.

Payne and Wordman(Rev. Sci. Instrum. 49 1741 (1978))produced an improved diplexer by replacing the mylar with an array of thin parallel wires spaced the order of a half-wavelength apart. The exact spacing of the wires is carefully chosen to ensure that the grid reflects 50% of the incident radiation whose electric-vector is parallel to the wires.

Although this represents an advance over the system described by Erickson this form of diplexer is optimised only at one frequency as the grid's reflectivity is a function of the ratio between the wire-spacing and the radiation wavelength. There is also a small loss of power due to scattering from the array as the wire spacing approaches a wavelength.

These problems may be overcome by employing an interferometer of the Martin-Puplett polarising form(see Martin and Puplett, Infra. Phys. 10 105 (1969)). Here the beamsplitter is a wire-grid polariser. In such a polariser the wire seperation is very much smaller than a wavelength, hence its properties do not vary significantly over a wide range of frequencies.

The use of a polarising two-beam interferometer, and the analysis of the Michelson interferometer(and its derivatives) in terms of its operation upon paraxial beams regarded as Gaussian-mode sets has not been considered prior to the work contained in this thesis.

The choice of Gaussian-mode optics was made on the basis of selecting that form of analysis which promised to illuminate most elegantly the physics of paraxial-wave propagation within a beam of finite size.

In the past the analysis of Michelson interferometers has generally proceeded by the application of Geometric Ray Optics modified by a variety of techniques such as the Geometric Theory of Diffraction. Such an approach, whilst enabling the calculation of many desired results, does not always promote a clear appreciation of the physics of a given situation. Furthermore, such an approach frequently requires the use of techniques of numerical approximation which render calculation difficult.

Gaussian-mode optics, however, was found as a result of the work described in this thesis to offer a method by which results can be swiftly obtained in a manner which tends to clarify the nature of the underlying physics. This form of analysis may therefore be regarded as being most appropriate for an exploration of the optics of the millimeter and submillimeter wavelength region.

SECTION 2

METHODS OF ANALYSIS AND DESIGN

In this section the operation of the polarising interferometer and its use as a diplexer are explained - initially in terms of its action upon plane parallel beams of radiation.

Gaussian-beam optics is then introduced and applied to the analysis of a compact diplexer for which the assumption of plane parallel beams is inappropriate. Expressions are then derived for the diplexer's performance as a function of various parameters including the beam wavelength and diameter. The loss of local oscillator power and the telescope's antenna efficiency and beam pattern are then calculated.

2.1 General description of the Martin-Puplett Interferometer and its use as a diplexer.

The action of the interferometer may be illustrated by the use of Fig 2.

For the sake of simplicity the manner of operation may initially be considered in terms of its action upon plane parallel beams whose cross-sectional size is considerably greater than the radiation wavelength. Under these circumstances the beams can be represented by a single axial ray in the manner of geometric optics. This form of analysis is not suitable for a detailed consideration of a compact system but is adequate as a description of the interferometer's operation and the manner in which it may be employed as a diplexer.

Consider a plane polarised beam of frequency f_a which enters via input port a. This passes through a polariser, P1, which is aligned so as to transmit f_a without loss.

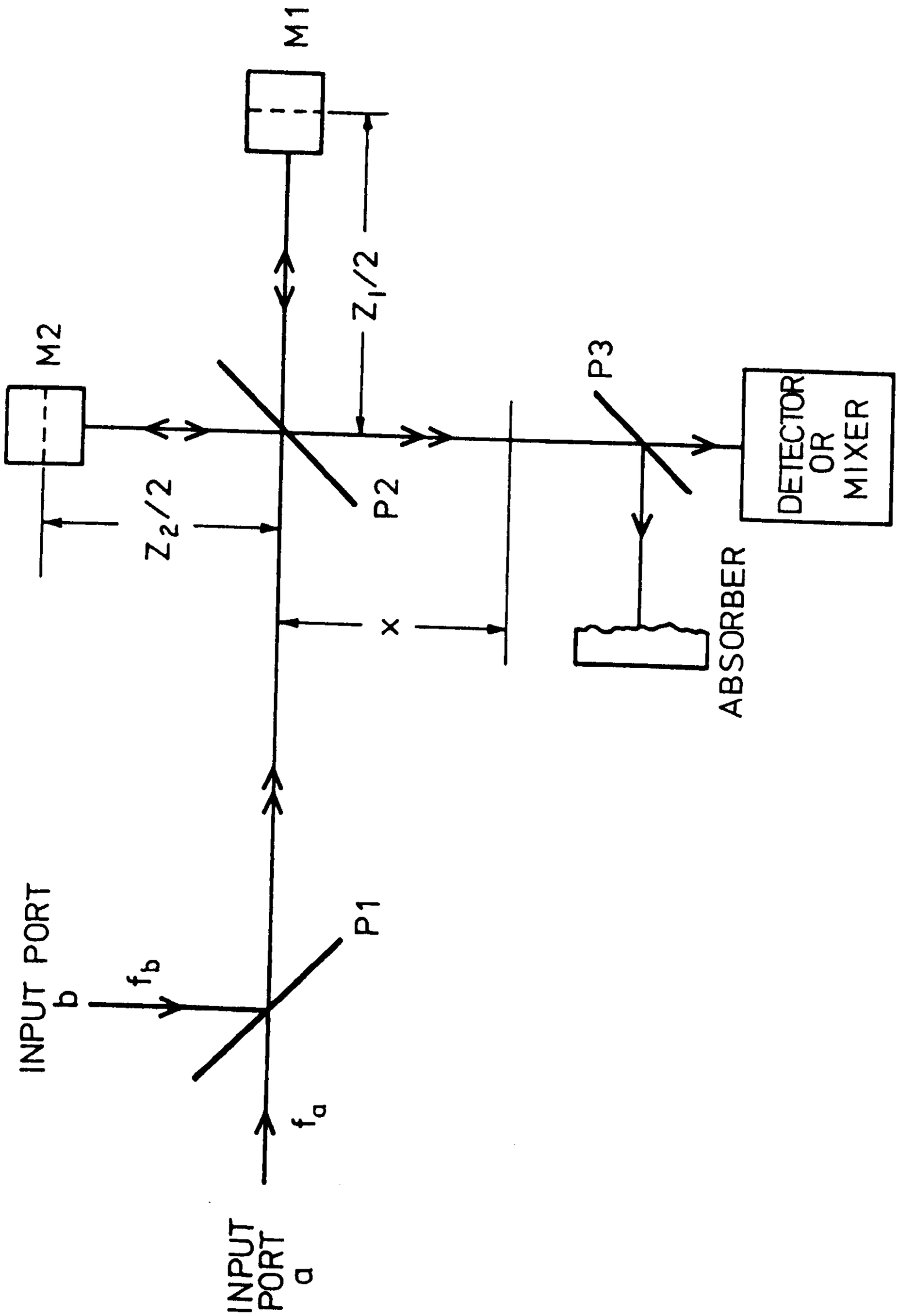

Fig. 2.
Interferometer schematic.

The polarisers, P1, P2, P3, are constructed from flat plane arrays of closely spaced parallel wires. Such a grid resolves incident radiation into two orthogonal plane polarised components, one of whose electric-vector is parellel to the wires. This component is reflected as if the polariser were a plane mirror whilst the other component is transmitted as if the polariser were absent.

The polarised beam next encounters the polariser P2 which is aligned with its wires at 45^{o} to the electric-vector of f_a as seen projected along the beam axis. Hence P2 splits f_a into two beams of equal magnitude which have orthogonal electric-vectors and propagate towards the two roof-mirrors, M1, and M2.

A roof-mirror consists of two plane mirrors at a mutual angle of 90^{o}. It possesses the property of rotating the plane of polarisation of an incident beam upon reflection. By placing the roof mirrors such that their roof-lines are 45^{o} to the electric-vectors of the incident beams it may be arranged that the incident and reflected beams are orthogonally polarised. This being so, the beam initially reflected by P2 will now be transmitted and vice-versa. The two beams may in this way be recombined and directed toward the polariser P3.

The polarisation of the recombined beam may be calculated from the sum of the two component electric-vectors.

These may conveniently be represented by $\underline{E1}$ and $\underline{E2}$ where

$$\underline{E1}(t,Z1,x) = \underline{e1}\ \mathrm{Sin}(2\pi f_a t - k_a(x + Z1)) \qquad (2.01)$$

$$\underline{E2}(t,Z2,x) = \underline{e2}\ \mathrm{Sin}(2\pi f_a t - k_a(x + Z2)) \qquad (2.02)$$

Here $\underline{e1}$, and $\underline{e2}$ represent the appropriate orthogonal unit vectors perpendicular to the direction of propagation, t represents the instant of time and x, Z1, and Z2 are as indicated in Fig 2. f_a represents the radiation frequency, and $k_a = 2\pi f_a/c$ where c

is the velocity of light in vacuo.

For simplicity it is assumed that $\underline{E1} = \underline{E2} = 0$ when $t = x = 0$.

If, therefore, we define Z1 and Z2 in terms of a mean path length, Z, and a path difference, D, such that

$$Z1 = Z - D/2 \quad ; \quad Z2 = Z + D/2$$

then the combined, time-dependent, electric vector, $\underline{a}$, may be expressed in the form

$$\underline{a} = (\underline{e1} + \underline{e2})\ \mathrm{Sin}(2\pi f_a t - k_a(x + Z))\mathrm{Cos}(-k_a D/2)$$
$$+ (\underline{e1} - \underline{e2})\ \mathrm{Cos}(2\pi f_a t - k_a(x + Z))\mathrm{Sin}(-k_a D/2) \qquad (2.03)$$

In general this represents an elliptically polarised wave, but when either $\mathrm{Cos}(-k_a D/2)$ or $\mathrm{Sin}(-k_a D/2)$ is equal to zero the wave is plane polarised in either the $(\underline{e1} + \underline{e2})$ or $(\underline{e1} - \underline{e2})$ direction.

If the beam represented by $\underline{a}$ is now directed onto another polariser, P3, the wires of which are parallel either to $(\underline{e1} + \underline{e2})$ or $(\underline{e1} - \underline{e2})$ it may be re-divided into two plane polarised beams whose amplitudes vary as a sinsunoidal function of $k_a D$. Thus it may be seen that variation of the path difference, D, generates interferometric modulation of the amplitude of the output beam. It is in this way the system is employed as the Martin-Puplett interferometer.

In order to examine the diplexing action of the system consider another coherent beam, f_b, entering via reflection from P1. This passes into the system along the same axis as f_a but the planes of polarisation of the two beams are perpendicular. As before an expression may be obtained for the output vector, $\underline{b}$

$$\underline{b} = (\underline{e1} + \underline{e2})\ \mathrm{Sin}(2\pi f_b t - k_b(x + Z))\mathrm{Sin}(-k_b D/2)$$
$$+ (\underline{e1} - \underline{e2})\ \mathrm{Cos}(2\pi f_b t - k_b(x + Z))\mathrm{Cos}(-k_b D/2) \qquad (2.04)$$

It should be noted that this expression differs from that obtained for $\underline{a}$; in particular, $\underline{a} \neq \underline{b}$ when $f_a = f_b$. This is because the input beams are orthogonally polarised.

If the amplitude of the ($\underline{e1}$ + $\underline{e2}$) component of the composite beam is represented by s, then

$$s = \mathrm{Sin}(2\pi f_a t - k_a(x + Z))\mathrm{Cos}(-k_a D/2) + \mathrm{Sin}(2\pi f_b t - k_b(x + Z))\mathrm{Sin}(-k_b D/2) \qquad (2.05)$$

A similar expression may be written for the amplitude of the beam in the ($\underline{e1}$ - $\underline{e2}$) plane, d, viz

$$d = \mathrm{Cos}(2\pi f_a t - k_a(x + Z))\mathrm{Sin}(-k_a D/2) + \mathrm{Cos}(2\pi f_b t - k_b(x + Z))\mathrm{Cos}(-k_b D/2) \qquad (2.06)$$

From these expressions it will be seen that if $\mathrm{Sin}(-k_a D/2) = \mathrm{Cos}(-k_b D/2) = 0$, d = 0 and s contains all the power of the input beams f_a and f_b. Similarly, if $\mathrm{Cos}(-k_a D/2) = \mathrm{Sin}(-k_b D/2) = 0$, then s = 0 and all the power entering in the beams f_a and f_b is contained in d.

The above conditions are equivalent to requiring that either

$$\mathrm{Cos}^2(-k_a D/2) + \mathrm{Sin}^2(-k_b D/2) = 2 \qquad (2.07)$$

or

$$\mathrm{Sin}^2(-k_a D/2) + \mathrm{Cos}^2(-k_b D/2) = 2 \qquad (2.08)$$

These expressions may be re-written as

$$\mathrm{Sin}(-\tfrac{1}{2}(k_a + k_b)D)\mathrm{Sin}(-\tfrac{1}{2}(k_a - k_b)D) = 1 \qquad (2.09)$$

and

$$\mathrm{Sin}(-\tfrac{1}{2}(k_a + k_b)D)\mathrm{Sin}(-\tfrac{1}{2}(k_b - k_a)D) = 1 \qquad (2.10)$$

From the above expressions, 2.05 to 2.10, it will be seen that, for an appropriate value of the path difference, D, the interferometer will act as a diplexer, directing all of the power contained by the input beams f_a and f_b towards a given exit port to which a mixer or power detector may be coupled.

In most cases of practical interest $|f_a - f_b| \ll f_a + f_b$, and this being so expressions 2.09 and 2.10 are approximately satisfied when

$$D \simeq \pi/|k_a - k_b| = \lambda/2 \qquad (2.11)$$

where λ is the wavelength of the difference frequency, $|f_a - f_b|$.

When the mixer is pumped by a local oscillator of frequency f_1 an output at an intermediate frequency, f, will be produced by input power to the mixer at a frequency of either $(f_1 + f)$ or $(f_1 - f)$. One of these may be selected as the signal frequency, the other is conventionally referred to as the image frequency.

Now any real local oscillator will generate noise over a wide range of frequencies centred about its nominal frequency of oscillation. The mixer is unable to distinguish between noise and a desired signal, and so any noise at the signal and image frequencies absorbed by the mixer will be combined with the signal, degrading the system performance.

From the symmetric nature of the interferometer, when D is chosen such that the desired signal and local oscillator power emerge in one plane of polarisation, the local oscillator noise at the signal and image frequencies will emerge orthogonally polarised to this plane.

At first sight it would seem that all that is required to prevent this noise from being absorbed in the mixer is to construct it in such a way as to be insensitive to the appropriate plane of polarisation. This being done, a polariser such as P3 appears redundant. Unfortunately, in practice the mixer may respond to some degree to both planes of polarisation, and even where the noise is not absorbed it may be reflected back into the optical system. Some of this may subsequently be re-reflected onto the mixer in such a way that its plane of polarisation is altered. This part of the noise power may then be absorbed.

Since, however, the wanted and unwanted powers are in orthogonal planes of polarisation they may be separated by the use of a polariser such as P3 and the unwanted noise directed onto a

suitable radiation absorber.

It should be noted that an output at a given intermediate frequency may be produced by power at the image frequency entering the system via the same input port as the signal. This may be prevented by an additional filter of some kind, placed in the signal beam, which transmits the signal frequency whilst rejecting the image. Such a device will require re-tuning when the frequency of operation is changed and may also be expected to lose some of the signal power.

The diplexer itself could be employed to perform the filtering action by a change of the path difference, D. This could be selected in order to prevent the image frequency power entering the signal input port from reaching the mixer whilst leaving the signal coupling unaffected. This approach is unsatisfactory for two reasons

a) The local oscillator power would now be shared equally between the two exit ports as it must emerge from the system with circular polarisation.

b) The image frequency noise from the local oscillator would emerge in the same plane of polarisation as the signal and would be combined with it by the mixer.

A more satisfactory alternative is to avoid the use of an image filter altogether and assess the image frequency contribution to the intermediate frequency output by modulating the local oscillator frequency. If, for example, the local oscillator frequency is increased by an amount, df, the input at $(f_1 + f)$ now produces output at a frequency $(f - df)$, whereas the input at $(f_1 + f)$ produces an output at $(f + df)$. It will be seen that the sign of the frequency shift in a component of the intermediate frequency spectrum depends upon whether the generating radio-

frequency power is at the signal or image frequency. Thus where the intermediate frequency output exhibits a recognisable spectral structure the changes produced by a shift in the local oscillator frequency make it possible to identify the signal and image contributions to the output.

Of necessity this method requires that the signal should exhibit a distinct spectral structure and that the intermediate frequency bandwidth should be sufficient to permit spectral analysis to resolve this structure at a fixed local oscillator frequency. In practice both of these conditions may be satisfied. Furthermore, in many cases a careful choice of the local oscillator frequency will ensure that the image frequency power is small in comparison with the wanted signal and hence the problem is avoided altogether.

2.2 The effect of a finite bandwidth upon diplexer performance.

In the concluding paragraphs of the previous section mention was made of the receiver's finite intermediate frequency bandwidth. Prior to this point it was assumed that the signal may be regarded as a single frequency. In reality the signal is a spectral distribution of power that, upon being mixed with the local oscillator, produces a similar distribution across a range of intermediate frequencies. This finite signal bandwidth must be taken into account when considering the detailed performance of the receiver. The way this may be done can be illustrated by reference to Fig 3. For a given set of conditions the ratio of the power entering via an input port to that emerging via a specific exit port may be defined as the coupling efficiency of the diplexer between those two ports. The variation in coupling efficiency as a function of frequency may then be defined as

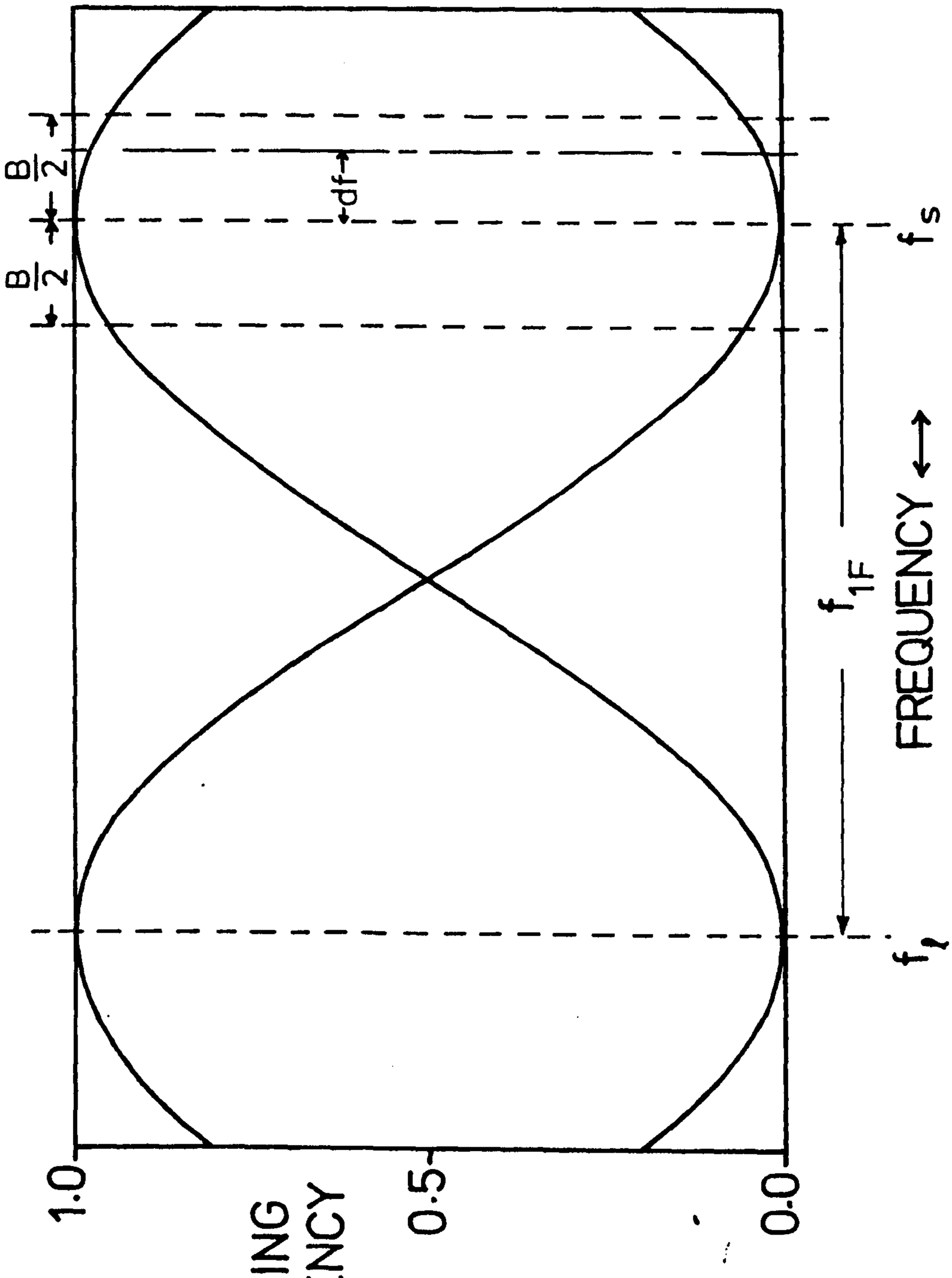
B/2
B/2
df
f_s
f_{1F}
FREQUENCY
f_2
1.0
0.5
0.0
COUPLING
EFFICIENCY
N

the frequency response of a particular input - output port pair.

The two sinusoids shown in Fig 3 represent the frequency response of a diplexer, each sinusoid representing the frequency response appropriate to a particular port pair. At a given exit port they represent the variation in coupling efficiency with frequency for each of the input ports.

That the frequency response is of this form may be seen by an examination of expressions 2.05 and 2.06.

Take, for example, 2.05. Here the amounts of the input beams f_a and f_b that emerge from the relevant exit port are

$$\mathrm{Sin}(2\pi f_a t - k_a(x + Z))\mathrm{Cos}(-k_a D/2)$$

and

$$\mathrm{Sin}(2\pi f_b t - k_b(x + Z))\mathrm{Sin}(-k_b D/2)$$

These expressions give the time-dependent amplitudes of the appropriate electric-vectors. By taking the time-averages of the squares of each expression we obtain the powers associated with the f_a and f_b components of the emergent beam. If these powers are then divided by the time-averaged values of the squares of the input amplitudes the resultant expressions are equivalent to the coupling efficiencies as defined above. If N_a and N_b represent the coupling efficiencies for the input beams f_a and f_b respectivly we may, therefore, write

$$N_a = \mathrm{Cos}^2(-k_a D/2) \qquad (2.12)$$

and

$$N_b = \mathrm{Sin}^2(-k_b D/2) \qquad (2.13)$$

Now it should be noted that the subscripts, a and b, do not necessarily denote different frequencies but different input ports. Hence if $f_a = f_b = f$, and $k_a = k_b = k$, we obtain

$$N_a = \mathrm{Cos}^2(-kD/2) \qquad (2.14)$$

and

$$N_b = \mathrm{Sin}^2(-kD/2) \qquad (2.15)$$

If the path difference, D, is obtained by regarding 2.11 as an equality, and k is such that

$$k = 2\pi(2nf + df)/c \qquad n = 1, 2, 3, ... \qquad (2.16)$$

then 2.14 and 2.15 become

$$N_a = \mathrm{Cos}^2((\pi df)/(2f)) \qquad (2.17)$$

and

$$N_b = \mathrm{Sin}^2((\pi df)/(2f)) \qquad (2.18)$$

where f and df are as shown in Fig 3, and df may be regarded as the deviation in frequency from that value at which f_a is perfectly coupled and f_b totally rejected from the exit port under consideration.

For a bandwidth, B, centered on the frequency 2nf we may write

$$N = \mathrm{Cos}^2((\pi B)/(4f)) \qquad (2.19)$$

and

$$R = \mathrm{Sin}^2((\pi B)/(4f)) \qquad (2.20)$$

Where N and R represent the coupling efficiencies at the extreme high and low frequency limits of the bandwidth, $\pm$ B/2. The symbol R is used in expression 2.20 to indicate that in this case we are concerned with the rejection of an unwanted noise component. R is defined as the rejection figure of the diplexer at the extreme ends of the passband. In the ideal situation, R approaches zero whilst N, the coupling efficiency for the desired signal and local oscillator power, should approach unity.

From 2.19 and 2.20 it will be appreciated that both N and R are impaired by the finite bandwidth, although when the bandwidth is small in comparison with the mean intermediate frequency(which is equivalent to the frequency, f)the effect may be insignificant.

In the case of the receiver discussed in this thesis the choice of mixer diode and its associated amplifiers determined that the intermediate frequency should lie in the range 3.8 to 4.2 GHz. The bandwidth of the system was limited to approximately 100 MHz by the autocorrelator employed for spectral analysis.

Putting f = 4 GHz, and B = 0.1 GHz into 2.19 and 2.20 we obtain the values N = 0.9996, and R = 0.00038(-34db). Hence in this case we may regard N = 1, and R = 0 for most purposes.

The above analysis was undertaken on the assumption that the diameters of the beams of radiation passing through the interferometer were sufficiently large in comparison with the wavelength that they could be regarded as plane parallel. When this condition is not met a different form of analysis must be employed. In the following section basic Gaussian-beam theory is discussed, and in section 2.4 this is applied to an investigation of the behaviour of a compact diplexer.

2.3 Basic Gaussian-mode optics.

Gaussian-mode optics has developed principally as a result of work undertaken on the propagation in lasers and resonant cavities of paraxial beams of radiation. A beam may be regarded as paraxial if the large majority of the radiative energy in the beam propagates along a set of directions whose angles of divergence or convergence from a common axis, θ, are sufficiently small that $\theta \simeq \mathrm{Sin}(\theta) \simeq \mathrm{Tan}(\theta)$.

Initially, Fox and Li(Bell Sys. Tech. J. 40 435 (1961))and Boyd and Gordon(Bell Sys. Tech. J. 40 489 (1961))determined the mode structures of paraxial beam resonators by a consideration of the effects of diffration. The concept of wave beams, introduced

by Goubau and Schwering(IRE Trans. AP-9 248 (1961)), was then applied to the analysis of spherical mirror cavities by Boyd and Kogelnik(Bell Sys. Tech. J. 41 1347 (1962)). It was this work which led to the development of Gaussian-beam optics.

Where a beam of radiation is represented by a scalar potential, u, this potential is required to satisfy the scalar wave equation

$$\nabla^2 u + k^2 u = 0 \qquad (2.21)$$

(Where $k = 2\pi/\lambda$)

For the field describing a paraxial beam propagating in essentially the z-direction in a Cartesian system of co-ordinates we may write

$$u = \chi(x,y,z)\exp(-jkz) \qquad (2.22)$$

where
$$\frac{\partial^2 \chi}{\partial z^2} << \frac{\partial^2 \chi}{\partial x^2} + \frac{\partial^2 \chi}{\partial y^2} \qquad (2.23)$$

Expression 2.23 may be regarded as a consequence of the definition of a paraxial beam given earlier. Alternatively, 2.23 itself may be chosen as the condition which must be satisfied in order that a beam may be considered paraxial.

Combining 2.22 and 2.23 we obtain

$$\frac{\partial^2 \chi}{\partial x^2} + \frac{\partial^2 \chi}{\partial y^2} - 2jk\frac{\partial \chi}{\partial z} = 0 \qquad (2.24)$$

By reference to Kogelnik and Li(Proc. IEEE 54 1312 (1966)) it may be shown that the solutions of this differential equation are of the form

$$\chi_{mn} = (w_o/w) \cdot E \cdot H_m(x\sqrt{2}/w) \cdot H_n(y\sqrt{2}/w) \cdot \exp(-j(kZ - \phi) - r^2((1/(w^2)) + (jk/2R))) \qquad (2.25)$$

Where H_m and H_n are Hermite polynomials of degree m and n respectively, and

$$\phi = (m + n + 1)\text{Arctan}((\lambda Z)/(\pi w_o^2)) \qquad (2.26)$$

$$w^2 = w_o^2(1 + ((\lambda Z)/(\pi w_o^2)^2) \qquad (2.27)$$

$$R = Z(1 + ((\pi w_o^2)/(\lambda Z))^2) \tag{2.28}$$

$$r^2 = x^2 + y^2 \tag{2.29}$$

and E is a complex coefficient which determines the total energy contained in the beam.

Many of the most important properties of this solution may be illustrated by what is conventionally referred to as the fundamental mode solution, m = n = 0. This is a function of Gaussian form

$$\mathcal{X} = (w_o/w) \cdot E \cdot \exp\left[-j(kZ - \phi) - r^2\left(\frac{1}{w^2} + \frac{jk}{2R}\right)\right] \tag{2.30}$$

The properties of which are illustrated in Figs 4 and 5.

The radial amplitude distribution shown in Fig 4 possesses a Gaussian profile with the parameter, w, describing the distance from the beam axis at which the beam amplitude is 1/e 'th of the axial value. w is conventionally referred to as the amplitude-beam radius and varies as a function of position along the beam axis. Due to the hyperbolic nature of this variation w reaches a minimum at a particular position along the beam. This position is called the beam-waist and the value of w at this position is defined to be, w_o, the beam-waist radius.

For convenience, distances along the beam axis, Z, are referred to an origin located at the beam-waist. This usage has already been exploited to simplify the forms of expressions 2.25 to 2.30.

At a given value of Z the phase difference between a point on the beam axis and one a distance, r, from the axis is given by

$$\exp(-r^2(jk/(2R)))$$

Hence R(Z) may be regarded as the radius of curvature of the beam's phasefront at a distance, Z, from the beam-waist.

For a higher-order mode(i.e. m or n $\neq$ 0)w may be regarded as

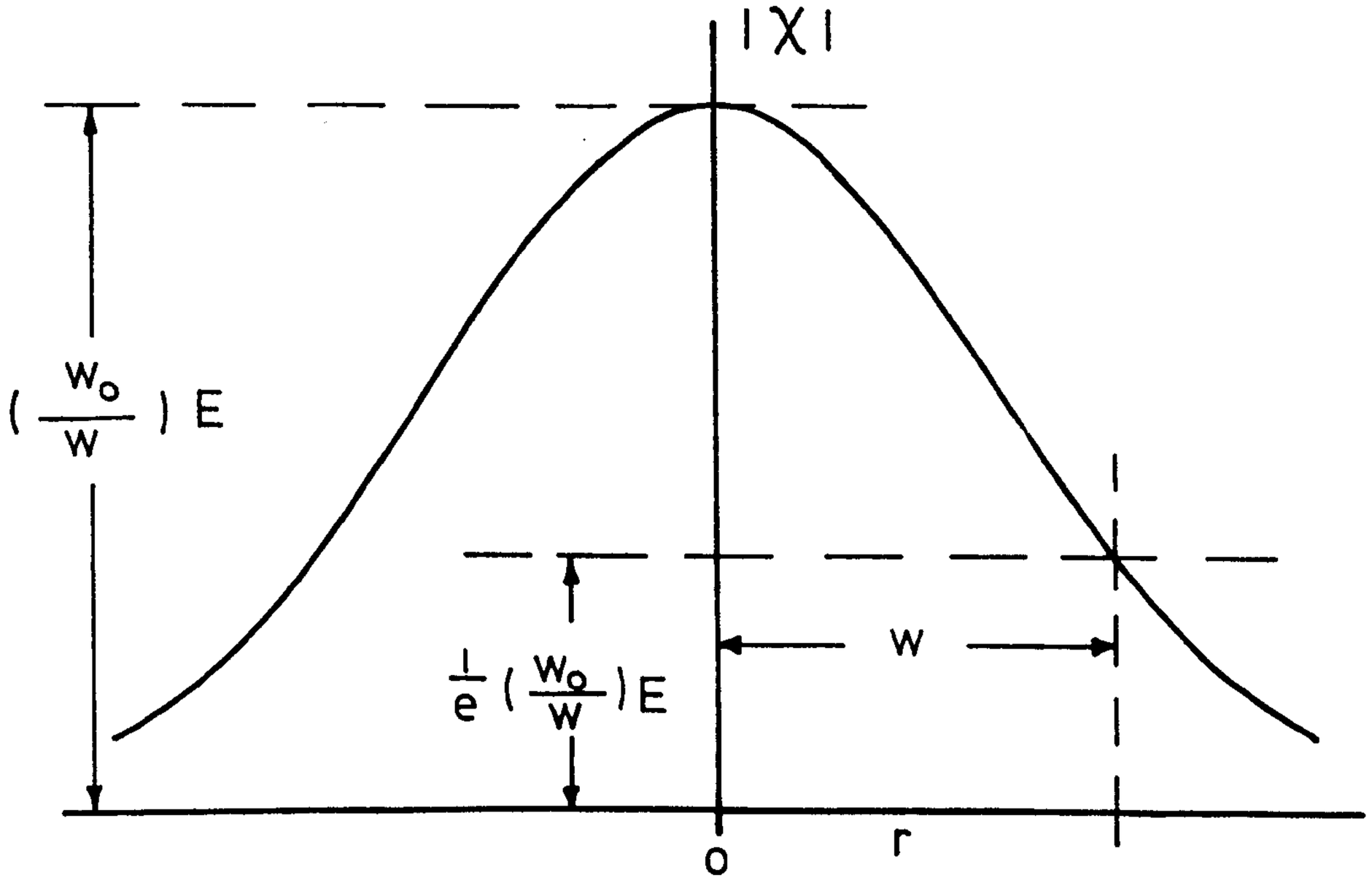

Fig. 4.
Radial amplitude distribution of a fundamental mode beam.

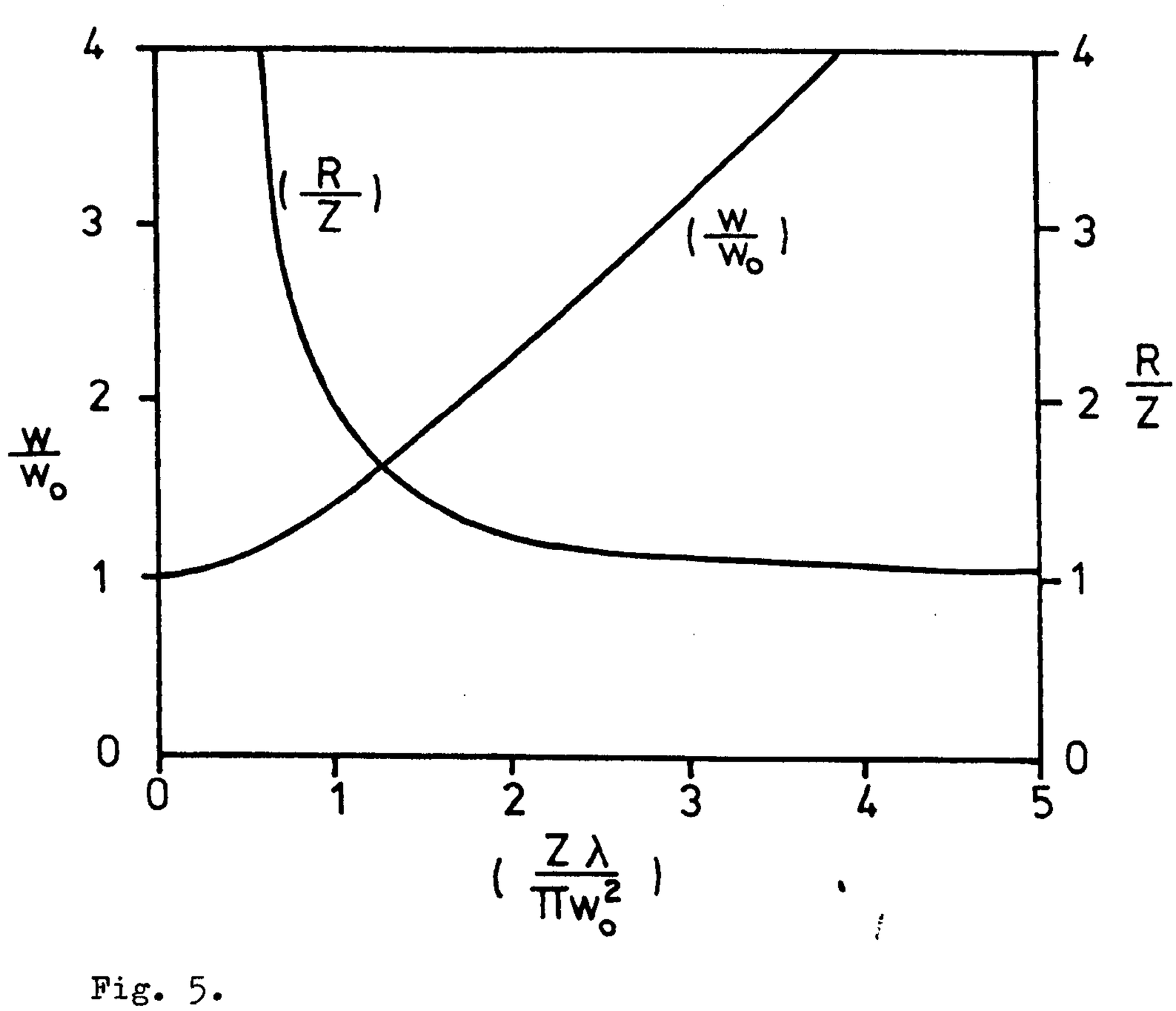

Fig. 5.
Normalised variation in R and w along the beam axis.

the scale-size of an amplitude distribution whose shape does not alter during propagation along the z-direction. An examination of 2.25 indicates that the variation of w and R as functions of Z does not depend upon m or n. Hence w and R may be regarded as the beam-size and radius of curvature irrespective of mode numbers. Furthermore, any linear superposition of functions of the form 2.25 also represents a solution of 2.24. Hence where a paraxial beam can be described by such a linear superposition of modes, sharing a common beam-waist size and position, w and R describe the variation in size and radius of curvature of the composite beam.

The component modes of such a composite beam may be referred to as a mode set.

Expressions 2.25 and 2.30 are in terms of a Cartesian system of co-ordinates, but in may cases possessing circular symmetry the use of cylindrical co-ordinates is more appropriate. In such cases 2.25 may be replaced by an expression of the form

$$\psi = E \cdot \left(\frac{r\sqrt{2}}{w}\right)^s \cdot L_p^s\left(\frac{2r^2}{w^2}\right) \cdot \exp(-j(kZ - \phi) - r^2((1/w)^2 + (jk)/(2R))) \quad (2.31)$$

where $$\phi = (2p + s + 1)\text{Arctan}\left(\frac{\lambda Z}{\pi w_o^2}\right) \quad (2.32)$$

and L_p^s is a generalised Laguerre polynomial with radial mode number, p, and angular mode number, s.

The definitions of the Hermite and generalised Laguerre polynomials and a list of some low-order examples are given in appendix A.

We may now make use of the expressions given above to study the coupling of power between optical systems.

Consider the situation illustrated in Fig 6. Here two optical

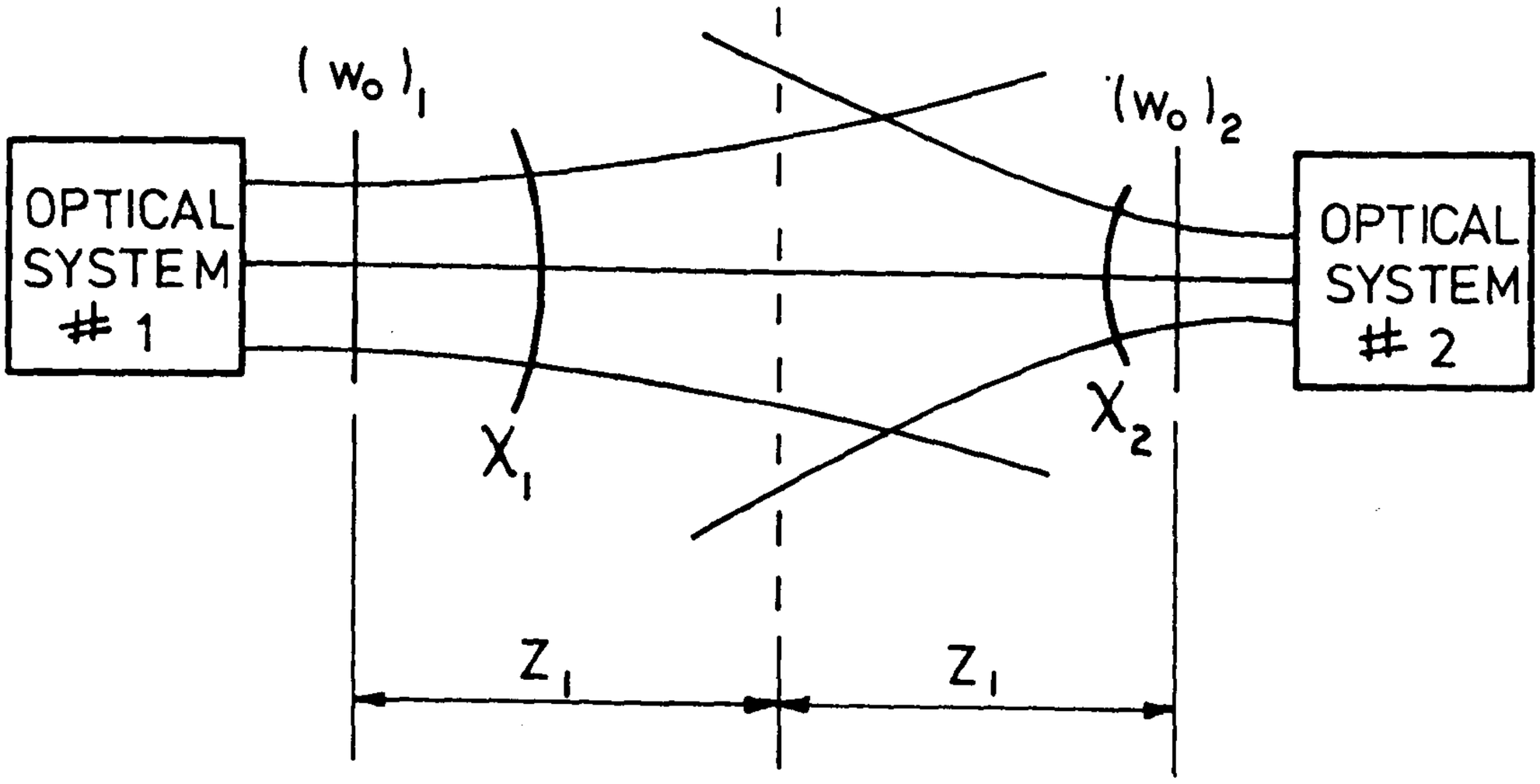

Fig. 6.
Gaussian coupling.

arrangements produce beam patterns described by expressions of the form $\chi(x,y,z)$ where each beam is paraxial to a common axis, z.

The amplitude coupling, C, between these beams is of the form(Kogelnik, Proc. Symp. Quasi-Opt., Polytech. Press, Brooklyn (1964) pg 333)

$$C = \int_{-\infty}^{\infty}\int_{-\infty}^{\infty} \chi_1^*(x,y,Z_1)\,\chi_2(x,y,Z_2)\,dx\,dy \qquad (2.33)$$

in Cartesian co-ordinates.

In cylindrical co-ordinates the appropriate expression is of the form

$$C = \int_{0}^{\infty} 2\pi r\,\chi_1^*(r,Z_1)\,\chi_2(r,Z_2)\,dr \qquad (2.34)$$

When considering the general properties of C we may employ the formalism

$$C_{pq} = \langle \chi_p^* \mid \chi_q \rangle \qquad (2.35)$$

where p = 1, q = 2; or, p =2, q = 1

irrespective of the co-ordinate system.

Since it must be true that for any physically realized system C is single-valued it follows that $C \neq C(Z_1,Z_2)$ where Z_1 and Z_2 are independent variables. Hence, for a given value of Z, the choice of coupling plane is irrelevant. This result is more formally proved by Arnaud(Beam and Fibre Optics, Academic Press, New York (1976) pg 75)

In rectangular co-ordinates we may write

$$\chi_p(x,y) = \chi_p(x)\,\chi_p(y) \qquad (2.36)$$

and

$$\chi_p(x) = \sum_{p=0}^{\infty} A_{mp}\,\chi_{mp}(x) \qquad (2.37)$$

$$\chi_p(y) = \sum_{p=0}^{\infty} B_{mp}\,\chi_{mp}(y) \qquad (2.38)$$

and $\chi_{mp}(x)$, $\chi_{mp}(y)$ are of the form

$$\chi_{mp}(x) = \left(\frac{2}{\sqrt{\pi}w.2^m.m!}\right)^{\frac{1}{2}} . H_m\left(\frac{x\sqrt{2}}{w}\right)$$

$$. \exp(-x^2((1/w)^2 + (jk)/(2R))) \qquad (2.39)$$

Note that χ_{mp} has been normalised such that

$$\langle \chi_{mp}^* | \chi_{mp} \rangle = 1 \qquad (2.40)$$

A_{mp} and B_{mp} are complex coefficients which determine the amplitude and phase of the m'th mode function's contribution at the coupling plane.

Since $\chi_p(x)$ and $\chi_p(y)$ are orthogonal we may write

$$C = C(x) . C(y) \qquad (2.41)$$

where $$C(x) = \langle \chi_p^*(x) | \chi_p(x) \rangle \qquad (2.42)$$

and $$C(y) = \langle \chi_p^*(y) | \chi_p(y) \rangle \qquad (2.43)$$

Combining 2.42 and 2.43 with 2.37 and 2.38 we obtain

$$C(x) = \sum_{m=0}^{\infty} \sum_{n=0}^{\infty} A_{mp}^* A_{nq} \langle \chi_{mp}^*(x) | \chi_{nq}(x) \rangle \qquad (2.44)$$

$$C(y) = \sum_{m=0}^{\infty} \sum_{n=0}^{\infty} B_{mp}^* B_{nq} \langle \chi_{mp}^*(y) | \chi_{nq}(y) \rangle \qquad (2.45)$$

Defining

$$C_{mpnq}(x) \equiv \langle \chi_{mp}^*(x) | \chi_{nq}(x) \rangle \qquad (2.46)$$

$$C_{mpnq}(y) \equiv \langle \chi_{mp}^*(y) | \chi_{nq}(y) \rangle \qquad (2.47)$$

we may write

$$C_{mpnq}(x) = \left(\frac{2}{\pi w_p w_q 2^{(m+n)} m! n!}\right)^{\frac{1}{2}}$$

$$. \int_{-\infty}^{+\infty} H_m(x\sqrt{\alpha^2}) . H_n(x\sqrt{\beta^2}) . \exp(-sx^2)\, dx \qquad (2.48)$$

and a similar expression for C(y), where

$$s = (1/w_p)^2 + (1/w_q)^2 + (jk/2)((1/R_q) - (1/R_p)) \quad (2.49)$$

$$\alpha = (2/w_p^2) \quad (2.50)$$

$$\beta = (2/w_q^2) \quad (2.51)$$

From an examination of 2.48 it will be appreciated that if (m + n) is odd the integrand is an odd function of x and the coupling integral is zero. Hence no coupling occurs between odd and even modes. The integral in 2.48 has been solved(see, for example, Erdyli, et al. Tables of Integral Transforms, Vol 1 Bateman Manuscript Proj. McGraw-Hill New York 1954)and may be expressed in terms of a finite hypergeometric series.

If m and n are even

$$C_{mpnq} = (-\tfrac{1}{2})^{(u+v)} \cdot (2/(w_p w_q s))^{\frac{1}{2}} \cdot \frac{(2u + 2v)!}{(u+v)!((2u)!(2v)!)^{\frac{1}{2}}} \cdot \frac{(s - \alpha)^v (s - \beta)^u}{s^{(u+v)}} \cdot F\left[-v, -u; -v-u+\tfrac{1}{2}, \frac{s(s - \alpha - \beta)}{(s - \alpha)(s - \beta)}\right] \quad (2.52)$$

where m = 2v ; n = 2u, and F is the hypergeometric series

$$F(a,b;c,z) = 1 + \frac{ab}{c} z + \frac{a(a+1)b(b+1)}{c(c+1)2!} z^2 + \ldots \quad (2.53)$$

Where m and n are odd

$$C_{mpnq} = (-\tfrac{1}{2})^{(u+v)} \cdot (2/(w_p w_q s))^{(3/2)} \cdot \frac{(2u + 2v + 1)!}{(u+v)!((2u+1)!(2v+1)!)^{\frac{1}{2}}} \cdot \frac{(s - \alpha)^v (s - \beta)^u}{s^{(u+v)}} \cdot F\left[-v, -u; -v-u-\tfrac{1}{2}, \frac{s(s - \alpha - \beta)}{(s - \alpha)(s - \beta)}\right] \quad (2.54)$$

where m = 2v + 1 ; n = 2u + 1, and F is as before.

As has been shown by Kogelnik(ibid)the above expressions lead to fairly simple forms for the lowest order coupling coefficients. For convenience we may omit the subscripts

p and q such that, $C_{mn} = C_{mpnq}$.

In this form some of the lowest order coupling coefficients may be listed as

$$C_{00} = (2/(w_p w_q s))^{\frac{1}{2}}$$

$$C_{20} = C_{00}/\sqrt{2}\,.\,((w_p/w_q)C_{00}^2 - 1)$$

$$C_{02} = C_{00}/\sqrt{2}\,.\,((w_q/w_p)C_{00}^2 - 1)$$

$$C_{22} = (1/C_{00})(C_{00}^6 + C_{02}C_{20})$$

$$C_{11} = C_{00}^3$$

$$C_{13} = \sqrt{3}\,.\,C_{00}^2 C_{02}$$

$$C_{31} = \sqrt{3}\,.\,C_{00}^2 C_{20}$$

etc...

It should be noted that the coupling coefficients quoted above and defined in 2.52 and 2.54 are one-dimensional. If, therefore, each of the beams γ_1 and γ_2 is represented as the summation of one-dimensional modes, γ_p or γ_q, as indicated by 2.36 to 2.38 the coupling coefficient in each dimension is, from expressions 2.44 to 2.47

$$C(x) = \sum_{m=0}^{\infty}\sum_{n=0}^{\infty} A_{mp}^{*} A_{nq} C_{mpnq}(x) \qquad (2.55)$$

$$C(y) = \sum_{m=0}^{\infty}\sum_{n=0}^{\infty} B_{mp}^{*} B_{nq} C_{mpnq}(y) \qquad (2.56)$$

where C_{mpnq} is as given by 2.52 or 2.54 .

The overall coupling coefficient is then obtained from 2.41 .

The above analysis is based upon Cartesian co-ordinates, but when a system is dealt with in terms of cylindrical co-ordinates the amplitude coupling coefficient can be obtained in a similar way(Kogelnik, ibid).

Once the amplitude coupling coefficient has been determined the coupling efficiency, N, is given by

$$N = C \,.\, C^{*} \qquad (2.57)$$

The above method of analysis may be applied quite generally to the coupling of power between optical systems.

In the following section this method is developed to examine the propagation of power through the diplexing interferometer. In sections 2.5 and 2.6 the Gaussian-mode beam approach is applied to the coupling of devices to the diplexer's input and output ports.

2.4 Gaussian-mode analysis of the Martin-Puplett Interferometer.

In section 2.1 the behaviour of the polarising interferometer was investigated in terms of its action upon plane parallel beams. In this section the interferometer's action upon compact beams is determined by considering the beams as Gaussian-mode sets.

Expressions 2.03 and 2.04 indicate the time-dependent amplitude and orientation of the vectors $\underline{a}$ and $\underline{b}$ which represent the electric-vectors associated with coherent plane parallel beams that have passed through the interferometer after entering via input ports a and b respectively.

In this section we replace the sinusoidal wave of the form

$$\gamma = \mathrm{Sin}(2\pi ft - kZ)$$

with Gaussian-mode sets.

i.e. in Cartesian co-ordinates

$$\gamma_p(x,y,z) = \left[\sum_{m=0}^{\infty} X_{mp}\,\gamma_{mp}(x,z)\right]\left[\sum_{m=0}^{\infty} Y_{mp}\,\gamma_{mp}(y,z)\right]\exp(-jkz) \qquad \ldots(2.58)$$

where γ_{mp} represents the m'th mode and X_{mp} and Y_{mp} determine the relative phase and amplitude of each mode's contribution to the composite beam.

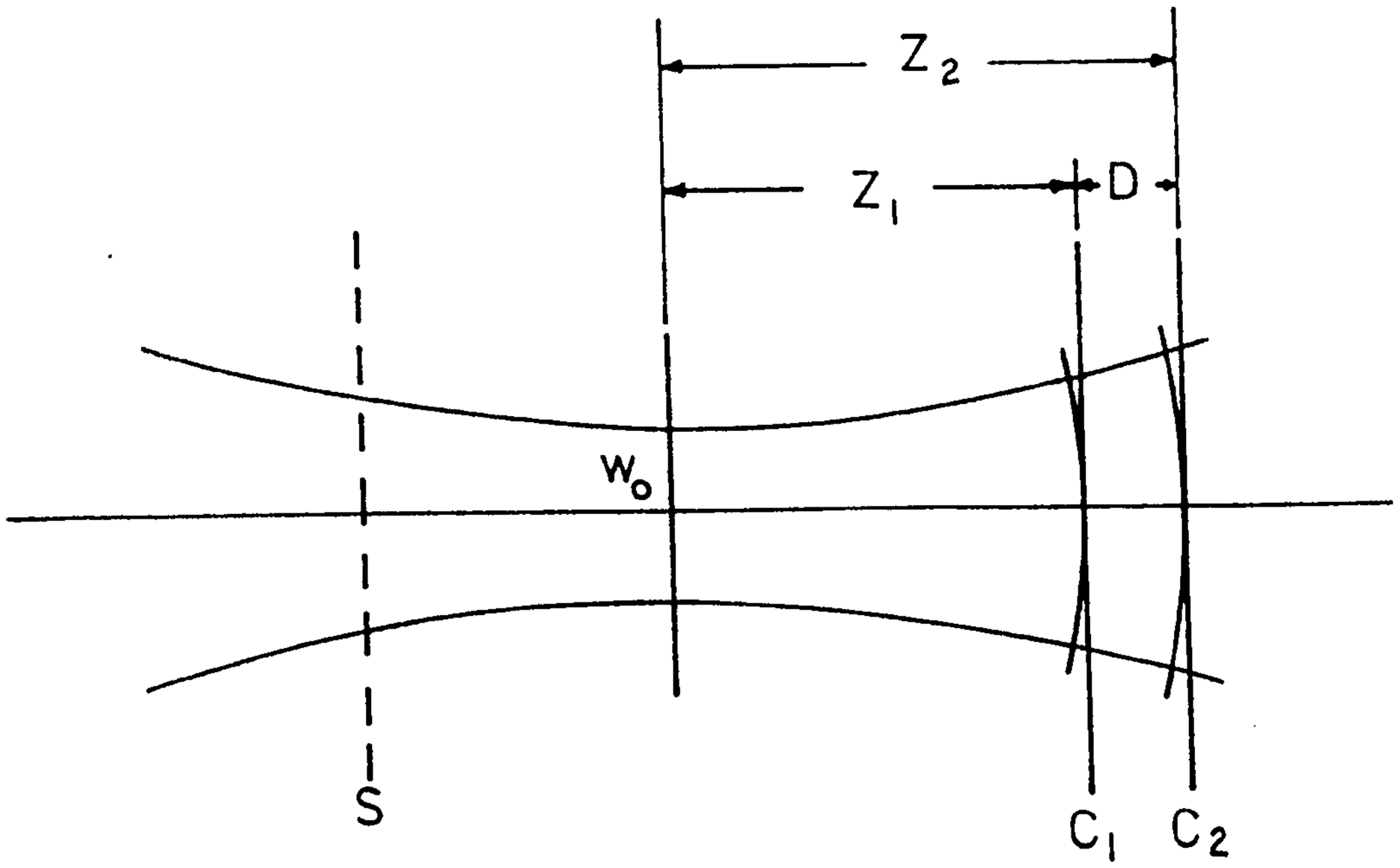

Fig. 7a.

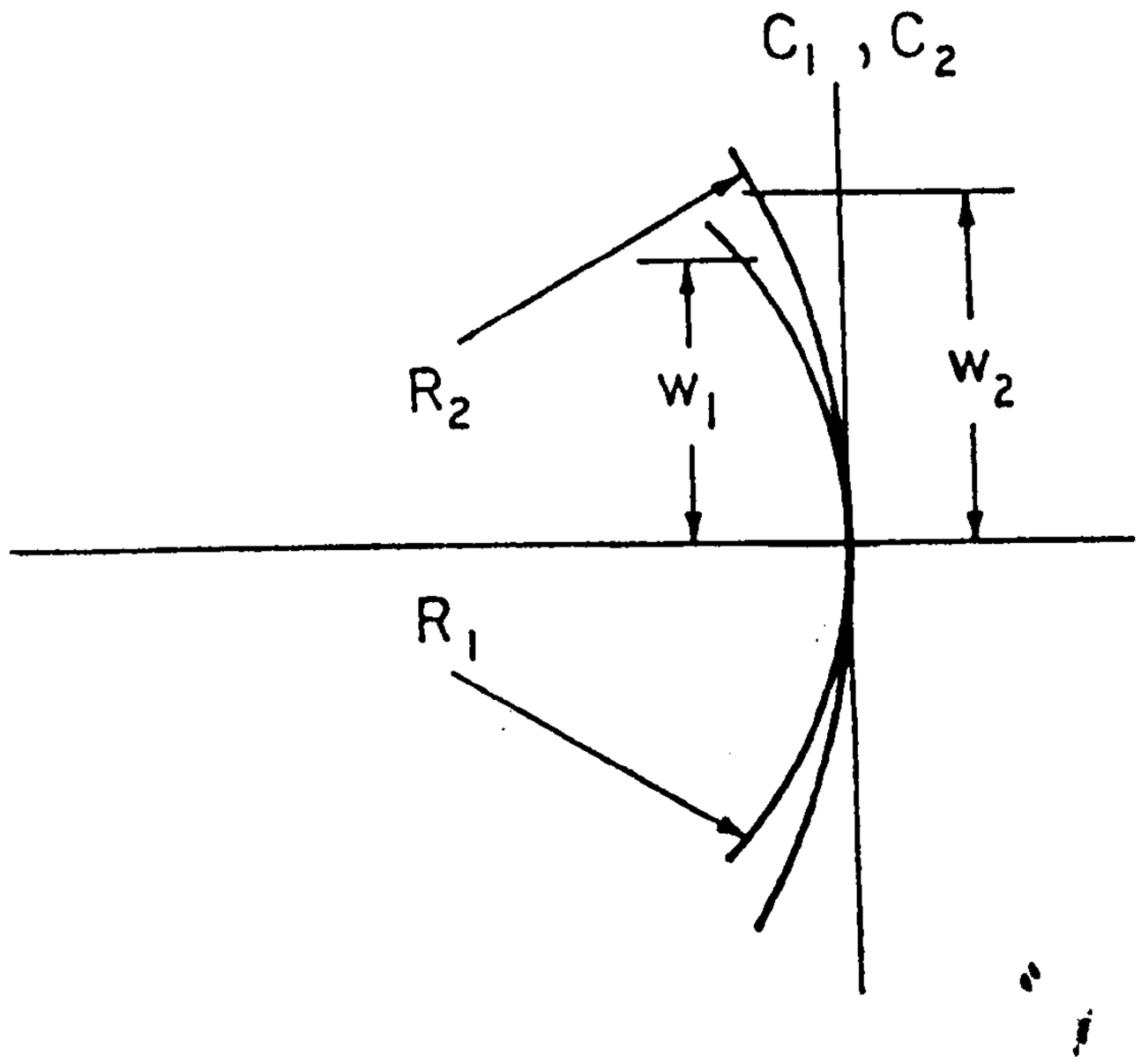

Fig. 7b.

Gaussian recombination.

The manner in which the interferometer acts upon such a beam may be illustrated by Figs 7a and 7b. An input beam, ψ_p, is divided into two equal parts, ψ_1, and ψ_2, by a beamsplitter at S. The two beams differ in amplitude and plane of polarisation from ψ_p but have the same radial amplitude and phase distribution. As they also possess the same beam-waist size and position as ψ_p they can be described by the same mode-set.

The two beams are re-combined at a plane that is at a distance Z_1 from the beam-waist of ψ_1 and Z_2 from the beam-waist of ψ_2. This recombination plane may be looked upon as the superposition of the planes C_1 and C_2 in a single mode set given by ψ_p.

The composite wave-function at this plane, Ψ_p, will therefore be of the form

$$\underline{\Psi}_p(x,y,Z_1,Z_2) = \underline{g1} \cdot \tfrac{1}{2}(\psi_p(x,y,Z_1) - (2p-3)\psi_p(x,y,Z_2)) + \underline{g2} \cdot \tfrac{1}{2}(\psi_p(x,y,Z_1) + (2p-3)\psi_p(x,y,Z_2)) \quad (2.59)$$

$$p = 1, 2$$

where $\underline{g1}$ and $\underline{g2}$ are orthogonal unit vectors that lie in planes equivalent to those defined by ($\underline{e1}$+$\underline{e2}$) and ($\underline{e1}$-$\underline{e2}$) in expressions 2.03 and 2.04. The subscript, p, denotes the port by which ψ_p enters the interferometer. The factors, $\frac{1}{2}$, included in the above expressions are required in order to ensure that the relative magnitudes of the input and output beams are correct.

The two beams produced by the polariser at S are orthogonally polarised and each has an amplitude $\sqrt{\frac{1}{2}}\psi_p$ - i.e. each contains half the power of ψ_p. These are recombined to produce an output resolved into two planes at 45° to the electric-vectors of ψ_1 and ψ_2. The contribution of each beam into a given plane is therefore $\frac{1}{2}\psi_p$. Hence the presence of the factors of $\frac{1}{2}$.

When $Z_1 = Z_2$ the interferometer has no net effect upon Ψ_p. Under these conditions it will be seen that g1 and g2 are arranged such that a beam entering via port p emerges with its electric-vector parallel to gp.

If Ψ_p is resolved into two plane polarised components by the use of a polariser arranged with its wires parallel to g1 or g2 the amplitudes of the resultant beams can be expressed by the scalar Ψ_{pq} where

$$\Psi_{pq}(x,y,Z_1,Z_2) = \tfrac{1}{2}(\Psi_p(x,y,Z_1) + T_{pq}\Psi_p(x,y,Z_2)) \quad (2.60)$$

$$T_{pq} = (2q-3)(2p-3) \quad (2.61)$$

and the parameter q defines the exit port from which the whole of Ψ_p emerges when $Z_1 = Z_2$ and $p = q$.

The ratio of the powers associated with the output beam Ψ_{pq} and the input beam Ψ_p may be defined as the coupling efficiency, N_{pq}, such that

$$N_{pq} = \frac{\langle \Psi^*_{pq} | \Psi_{pq} \rangle}{\langle \Psi^*_p | \Psi_p \rangle} \quad (2.62)$$

To determine the value of N_{pq} we can make use of an extension of the methods discussed in the previous section.

Consider that part of the beam Ψ_p which may be described by a mode-set in the x-direction

$$\Psi_p(x,z) = \sum_{m=0}^{\infty} A_{mp}\,\Psi_{mp}\exp(-j\phi_m(z)) \quad (2.63)$$

where $$\phi_m(z) = (m+\tfrac{1}{2})\arctan(\lambda z/\pi w_o^2) \quad (2.64)$$

It should be noted that the above expressions differ from those given in section 2.3 which do not contain an explicit z-dependence. This is because we are here concerned with combining two beams which possess a pre-determined phase difference that

is dependent upon the distances Z_1 and Z_2, whereas, in section 2.3, the relative phases of the coupled beams was described solely by the phases of the coupling coefficients. It is this z-dependent phase difference that generates the interferometric modulation of the output beam power hence permitting the interferometer's use as a diplexer.

As 2.63 and 2.64 are one-dimensional the expression for ϕ_m differs from that for Φ_m given earlier. It can be seen, however, that Φ_m represents the product of two terms $\phi_m(x)$ and $\phi_m(y)$.

$\psi_p(x,y,z)$ may now be regarded as

$$\psi_p(x,y,z) = \psi_p(x,z)\,\psi_p(y,z)\exp(-jkz) \qquad (2.65)$$

where $\psi_p(y,z)$ is a mode set similar to that given in 2.63

Hence

$$\Psi_{pq} = \tfrac{1}{2}(\psi_p(x,Z_1)\,\psi_p(y,Z_1)\exp(-jkZ_1) + T_{pq}\psi_p(x,Z_2)\,\psi_p(y,Z_2)\exp(-jkZ_2)) \qquad (2.66)$$

Now the power, P_{pq}, associated with Ψ_{pq} is given by

$$P_{pq} = \langle \Psi^*_{pq} | \Psi_{pq} \rangle \qquad (2.67)$$

which, from the above, leads to

$$\begin{aligned} P_{pq} = \tfrac{1}{4}(& \langle \psi^*_p(x,Z_1) | \psi_p(x,Z_1)\rangle \langle \psi^*_p(y,Z_1) | \psi_p(y,Z_1)\rangle \\ & + \langle \psi^*_p(x,Z_2) | \psi_p(x,Z_2)\rangle \langle \psi^*_p(y,Z_2) | \psi_p(y,Z_2)\rangle \\ & + T^*_{pq}\langle \psi^*_p(x,Z_2) | \psi_p(x,Z_1)\rangle \langle \psi^*_p(y,Z_2) | \psi_p(y,Z_1)\rangle \exp(-jk(Z_1-Z_2)) \\ & + T_{pq}\langle \psi^*_p(x,Z_1) | \psi_p(x,Z_2)\rangle \langle \psi^*_p(y,Z_1) | \psi_p(y,Z_2)\rangle \exp(+jk(Z_1-Z_2))) \end{aligned} \qquad \ldots (2.68)$$

Now we may define the z-invariant parameters X and Y as

$$X = \langle \psi_p^*(x,z) \mid \psi_p(x,z) \rangle \tag{2.69}$$

$$Y = \langle \psi_p^*(y,z) \mid \psi_p(y,z) \rangle \tag{2.70}$$

where X and Y must be real, non-negative numbers.

It may also be shown that

$$\langle \psi_p^*(x,Z_1) \mid \psi_p(x,Z_2) \rangle = \langle \psi_p^*(x,Z_2) \mid \psi_p(x,Z_1) \rangle^* \tag{2.71}$$

$$\langle \psi_p^*(y,Z_1) \mid \psi_p(y,Z_2) \rangle = \langle \psi_p^*(y,Z_2) \mid \psi_p(y,Z_1) \rangle^* \tag{2.72}$$

and so we may write

$$P_{pq} = \tfrac{1}{2}\Big(X.Y + \text{Real}\Big[T_{pq} \langle \psi_p^*(x,Z_1) \mid \psi_p(x,Z_2) \rangle \cdot \langle \psi_p^*(y,Z_1) \mid \psi_p(y,Z_2) \rangle \cdot \exp(jk(Z_1-Z_2))\Big]\Big) \tag{2.73}$$

Now, as $\langle \psi_p^*(x,y,z) \mid \psi_p(x,y,z) \rangle = X.Y$, we may write

$$N_{pq} = \tfrac{1}{2}\Big(1 + \frac{T_{pq}}{(X.Y)} \cdot \text{Real}\Big[\langle \psi_p^*(x,Z_1) \mid \psi_p(x,Z_2) \rangle \cdot \langle \psi_p^*(y,Z_1) \mid \psi_p(y,Z_2) \rangle \cdot \exp(jk(Z_1-Z_2))\Big]\Big) \tag{2.74}$$

Consider the function

$$G_x = \langle \psi_p^*(x,Z_1) \mid \psi_p(x,Z_2) \rangle \tag{2.75}$$

By substituting into this expression a mode set of the form shown in 2.63 we obtain

$$G_x = \sum_{m=0}^{\infty}\sum_{n=0}^{\infty} A_m^* A_n \langle \psi_{mp}^*(x,Z_1) \mid \psi_{mp}(x,Z_2) \rangle \exp(-j(\phi_m(Z_1) - \phi_n(Z_2))) \quad \ldots\ldots (2.76)$$

Now,

$$\langle \psi_{mp}^*(x,Z_1) \mid \psi_{mp}(x,Z_2) \rangle = \left(\frac{2}{\pi . w_1 . w_2 . 2^m . 2^n . m! . n!}\right)^{\frac{1}{2}} \cdot \int_{-\infty}^{\infty} H_m(x\sqrt{a}) H_n(x\sqrt{b}) \exp(-Sx^2)\, dx \tag{2.77}$$

where $$a = (1/w_1)^2 \qquad (2.78)$$

$$b = (1/w_2)^2 \qquad (2.79)$$

and $$S = \left((1/w_1)^2 + (1/w_2)^2 + (jk/2)((1/R_2) - (1/R_1)) \right) \qquad \ldots. (2.80)$$

It is immediately clear that the above integral is similar to that in expression 2.48 and hence the solution is also of as similar form. The answer may therefore be expressed as a modified form of the coupling coefficients introduced in the previous section. By substitution of the above values of a, b, and S obtained above into 2.52, 2.53, and 2.54 it can be shown that these modified coefficients are equivalent to those listed earlier if $w(Z_1)$, $w(Z_2)$, $R(Z_1)$, and $R(Z_2)$ are identified with w_p, w_q, R_p, and R_q. For convenience we may continue to use the symbols C_{mpnq} to represent these coefficients of modified form.

We may now write

$$G_x = \sum_{m=0}^{\infty} \sum_{n=0}^{\infty} A^*_{mp} A_{nq} C_{mpnq} \exp(j(\phi_n(Z_2) - \phi_m(Z_1))) \qquad (2.81)$$

For a known beam mode set, $A_{mp}\psi_{mp}(x)$, and $B_{mp}\psi_{mp}(y)$, G_x and the corresponding function in the y-direction, G_y, may now be determined as functions of Z_1 and Z_2. These in turn lead to a value for N_{pq} as

$$N_{pq} = \tfrac{1}{2}\left(1 + T_{pq} \cdot \text{Real}\left[G_x \cdot G_y \cdot \exp(jk(Z_1 - Z_2)) \right] / (X.Y) \right) \qquad \ldots.(2.82)$$

When considering a plane parallel beam propagating in the z-direction the rate of phase change when moving in that direction, θ', is of the form

$$\theta' = k$$

This leads to the expected result that the interferometric modulation depends upon the path difference, D, but not upon the mean path length. For a Gaussian mode, however, the rate of change of phase in the z-direction is of the form

$$\Theta' = k - \frac{\partial}{\partial Z}\left(\phi_m(Z)\right) + \frac{k(x^2+y^2)}{2} \cdot \frac{\partial}{\partial Z}\left(R(Z)\right)$$

Hence the rate of phase change may in general be expected to be a function of both mode number, m, and location. This being so, those values of Z_1 and Z_2 which maximise(or minimise)the contribution of the m'th mode to N_{pq} may not maximise(or minimise) that due to the n'th mode(where $m \neq n$). It can therefore be anticipated that, for a multi-mode beam, the modulation of N_{pq} as a function of Z_1 and Z_2 is less, in general, than in the case of a single-mode beam. For this reason it is desirable to ensure that the radiation passing through the interferometer should approach being a single-mode beam.

Fortunately it is possible in practice to generate beam patterns which consist almost exclusively of a fundamental mode. For this reason we may now direct our attention to the consideration of a pure fundamental beam. Before doing so, however, it is of interest to examine the magnitude of the effect upon N_{pq} of contamination of the fundamental beam with a small amount of a higher order mode.

Consider the example of a beam composed of a linear sum of the fundamental and the m'th mode in each dimension, i.e.

$$(x,z) = A\,\psi_o(x,z) + B\,\psi_m(x,z) \qquad (2.83)$$

$$(y,z) = C\,\psi_o(y,z) + D\,\psi_m(y,z) \qquad (2.84)$$

From this it follows that the power contained by such a beam, P, is given by

$$P = (A^{*}A + B^{*}B) . (C^{*}C + D^{*}D) \qquad (2.85)$$

In practice it is found that the beams of interest for use with the interferometer are essentially symmetric, hence we may set A = C, B = D, and

$$P = (A^{*}A + B^{*}B)^{2} \qquad (2.86)$$

We may now write the interferometer's coupling efficiency as

$$N_{pq} = \tfrac{1}{2}\left(1 + \frac{T_{pq}}{(A^{*}A + B^{*}B)^{2}} \cdot \mathrm{Real}\left[G_x G_y \exp(jk(Z_1 - Z_2)) \right] \right) \qquad \ldots\ (2.87)$$

Where G_x and G_y are as defined earlier. In terms of the modified coupling coefficients, C_{mn}, it may be shown that

$$\begin{aligned} G_x = \quad & A^{*}A\, C_{oo} \exp(-j(\not\phi_o(Z_1) - \not\phi_o(Z_2))) \\ + \quad & B^{*}A\, C_{mo} \exp(-j(\not\phi_m(Z_1) - \not\phi_o(Z_2))) \\ + \quad & A^{*}B\, C_{om} \exp(-j(\not\phi_o(Z_1) - \not\phi_m(Z_2))) \\ + \quad & B^{*}B\, C_{mm} \exp(-j(\not\phi_m(Z_1) - \not\phi_m(Z_2))) \end{aligned} \qquad (2.88)$$

and $G_x = G_y$ in the case of a symmetric beam.

N_{pq} may hence be calculated as a function of the various parameters by the use of expressions 2.87 and 2.88.

A computer program was written to enable the calculation of N_{pq} as a function of w_o, Z_1, Z_2, etc, and some of the results obtained are shown in Figs 8 and 9. Here a standard NAG library routine(E04AAF)was employed to find the local minimum of N_{pq} (p=q)as a function of Z_2 over a range of values of w_o and A. Z_1-Z_2 was chosen to approximate the path difference of a diplexer employed with an intermediate frequency of 4 GHz. Z_1, in these examples, has been chosen so as to place the recombination planes at a reasonable distance from the beam-waist.

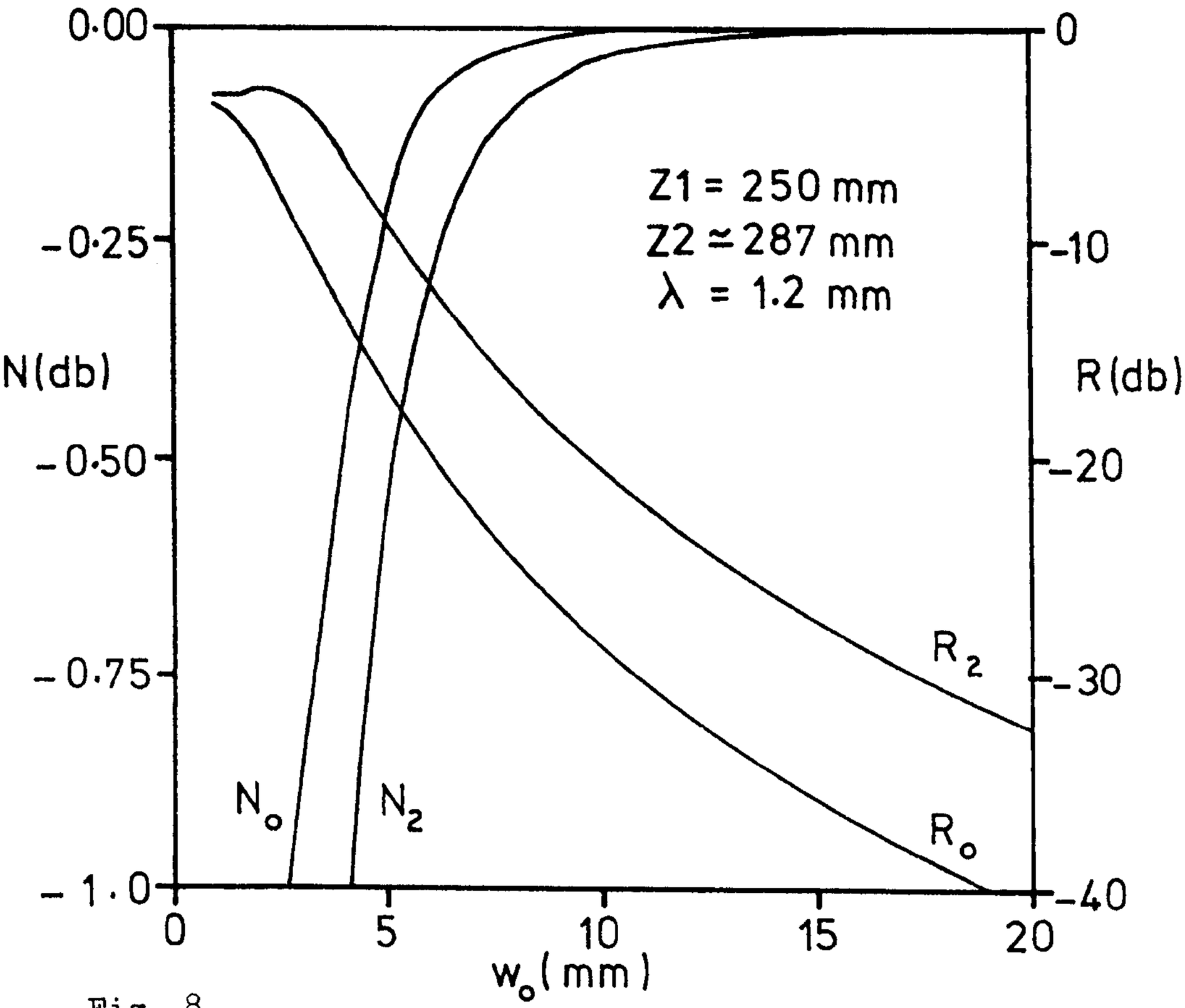

Fig. 8.
Single mode coupling efficiency.

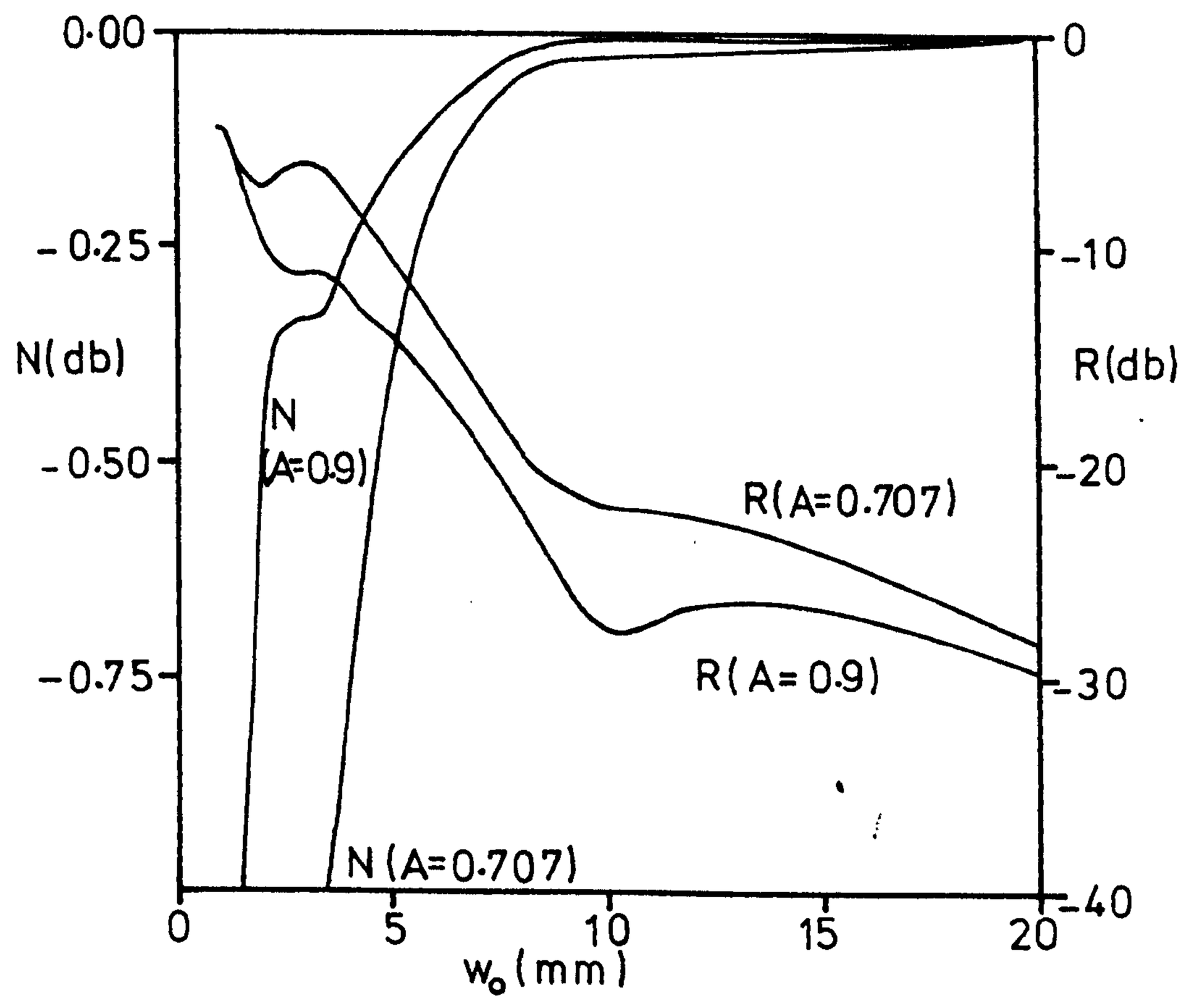

Fig. 9.
Contaminated mode coupling efficiency.

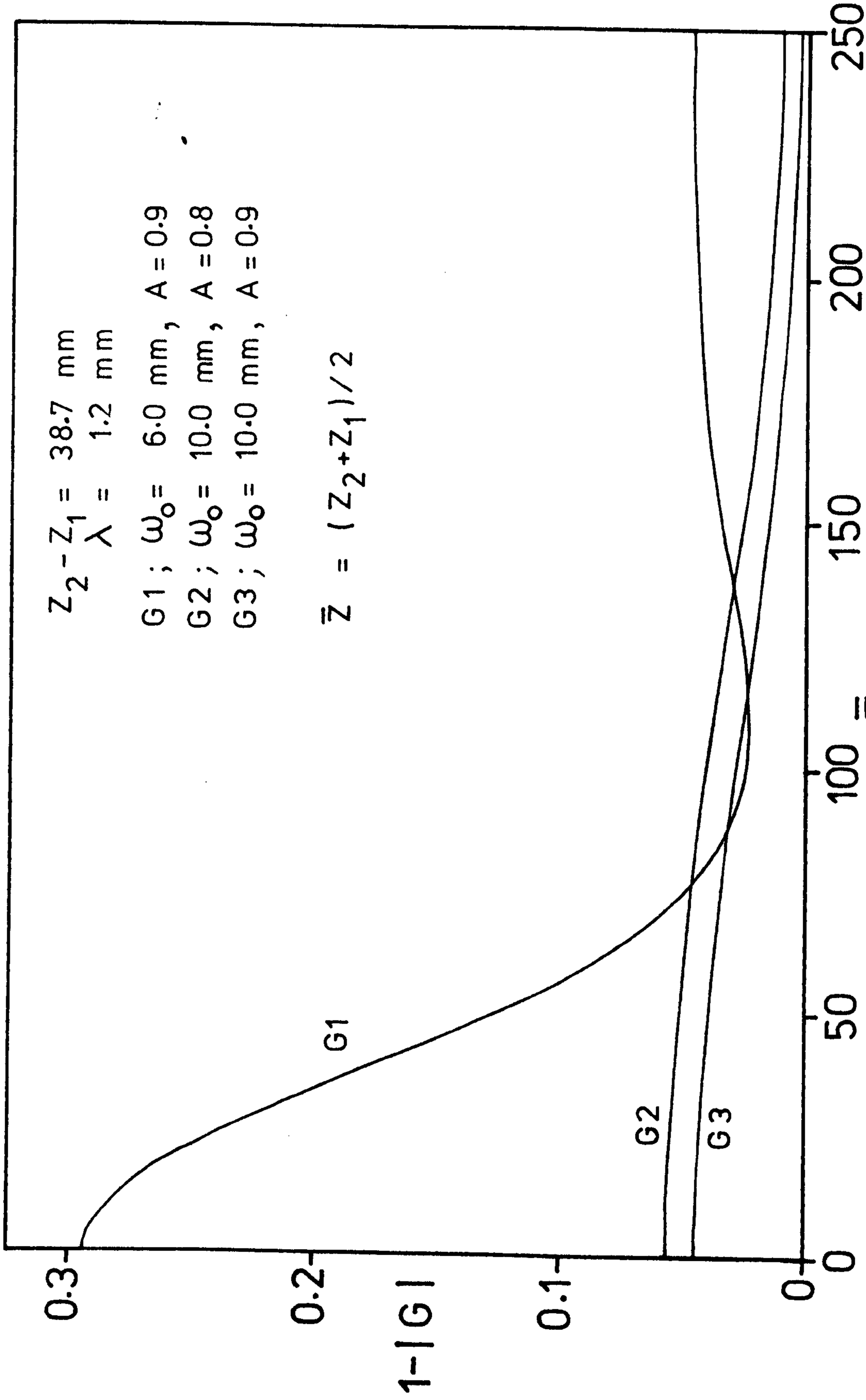
$Z_2 - Z_1$ = 38.7 mm
λ = 1.2 mm
G1 ; ω_o = 6.0 mm, A = 0.9
G2 ; ω_o = 10.0 mm, A = 0.8
G3 ; ω_o = 10.0 mm, A = 0.9
$\bar{Z} = (Z_2 + Z_1)/2$
G1
G2
G3
250
200
150
100
50
0
$\bar{Z}$ mm
0.3
0.2
0.1
0
$1-|G|$

Fig. 10.

The minimum value of N_{pq} may be regarded as the maximum value of the rejection figure, R_{pq}, as it represents the greatest amount by which unwanted power may be rejected from the path p=q.

By both the conservation of energy and the symmetric nature of the interferometer, the maximum coupling efficiency, $N_{pq}(max)$, for the path $p \neq q$ is related to the maximised rejection figure by the expression $N = 1 - R$.

In Fig 8 the maximum coupling efficiency and rejection figure are plotted as functions of w_o. N_o, R_o, refer to a beam composed of a pure fundamental mode, and N_2, R_2, refer to a beam composed solely of the m=2 mode. Fig 9 shows similar curves for a mixed-mode beam of the form

$$\chi = A\chi_o + (1-A^2)^{\frac{1}{2}}\chi_2 \qquad (2.89)$$

where $0 \leq A \leq +1$ and A is real.

This corresponds to a dual-mode beam with a unity total power whose components are in-phase at the common beam-waist.

It will be seen from these graphs that, for $w_o \geq 10\lambda$, the main effect of beam contamination is upon the rejection figure. In this region the effect upon the coupling efficiency is very small, and in practice would prove most difficult to measure.

For a beam of unity power we may write

$$N_{pq} = \tfrac{1}{2}\left(1 + T_{pq}.\mathrm{Real}\left[G.\exp\left(jk(Z_1-Z_2)\right)\right]\right) \qquad (2.90)$$

where $G = G_xG_y$. Hence G is a function of Z_1 and Z_2.

Some examples of the variation of G as a function of $(Z_1+Z_2)/2$ (where Z_2-Z_1 = constant)are shown in Fig 10. Here $1-|G|$ is plotted against $\overline{Z}$ when Z_2-Z_1 = 38.7mm. These graphs serve to illustrate that G is, in general, a slowly-varying function

of $\overline{Z}$ and that the magnitude of this variation reduces as kw_o or A is increased. In particular, as $kw_o \rightarrow \infty$, $G \rightarrow 1$, irrespective of the beam mode composition. This may be seen from a consideration of the expressions for G_x and G_y given earlier.

As $kw_o \rightarrow \infty$; we have $\phi_m(Z) \rightarrow 0$, $C_{mn}(m=n) \rightarrow 1$, and $C_{mn}(m \neq n) \rightarrow 0$. Hence as kw_o increases, $(G_x G_y)/(X.Y) \rightarrow 1$, and the coupling efficiency rapidly approaches the limit

$$N_{pq}(kw_o \rightarrow \infty) = \tfrac{1}{2}(1 + T_{pq}.\mathrm{Real}(\exp(jk(Z_1-Z_2)))) \quad (2.91)$$

which is equivalent to the coupling efficiency predicted by the assumption of plane parallel beams of sinusoidal form.

From Figures 8, 9, 10, and from the above arguments it will be seen that we may for most purposes treat the beam as a pure fundamental Gaussian provided $w_o > 10\lambda$ and $A_o > 0.9$.

Let us now, therefore, consider a symmetric fundamental-mode beam of unity power. In this case

$$G = G_x G_y = (C_{oo}(-j(\phi_o(Z_1) - \phi_o(Z_2))))^2 \quad (2.92)$$

$$= \left(\frac{2}{w_1 w_2}\right) \cdot ((1/w_1)^2 + (1/w_2)^2 - (jk/2)((1/R_1)-(1/R_2))^{-1}$$

$$\cdot \exp(-j(\phi_o(Z_1) - \phi_o(Z_2))) \quad (2.93)$$

By making use of the substitutions

$$\exp(-j.\arctan(a/c)) = (a^2+c^2)^{-\frac{1}{2}} \cdot (c-ja)$$

$$\exp(+j.\arctan(b/c)) = (b^2+c^2)^{-\frac{1}{2}} \cdot (c+jb)$$

where $a = 2Z_1$, $b = 2Z_2$, and $c = kw_o^2$, we obtain

$$G = \frac{2(c - ja)(c + jb)}{c^2 + a^2 + b^2 + c^2 - (j/c)(a(b^2 + c^2) - b(a^2 + c^2))} \quad \ldots.(2.94)$$

This may be rearranged into the form

$$G = 2((1 - j(a/c)) + (1 + j(b/c)))^{-1} \qquad (2.95)$$

$$\text{i.e.} \quad G = (1 + (j/kw_o^2)(Z_2-Z_1))^{-1} \qquad (2.96)$$

From the form of this expression it is clear that, in the case of a symmetric Gaussian beam, G does not depend upon the mean path length between the beam-waist and the recombination planes, $\bar{Z}$, but only upon the path difference (Z_2-Z_1).

This is a useful result for two reasons: a) The beam-waist location may be chosen on the basis of practical convenience without the concern that an unsuitable value will degrade the diplexer's performance unnecessarily; b) In practice the recombination planes may not be perpendicular to the z-direction. Typically, the polariser which performs this function is at 45° to the beam axies. If G were to exhibit a significant z-dependency this might be expected to affect the actual value of N_{pq} obtained in a z-dependent manner.

From the above arguments, however, where the beam may be regarded as an essentially pure fundamental Gaussian mode the interferometer's performance can be accurately predicted by an almost trivially simple calculation.

When employing the interferometer as a diplexer we require that it should, ideally, optimise both the signal and local oscillator coupling efficiencies simultaneously. In practice this may not occur as, even when $Z_2-Z_1 \simeq \lambda_{if}/2$, the local oscillator and signal coupling efficiency maxima may not be perfectly coincident.

To evaluate this effect let us consider two similar Gaussian beams of frequency k_1, k_2, which enter via the p = 1 and p = 2 input ports respectively. The relevant coupling efficiencies

at the output port, q, are therefore given by expressions of the form

$$N_{pq} = \tfrac{1}{2}(1 + T_{pq}.\text{Real}\left[G_p.\ \exp(jk_pD)\right]) \qquad (2.97)$$

Where $D = Z_1 - Z_2$, and G_p is the appropriate coupling factor.

Now in order to optimise N_{pq} we may, by a suitable choice of w_o arrange that $G_p \to 1$. This effectively arranges that we approach the case approximated by plane parallel beams where

$$N_{pq} = \tfrac{1}{2}(1 + T_{pq}.\text{Real}\left[\exp(jk_pD)\right]) \qquad (2.98)$$

Let $k_1 = k$; $k_2 = k + dk$; and $dk \ll k$.

We may now write

$$N_{1q} = \tfrac{1}{2}(1 + T_{1q}.\ \text{Cos}(kD)) \qquad (2.99)$$

$$N_{2q} = \tfrac{1}{2}(1 + T_{2q}.\ \text{Cos}((k+dk)D)) \qquad (2.100)$$

In order to maximise N_{1q} we require that $T_{1q}.\ \text{Cos}(kD) = +1$, and, from previous considerations, we may expect that the optimum diplexing action will occur when

$$D = \frac{\lambda_{IF}}{2} + x = \frac{\pi}{dk} + x \qquad (2.101)$$

where $|x| \ll \pi/k$.

i.e. the optimum diplexing action will occur at the N_{pq}-maximum closest to $D = \pi/dk$.

Now $T_{1q}.\ \text{Cos}(kD) = +1$ implies $\text{Sin}(kD) = 0$, hence

$$\text{Cos}((k+dk)D) = \text{Cos}(kD).\text{Cos}(dk.D)$$

$$= \frac{\text{Cos}(dk.D)}{T_{1q}} \qquad (2.102)$$

and

$$N_{2q} = \tfrac{1}{2}(1 + (T_{2q}/T_{1q}).\text{Cos}(dk.D)) \qquad (2.103)$$

From the above definition of D and from knowing that $T_{1q} = -T_{2q}$

$$N_{2q} \qquad \tfrac{1}{2}(1 - \mathrm{Cos}(\pi\, dk/k)) \qquad (2.104)$$

This expression enables us to establish the most serious degredation of the coupling efficiency and rejection figure that will be produced by the non-coincidence of the maxima in N_{1q} and N_{2q}. As an example, if f_1 = 250 GHz, f_2 = 254 GHz, we obtain $N_{2q} \geqslant 0.99936(-0.0027db)$, which implies that the rejection figure will be better than -32db.

When we are concerned with optimising the coupling efficiency for a single monochromatic input beam, γ_p, N_{pq} may be brought arbitrarily close to unity by increasing w_o. In general, however, there is little benifit to be gained beyond the value which causes N_{pq} to exceed 1-dN, where dN is the probable degredation of N_{pq} produced by the combined effects of a finite signal bandwidth(as discussed in section 2.2)and the non-coincidence of the signal and local oscillator coupling maxima.

Where the diplexer is designed such that $N_{pq} \geqslant 1-dN$ it will usually be discovered that, in practice, the receiver's performance is limited by the physical imperfections of the various optical elements employed. The nature of these imperfections and their effect upon the receiver's performance will be discussed and measured in the following sections.

2.5 Local Oscillator-Mixer coupling via the Diplexer.

The forms of the local oscillator source and the mixer employed with the diplexer were chosen at the commencement of receiver design. This was because it was decided to exploit what was already known about existing techniques which could be expected to perform satisfactorily over the frequency range of interest.

The local oscillator selected was a crossguide multiplier supplied by N.J.Cronin of the Queen Mary College Physics Dept (Cronin, et al, Infra. Phys. 18 731 (1978)). The mixer was provided by D.Vizard of the Appleton Laboratory. Each of these designs are based upon conventional waveguide techniques and suitable antennas were therefore required to enable their use with a Quasi-Optical system.

The situation with regard to the coupling of power between the local oscillator and the mixer may be illustrated by reference to Fig 11.

Here local oscillator power is radiated from a feed-horn onto a lens, L1, which directs the power into the diplexer via port p. The mixer is coupled to exit port q by a similar feed-horn/lens combination.

The effectiveness with which power is conveyed from the local oscillator to the mixer is restricted by three forms of power loss:

a) Loss due to physical imperfections of the various optical elements - e.g. absorbtion by the lens dielectric.

b) Losses due to N_{pq} being less than unity.

c) Losses due to mismatch between the beam/antenna patterns of the local oscillator power emergent from q($\mathcal{F}_1$)and the mixer($\mathcal{F}_d$).

The loss of power produced by a) will be determined, principally by measurement, later in this thesis, and that

$$\mathfrak{x}_\lambda = \tfrac{1}{2}(\psi_\alpha(Z_1) + T_{pq}\,\psi_\alpha(Z_2))$$

$$\mathfrak{x}_d$$

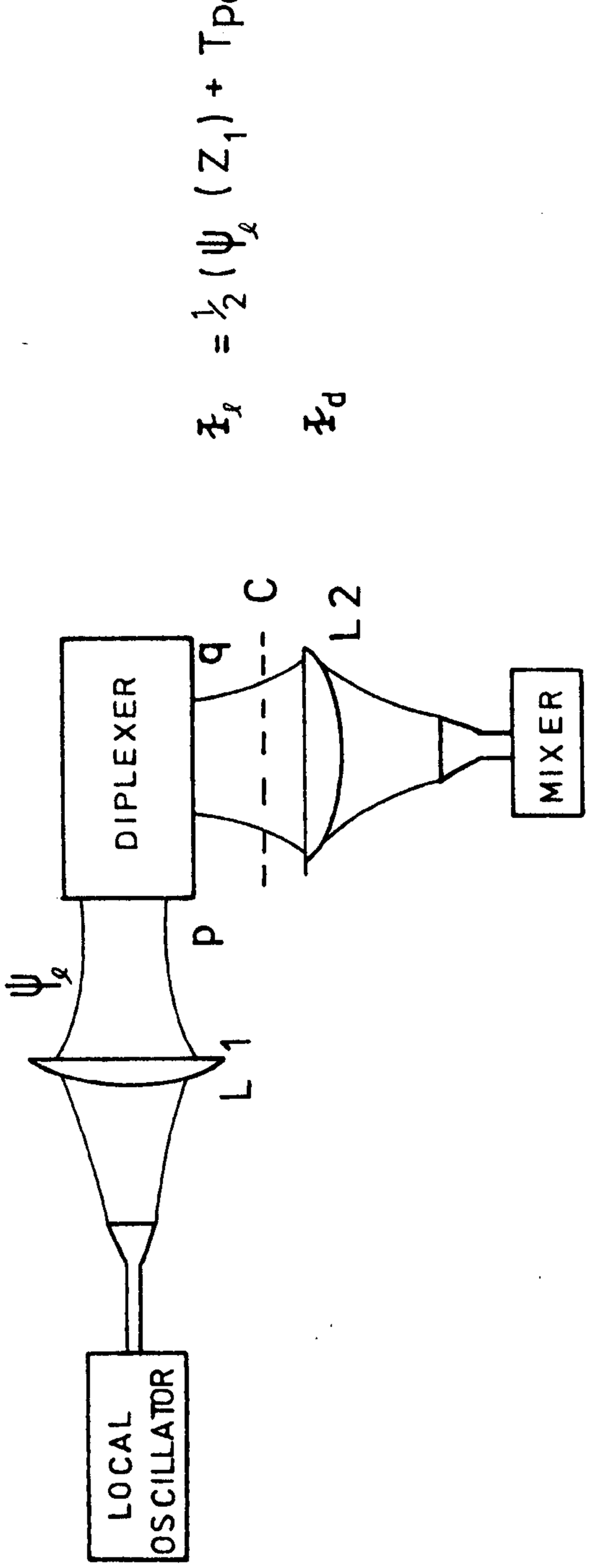

Fig. 11.
L.O. coupling via the Diplexer.

due to b) has already been considered in section 2.4. In this section the effect of c) upon receiver performance will be examined in terms of a coupling integral over a plane such as C in Fig 11.

In the case of the receiver constructed for use with the United Kingdom Infra-Red Telescope it was decided that the waveguide devices would be coupled into free-space readiation by conventional flared feed horns used in conjunction with appropriate lenses. This decision was made for the reason already quoted in connection with the choice of the form of the local oscillator source and mixer.

Before considering the coupling integral which may be employed to calculate the beam-mismatch loss at C it is therefore necessary in this case to examine the properties of feed horns and lenses in terms of Gaussian mode sets. The methods of analysis discussed later in this section may, however, be generally applied to any form of antenna used with a quasi-optical system.

One of the earliest theoretical treatments of flared feed radiators is that by Barrow and Lewis(Proc. IRE 27 41 (1939)). This predicts the radiation pattern of a horn flared in a single dimension parallel to either the electric- or magnetic-field direction of a linearly polarised wave produced by a generator near the horn apex. In a subsequent paper by Barrow and Chu(Proc. IRE 27 51 (1939))the same method of analysis is applied to the more general case of a horn flared in two dimensions into the form of a rectangular pyramid.

These feed horns, and those of conical forms treated by Schelkunoff(Electromagnetic Waves. Van Nostrand, New York, 1943), King(Proc. IRE 38 249 (1950)), and others, assume that the

boundary walls are smooth, ideal conductors. The radiation pattern is then predicted from the application of Maxwell's equations under the requirement that the electric field component along the conducting surfaces and the magnetic field component into the surfaces should be zero.

Subsequently, Clarricoats and Saha published two papers (Proc. IEE 118 1167, and 1177 (1971))which provide a detailed analysis of conical feeds with corrugated walls. This type of feed possesses a number of advantages over the plane-walled form. Of particular interest here is the ability to produce highly symmetric antenna patterns with low sidelobe levels. In addition, where the waveguide coupled to the horn apex supports a single, plane polarised mode, the antenna pattern is also confined almost exclusively to a single plane of polarisation. These properties are preserved over a substantial range of frequencies(typically 1.5:1).

Figure 12 represents a corrugated conical feed of length, L, and flare angle, θ. The behaviour of such a feed may be conveniently characterized by two dimensionless parameters, ka, and Δ, where

$$\Delta = (ka/2\pi).\tan(\theta/2) \qquad (2.105)$$

Clarricoats and Saha observed(ibid)that under some conditions the feed's antenna pattern is almost Gaussian in form. These conditions correspond to a horn of small flare angle and overall length excited by balanced hybrid modes(see Clarricoats and Saha). Under these conditions the phase shift across the horn's aperture is small and the electric field in the aperture plane may be represented by the scalar

$$J_o^T(\alpha r)\exp(-(jk/2L)r^2) \qquad (2.106)$$

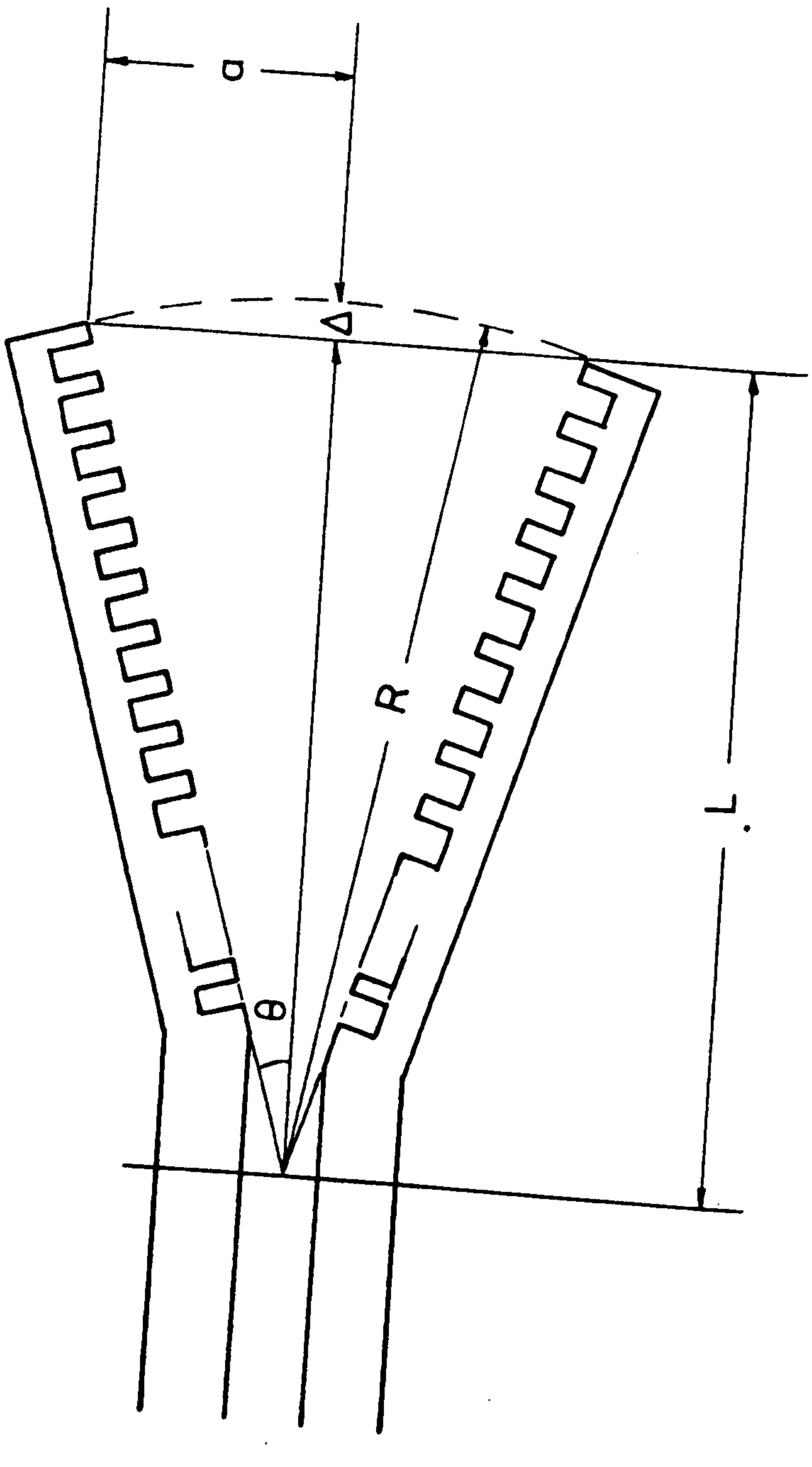

Fig. 12.
Corrugated feed horn.

where

$$J_o^T(\alpha r) = \begin{cases} J_o(\alpha r) & ; r \leq a \\ 0 & ; r > a \end{cases} \qquad (2.107)$$

and $a = 2.4048$(This positions the first zero of J_o at the aperture rim).

Aubry and Bitter(Elect. Lett. 11 154 (1975))observed that the antenna pattern due to this field distribution could be expressed quite concisely in terms of a set of Laguerre-Gaussian functions.

If we write

$$J_o^T(\alpha r) = \sum_{n=0}^{\infty} A_n L_n(2(r/w)^2).\exp(-(r/w)^2) \qquad (2.108)$$

where L_n is the Laguerre polynomial of degree n, it has been shown(Aubry and Bitter, ibid)by the application of numerical methods that, when $w/a = 0.64$

$$\frac{A_o^2}{\sum_{m=0}^{M} A_m^2} = 0.98 \qquad (2.109)$$

Since each Laguerre-Gaussian function represents a solution of the paraxial wave equation, 2.24, the series is a mode set which may be employed to describe the beam pattern produced by the antenna.

For a circularly symmetric beam each Laguerre-Gaussian term may be represented as the product of two similar Hermite-Gaussian modes. i.e. the beam may be represented as

$$\psi(r) = \left[\sum_{m=0}^{\infty} A_m \psi_m(x)\right].\left[\sum_{m=0}^{\infty} A_m \psi_m(y)\right] \qquad (2.110)$$

where $r^2 = x^2 + y^2$.

In terms of this new set of coefficients, A_m, we may write

$$\frac{|A_o|^4}{\left(\sum_{m=0}^{\infty} |A_m|^2\right)^2} = 0.98 \qquad (2.111)$$

Hence for a normalised beam, $A_o = (0.98)^{\frac{1}{4}} = 0.995$, which is sufficiently close to unity that the radiated beam pattern may be regarded for most purposes as a pure fundamental Gaussian.

As the horn length and flare angle increase the far-field pattern departs from a simple Gaussian shape. However, provided Δ is significantly less than unity the pattern retains a predominantly Gaussian profile. Figure 13 illustrates the antenna patterns at 220, 250, and 280 GHz of a feed horn for which $\Delta = 0.46$ at 250 GHz. These patterns were calculated by the use of a computer program due to Loefer, et al(Microwaves 15(5) 58 (1976)).

Where the pattern is essentially Gaussian the angle at which the normalised power, P_n, falls to 1/e of the axial value may be identified with θ_ξ where

$$\theta_\xi = \frac{\lambda}{2\pi\xi_o} = \frac{\lambda}{\sqrt{2}\pi w_o} \qquad (2.112)$$

if ξ_o and w_o are the power and amplitude beam waist sizes respectively.

At larger values of Δ the assumption of a simple Gaussian beam ceases to be appropriate and the antenna pattern must, in general, be represented as a mode-set. This may be done by a numerical function-fitting technique using either the aperture distribution or the far-field pattern.

In order to determine the amount of power coupled between two quasi-optical systems it is necessary to know both the compositions of the relevant mode sets and the locations of their beam waists.

Now as defined by Thomas(ibid) Δ is the axial distance in wavelengths between the spherical phasefront which touches the aperture rim and the aperture plane(see Fig 12). Hence

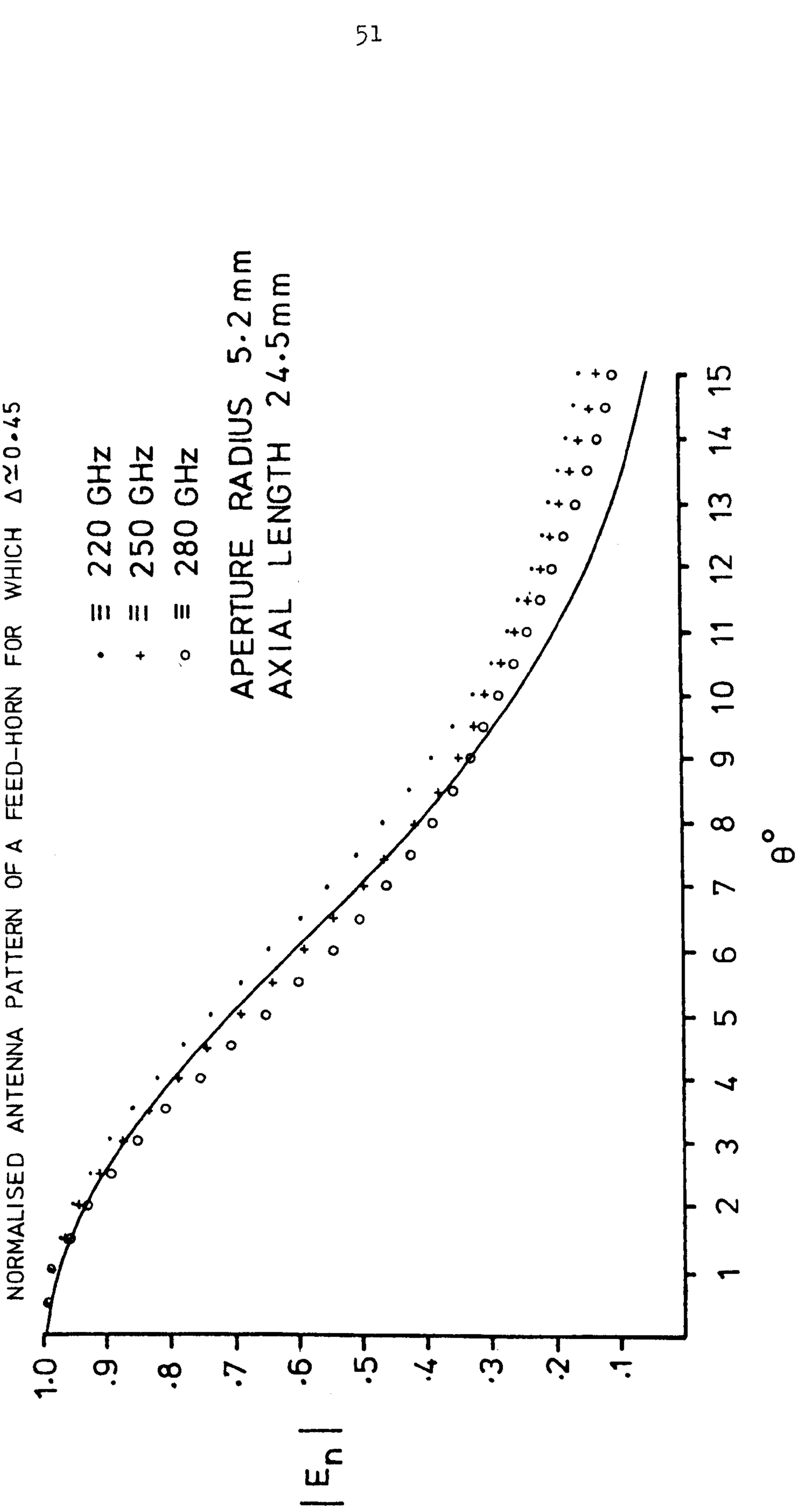
NORMALISED ANTENNA PATTERN OF A FEED-HORN FOR WHICH Δ≃0.45
• ≡ 220 GHz
+ ≡ 250 GHz
○ ≡ 280 GHz
APERTURE RADIUS 5.2mm
AXIAL LENGTH 24.5mm
1.0
.9
.8
.7
.6
.5
.4
.3
.2
.1
1 2 3 4 5 6 7 8 9 10 11 12 13 14 15
θ°
E/E_m

Fig. 13.

in general when Δ is very small, say ≤ 0.1, the phasefront at the aperture is effectively plane and the beam waist may be regarded as being located at the aperture. As Δ increases the beam waist moves into the horn, towards the apex, by an amount that may be calculated from knowing the beam waist size and the radius of curvature of the phasefront at the aperture.

Thomas has made use of the conventional theoretical method based upon the work of Clarricoats and others to obtain a graph which indicates the position of the far-field phase centre of the radiated pattern as a function of Δ.

For a single-mode Gaussian beam the far field phase centre is located at the axial intercept of the beam waist. This is because any single mode has a uniform phase over each spherical surface whose radius, R, is given by expression 2.28, and $(z-R) \rightarrow 0$ as $z \rightarrow \infty$. This need not, however, be true for a multi-mode beam as the phase across a spherical surface of radius, R, will in such a case depend upon the composition of the beam mode set and may be expected to vary as a function of distance from the beam waist.

The standard theoretical methods have been employed by Ohtera and Ujiie(IEEE AP-23 858 (1975))to obtain nomographs of the effective phase centre location as a function of various parameters including the distance from the horn aperture to the point of observation(which is assumed to be on-axis).
In contrast with this approach the Gaussian-beam method permits the location of the beam waist to be obtained as the result of a fairly simple calculation given the relevant values of R, Δ, and w_o. The radius of curvature of the wavefront may then be obtained for any position along the beam by the use

of 2.28.

The beam waist location may be obtained by re-arranging 2.28 into the form

$$z = \tfrac{1}{2}\left(R \pm \left(R^2 - 4(\pi w_o^2/\lambda)^2\right)^{\frac{1}{2}}\right) \qquad (2.113)$$

It should be noted that there are two possible solutions for z, however, since we are here interested only in the near-field solution for which $z \to 0$ as $R \to \infty$ the above becomes

$$z = \tfrac{1}{2}\left(R - \left(R^2 - (\lambda/\pi\theta_s^2)^2\right)^{\frac{1}{2}}\right) \qquad (2.114)$$

where θ_s is the angle defined by 2.112.

As the wavefront of radius R nominally intersects the optical axis a distance $\Delta\lambda$ in front of the aperture plane the beam waist may be taken to be a distance, t, behind the aperture plane, where

$$t = \tfrac{1}{2}\left(R - \left(R^2 - (\lambda/\pi\theta_s^2)^2\right)^{\frac{1}{2}}\right) - \Delta\lambda \qquad (2.115)$$

The horn's far field pattern may be derived from the program due to Loefer et al or read off the figure given by Thomas(ibid) and, provided the resultant pattern is essentially Gaussian in form, θ_s may be regarded as the angle at which the radiated power falls to 1/e of its axial value. The beam waist size and location may then be calculated by the use of 2.27, 2.28, and the expressions given above.

Having defined a Gaussian mode set which satisfactorily describes the radiation produced by a given feed horn we may now examine the effect of a lens upon such a mode set.

In Gaussian optics the action of a lens is frequently described in terms of a transfer matrix which converts each ray, x_1, of an input ray-bundle into a new ray, x_2, according

to

$$\begin{pmatrix} x_2 \\ \frac{dx_2}{dz} \end{pmatrix} = \begin{pmatrix} 1 & 0 \\ -1/f & 1 \end{pmatrix} \begin{pmatrix} x_1 \\ \frac{dx_1}{dz} \end{pmatrix} \qquad (2.116)$$

where each x is complex and is proportional to the complex ray parameter, q, defined as

$$q = z + j(\pi w_o^2/\lambda) \qquad (2.117)$$

The modulus of x represents the distance from the beam axis to the ray and from 2.117 this may be seen to vary hyperbolically as a function of z.

When each beam is described in terms of a set of beam modes it is, however, generally more convenient to define an idealized lens in terms of its effect upon the phase distribution of an incident beam.

Consider an input mode of the form

$$\mathcal{X}_{mp}(x,y,z) = A_{mp}H_{mp}\exp(-r^2((1/w)^2 + j(k/2R))) \cdot\exp(-j(kz-\mathcal{F}_{mp})) \qquad (2.118)$$

where

$$r^2 = x^2 + y^2 \qquad (2.119)$$

$$H_{mp} = H_m(\sqrt{2}x/w).H_p(\sqrt{2}y/w) \qquad (2.120)$$

A_{mp} contains the amplitude and phase of the mode at the beam waist and the other variables are as defined earlier.

This beam mode is transformed by the action of an idealized lens into a new mode, $\mathcal{X}'_{mp}$, such that

$$\mathcal{X}'_{mp}(x,y,z) = \mathcal{X}_{mp}(x,y,z).\exp(j(kr^2/2f) \qquad (2.121)$$

Hence immediately after transformation by the lens

$$\psi_{mp}'(x,y,L) = A_{mp}H_{mp}\exp(-r^2((1/w)^2 + j(k/2R'))) \cdot\exp(-j(kL-\Phi_{mp})) \qquad (2.122)$$

where

$$(1/R') = (1/R) - (1/f) \qquad (2.123)$$

and L is the distance from the beam waist to the lens plane.

The distance from the lens plane to the transformed beam waist position, L', is such that

$$L' = R'(1 + (\lambda R'/\pi w^2)^2)^{-1} \qquad (2.124)$$

and the transformed beam waist size is given by

$$w_o' = w(1 + (\pi w^2/\lambda R')^2)^{-\frac{1}{2}} \qquad (2.125)$$

where w and R' are the beam size and the transformed radius of curvature at the lens.

In order to describe the propagation of the transformed beam it is necessary to define a modified beam mode expression

$$\psi_{mp}'(x,y,z') = A_{mp}'H_{mp}'\exp(-r^2((1/w')^2 + j(k/2R'))) \cdot\exp(-j(kz'-\Phi_{mp}')) \qquad (2.126)$$

for which it is required that, at the lens plane

$$\psi_{mp}(x,y,L).\exp(j(kr^2/2f) = \psi_{mp}'(x,y,L') \qquad (2.127)$$

if L and L' represent the distance from the lens plane to each beam waist, and each primed quantity is a function of, z', the distance to the transformed beam waist. Hence

$$A_{mp}\exp(-j(kL-\Phi_{mp})) = A_{mp}'\exp(-j(kL'-\Phi_{mp}')) \qquad (2.128)$$

i.e.

$$A_{mp}' = A_{mp}\exp(-j(k(L-L') - \Phi_{mp} + \Phi_{mp}')) \qquad (2.129)$$

From the above expressions it can be seen that the moduli of A_{mp} and A_{mp}' are the same although their phases will, in

general, differ by an amount which depends upon the mode numbers, m, p.

Where an input beam is represented as a set of modes of the form $\mathcal{X}_{mp}$ the transformed beam may be represented by a new set whose beam waist size and location are given by expressions 2.124 and 2.125. Each mode in this transformed set may then be written as

$$\mathcal{X}'_{mp} = A_{mp} D_{mp} H'_{mp} \exp(-r^2((1/w')^2 + j(k/2R'))) \cdot \exp(-j(kz' - \Phi'_{mp})) \qquad (2.130)$$

where each A_{mp} is the initial mode coefficient as in expression 2.118 and

$$D_{mp} = \exp(-j(k(L-L') - \Phi_{mp} + \Phi'_{mp})) \qquad (2.131)$$

In practice the absolute phase of each mode may usually be neglected and 2.131 may be replaced by

$$D_{mp} = \exp(j(\Phi_{mp} - \Phi'_{mp})) \qquad (2.132)$$

Now from the definition of Φ_{mp} given in an earlier section (expression 2.26).

$$D_{mp} = \exp(j(m+p+1)(\arctan(\lambda L/\pi w_o^2) - \arctan(\lambda L'/\pi w_o'^2))) \qquad \ldots.(2.133)$$

and it is a standard identity that

$$\exp(j(\arctan(a/b))) = (b + ja)/(a^2 + b^2)^{\frac{1}{2}} \qquad (2.134)$$

Hence

$$D_{mp} = \left(\frac{(\pi w_o^2 + j\lambda L) \cdot (\pi w_o'^2 - j\lambda L')}{((\pi w_o^2)^2 + (\lambda L)^2)^{\frac{1}{2}} \cdot ((\pi w_o'^2)^2 + (\lambda L')^2)^{\frac{1}{2}}} \right)^{(m+p+1)} \qquad (2.135)$$

Since the modulus of D_{mp} is one this is equivalent to

$$D_{mp} = \left[(1 + j(\lambda L/\pi w_o^2))(1 - j(\lambda L'/\pi w_o'^2)) \right]^{(m+p+1)} \quad \ldots.(2.136)$$

where the square brackets are defined such that

$$[C] = C / |C| \quad \ldots.(2.137)$$

Now, for a Gaussian mode

$$\pi w^2/\lambda R = \lambda z/\pi w_o^2 \quad \ldots.(2.138)$$

and at the lens plane

$$1/R' = 1/R - 1/f \quad \ldots.(2.139)$$

hence

$$D_{mp} = \left[(1+(1-R/f)(\lambda L/\pi w_o^2)^2) + j(\pi w^2/\lambda f) \right]^{(m+p+1)} \quad \ldots.(2.140)$$

If an angle, δ, is defined such that

$$D_{mp} = \exp(j(m+p+1)\delta) \quad \ldots.(2.141)$$

then

$$\delta = \arctan((\pi w^2/\lambda f)/(1+(1-R/f)(\lambda L/\pi w_o^2)^2)) \quad \ldots.(2.142)$$

which may be simplified into the form

$$\delta = \arctan((\pi w_o^2)/(\lambda(f-L))) \quad \ldots.(2.143)$$

hence

$$D_{mp} = \exp(j(m+p+1)\pi w_o^2/(\lambda(f-L))) \quad \ldots.(2.144)$$

Up to this point the details of the analysis discussed in this section have been explicitly directed towards understanding the behaviour of lens/feed-horn combinations. It should, however,

be noted that similar methods of analysis can be applied to define the mode sets generated by other systems.

Whatever the details of the system, once the appropriate mode set has been defined the various coupling parameters may be obtained by the application of the Gaussian techniques laid out in this thesis.

Consider once more the system as illustrated in Fig 11.

The amplitude coupled between the diplexer output port, q, and the mixer will depend upon the coupling integral $\langle \mathcal{F}_1^* | \mathcal{H}_d \rangle$ where

$$\mathcal{F}_1 = \tfrac{1}{2}(\mathcal{H}_1(Z_1) + T_{pq} \mathcal{H}_1(Z_2)) \qquad \ldots.(2.145)$$

and $\mathcal{H}_1$, $\mathcal{H}_d$ are mode sets similar in form to those discussed elsewhere in this thesis.

It is convenient to define a coupling coefficient of the form

$$C = \frac{\langle \mathcal{F}_1^* | \mathcal{H}_d \rangle}{\langle \mathcal{F}_1^* | \mathcal{F}_1 \rangle \langle \mathcal{H}_d^* | \mathcal{H}_d \rangle} \qquad \ldots.(2.146)$$

from which it follows that $P_d = CC^* P_1$ where, if P_1 is the power contained in the beam $\mathcal{F}_1$, then P_d represents the power coupled onto the mixer or detector whose beam pattern is defined by $\mathcal{H}_d$.

Now if the power contained in the input beam $\mathcal{H}_1$ is P, then $P_1 = N_{pq} P$, hence

$$P_d/P = CC^* N_{pq} \qquad \ldots.(2.147)$$

The right hand side of expression 2.147 represents the overall effectiveness with which power is transported from the local oscillator to the mixer. An overall coupling efficiency, K, may therefore be defined as

$$K = CC^{*}N_{pq} \qquad \ldots.(2.148)$$

In general, CC^{*} may be calculated by the use of the modified coupling coefficients employed earlier to obtain N_{pq}.

It may often be arranged that the mode sets $\mathcal{Y}_1$ and $\mathcal{Y}_d$ are of the same form, i.e.

$$\mathcal{Y}_d = \mathcal{Y}(Z_d) \qquad \ldots.(2.149)$$

$$\mathcal{Y}_1 = \tfrac{1}{2}(\mathcal{Y}(Z_a) + T_{pq}\, \mathcal{Y}(Z_b)) \qquad \ldots.(2.150)$$

$$\mathcal{Y}_1 = \mathcal{Y}(Z_c) \qquad \ldots.(2.151)$$

In this special case, if the beams are normalised such that

$$\langle \mathcal{Y}^{*}(Z) | \mathcal{Y}(Z) \rangle = +1 \qquad \ldots.(2.152)$$

then

$$K = |\langle \mathcal{Y}_1^{*} | \mathcal{Y}_d \rangle|^{2}$$
$$= \tfrac{1}{4} |\langle \mathcal{Y}^{*}(Z_a) | \mathcal{Y}(Z_d) \rangle + T_{pq} \langle \mathcal{Y}^{*}(Z_b) | \mathcal{Y}(Z_d) \rangle|^{2} \qquad \ldots.(2.153)$$

In an earlier section it proved convenient to define the complex variable, G, such that

$$N_{pq} = \tfrac{1}{2}(1 + T_{pq}.\mathrm{Real}[G(Z_a,Z_b).\exp(jk(Z_a-Z_b))])$$

and it was shown that as $kw_o \to \infty$, $G \to 1$, irrespective of the beam's mode-composition.

For beams which can be regarded as pure fundamental Gaussian mode it was shown (expression 2.96) that

$$G(Z_1,Z_2) = (1 + (j/kw_o^{2})(Z_2-Z_1))^{-1}$$

If, therefore, $\mathcal{Y}(Z_a), \mathcal{Y}(Z_b), \mathcal{Y}(Z_d)$, may be regarded as circularly symmetric fundamental Gaussian beams sharing the same

beam waist size, w_o, then

$$K = \frac{1}{4}\left| \frac{\exp(jk(Z_a-Z_d))}{(1+(j/kw_o^2)(Z_d-Z_a))} + T_{pq}\cdot \frac{\exp(jk(Z_b-Z_d))}{(1+(j/kw_o^2)(Z_d-Z_b))} \right|^2 \quad \ldots.(2.154)$$

The local maximum values of K and N_{pq} are therefore given by

$$N_{max} = \tfrac{1}{2}(1 + |G(Z_1,Z_2)|) \quad \ldots.(2.155)$$

$$K_{max} = \tfrac{1}{4}(|G(Z_a,Z_d)| + |G(Z_b,Z_d)|)^2 \quad \ldots.(2.156)$$

Fig 14 illustrates the variation of N_{max} and K_{max} (assuming $Z_d = \frac{1}{2}(Z_a+Z_b)$) as functions of $|(Z_a-Z_b)/(kw_o^2)|$. From this it may be seen that when $w_o^2 \gg |(Z_a-Z_b)/k|$, $N_{max} \simeq K_{max}$.

More generally we may arrange that Z_d be equal to either Z_a or Z_b. Under this condition

$$K_{max}(Z_a,Z_b,Z_d) = N_{max}(Z_a,Z_b) \quad \ldots.(2.157)$$

Hence under most circumstances we may regard N_{max} as the measure of the coupling efficiency which may be attained by a carefully designed system.

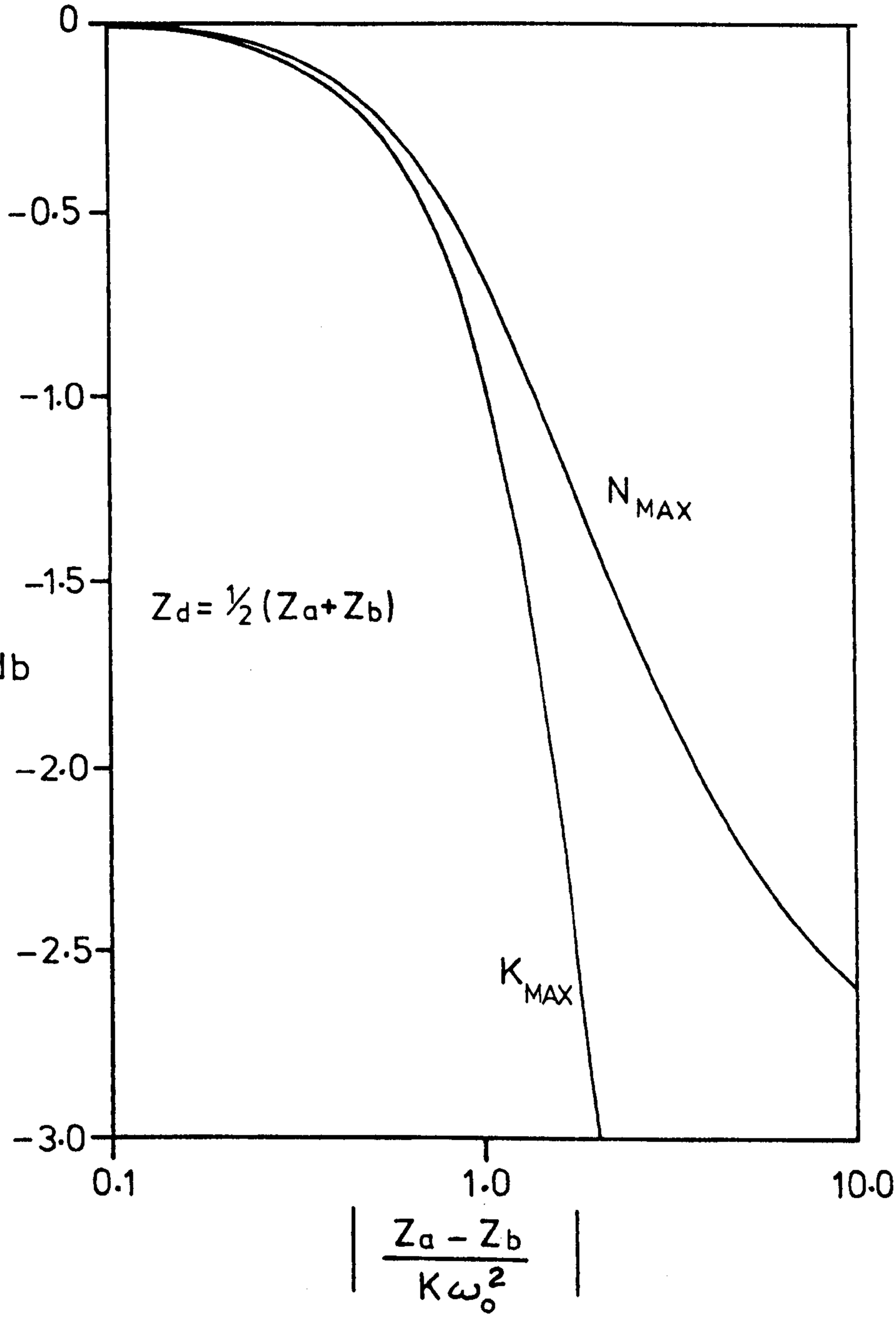
0
-0.5
-1.0
-1.5
-2.0
-2.5
-3.0
db
$Z_d = \frac{1}{2}(Z_a + Z_b)$
N_{MAX}
K_{MAX}
0.1
1.0
10.0
$\left| \frac{Z_a - Z_b}{K\omega_o^2} \right|$

Fig. 14.

2.6 Telescope efficiency and antenna pattern.

The optical arrangement by which power is coupled from a Cassegrain telescope onto the mixer may be illustrated by reference to Fig 15. Here γ represents the beam pattern of the mixer transformed by being passed through the diplexer and its associated optics.

In order to facilitate computation it is frequently convenient to imagine the mixer/diplexer combination being replaced by a transmitter arranged to radiate power along a beam, γ, equivalent to that of the receiver system. The antenna pattern, aperture efficiency, and beam efficiency of the resultant transmitter system may then be calculated. As this transmission system is distinguished from a receiver simply by the direction of power transport along the beam the values obtained are equal to those which would be obtained for the equivalent receiver.

The physical dimensions of a Cassegrain telescope are, in general, so much greater than the radiation wavelength that the system may be represented as shown in Fig 16a. Here the telescope is represented by an ideal lens adjacent to an emitting/absorbing centre-stop and aperture which is placed between the far-field pattern of the beam, γ, and the radiation incident upon the telescope. $\gamma(\theta)$ represents the far-field pattern in terms of a Gaussian mode set whose asymptotic 1/e - power beam angle is θ_s . θ_F and θ_s represent the apparent half-angles subtended by the outer edge of the telescope system and the centre-stop produced either by the secondary shadow or the finite size of the primary tunnel.

Power entering the telescope's antenna pattern can only be coupled to $\gamma(\theta)$ over the angular range $\theta_s \leq \theta \leq \theta_F$.

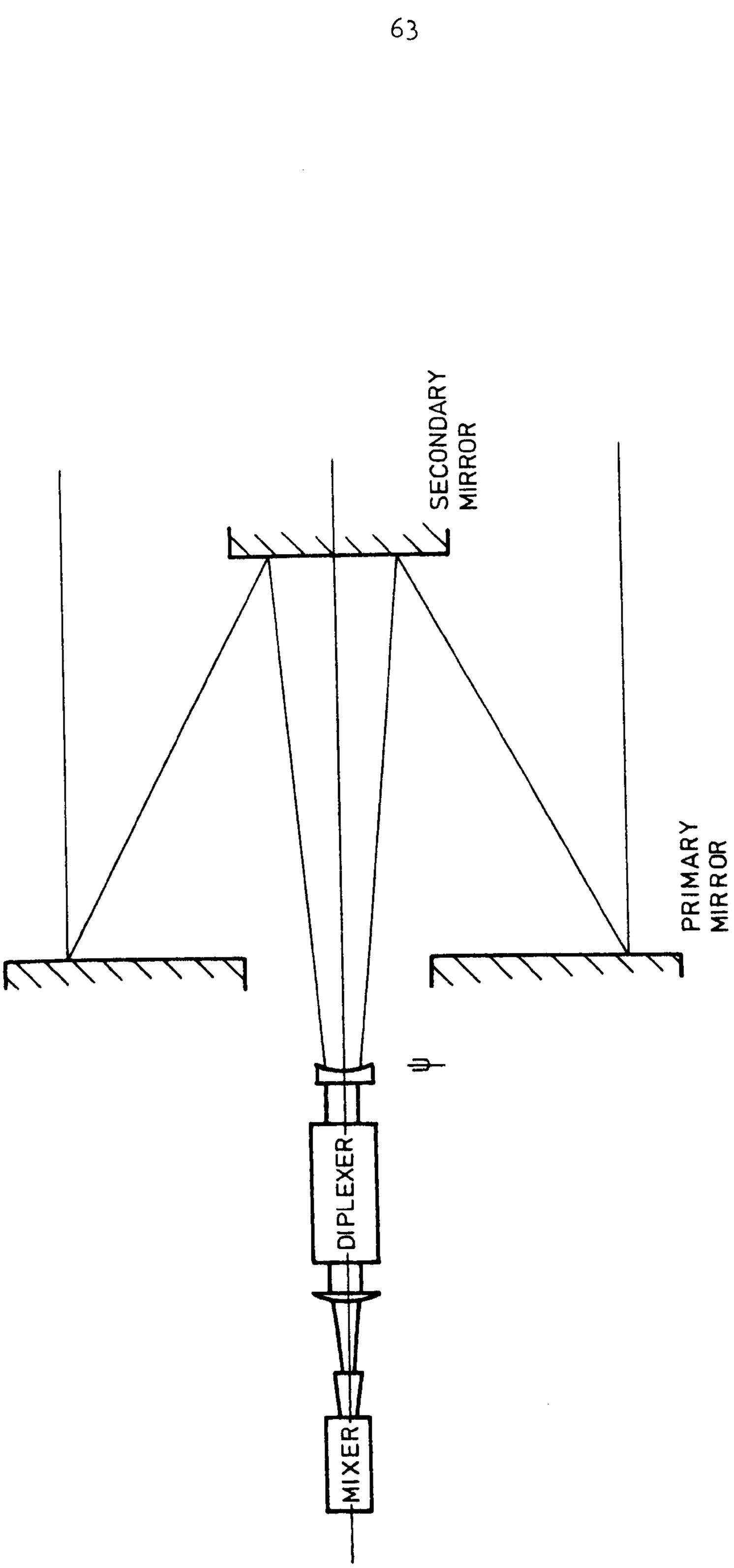

Fig. 15.
Telescope-mixer coupling via the Diplexer.

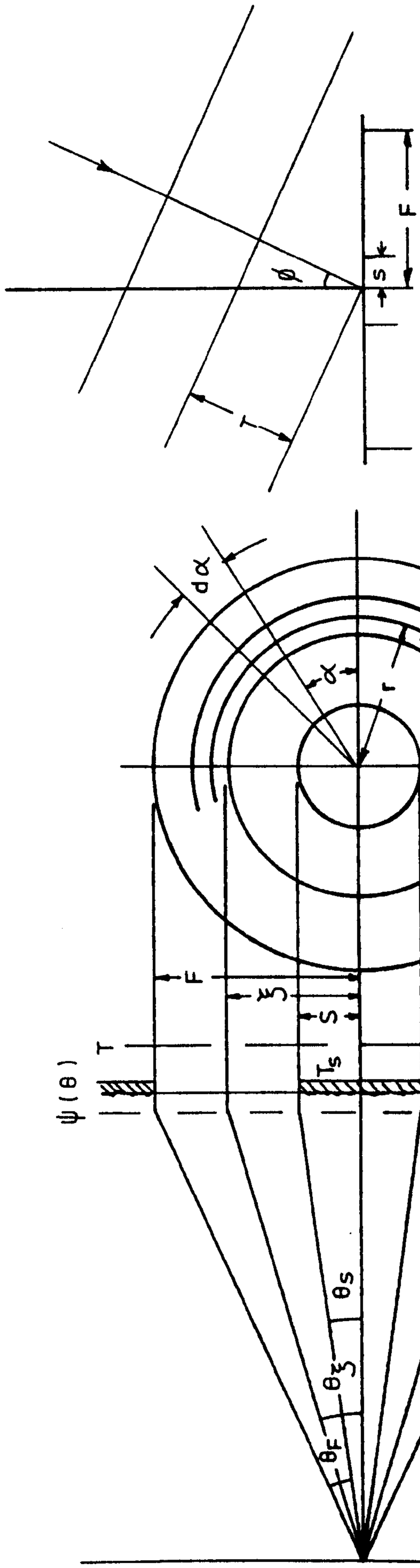

Fig. 16b.

Fig. 16a.

Beyond these limits power will be coupled to $\gamma(\theta)$ from other sources(here represented by the emissive aperture and stop of temperatures T_f and T_s)unless $\gamma(\theta) = 0$ in these regions.

In general the above constraint will not be satisfied and this causes the receiver to be sensitive to radiation which has not entered via the telescope's antenna patter and reduces its sensitivity to power which does flow in through the antenna pattern.

By reference to a standard discussion on the behaviour of radio telescopes(Kraus, J.D., Radio Astronomy, McGraw-Hill, London 1966)it may be seen that the antenna pattern and efficiency of a cassegrain telescope can be derived by regarding it as a plane annular region over which the electric-field distribution is given by the far-field pattern, $\gamma(\theta)$, of the receiver. For the sake of simplicity the electric field will be regarded as a scalar field with circular symmetry. From this it follows that the resultant antenna power pattern, $P(\phi)$, will have circular symmetry and be polarisation-independent.

Consider the situation illustrated in Figs 16a & 16b.

Fig 16a shows an annular region which represents the coupling plane between the receiver beam and a plane wave incident upon the plane at an angle ϕ to the normal. It is assumed that the curved telescope mirror surfaces result in the phasefront radius of curvature of the receiver beam being infinite at the coupling plane.

For a telescope system coupled to a Gaussian beam-set we may in general expect the conditions $\theta_1 \ll \pi$ and $\pi\theta_1^2 \gg \lambda/2\pi$ to be satisfied. Hence at the coupling plane $\theta = r/Z$ and $\gamma(\theta) = \gamma(r/Z)$.

The incremental contribution to the coupled aplitude, dE, of a small area (dr, $d\alpha$)located on the coupling plane at

(r,α) is given by an expression of the form

$$dE(r,\alpha) = \chi(r/Z)\exp(j(2\pi r/\lambda)\sin(\phi)\cos(\alpha))r\ dr\ d\alpha \quad \ldots.(2.158)$$

where it has been assumed that the $\alpha=0$ axis is parallel to the projection onto the coupling plane of the normal to the incident plane wave and that the plane wave's phase is zero at r=0.

The total amplitude coupling may therefore be obtained by integrating the incremental contributions over the annular region. i.e. the total coupling, $E(\phi)$, may be derived from

$$E(\phi) = 2\int_{S}^{F}\int_{0}^{\pi} dE(\phi) \quad \ldots.(2.159)$$

Now, as $\chi(r/Z)$ is circularly symmetric, for every position (r,α) where the contribution is as given by 2.158 we may find a corresponding position $(r,(\pi-\alpha))$ such that

$$dE(r,\alpha) = dE(r,(\pi-\alpha))^{*} \quad \ldots.(2.160)$$

Hence, upon summation the imaginary components of each incremental contribution has no effect upon the final value of $E(\phi)$. We may therefore write

$$E(\phi) = 2\int_{0}^{\pi}\int_{S}^{F} (r/Z)\cos((2\pi r/\lambda)\sin(\phi)\cos(\alpha))r\ dr\ d\alpha \quad \ldots.(2.161)$$

and the antenna power pattern $P(\phi)$ may then be defined as $P(\phi) = E(\phi).E(\phi)^{*}$.

From Kraus(ibid)we may define the beam solid angle, Ω_a, and main-beam solid angle, Ω_m, in terms of the normalised antenna

power pattern $P_n(\phi)$, where $P_n(\phi) = P(\phi)/P(0)$, by the expressions

$$\Omega_a = \int_0^{\pi} P_n(\phi)\sin(\phi)\, d\phi \qquad \ldots.(2.162)$$

$$\Omega_m = \int_0^{\beta} P_n(\phi)\sin(\phi)\, d\phi \qquad \ldots.(2.163)$$

where β is the smallest angle at which $P(\phi) = 0$.

The aperture efficiency, e_a, and beam efficiency, e_b, may then be defined as

$$e_a = \lambda^2/(A_p\Omega_m) \qquad \ldots.(2.164)$$

$$e_b = \Omega_m/\Omega_a \qquad \ldots.(2.165)$$

where A_p is the physical flux-collecting area of the telescope.

From the above it follows that Ω_a, Ω_m, e_a, e_b can all be calculated once $P_n(\phi)$ is known.

Now the signal beam associated with the diplexer/receiver systems which are the main subject of the work described in this thesis may be taken to be essentially pure fundamental Gaussian mode. i.e.

$$\gamma(\theta) = (1/2\pi\theta_s^2)\exp(-\tfrac{1}{2}(\theta/\theta_s)^2) \qquad \ldots.(2.166)$$

Hence, under this condition

$$P(\phi) = \left[\frac{1}{\pi\theta_s^2}\int_0^{\pi}\int_s^F \exp(-\tfrac{1}{2}(ur)^2)\cos((2\pi r/\lambda)\sin(\phi)\cos(\alpha)r\, dr\, d\alpha\right]^2$$

where u is defined to be such that $u = \theta_f/\theta_s$, and may be referred to as the underillumination ratio.

Fig 17 shows the normalised antenna pattern predicted from

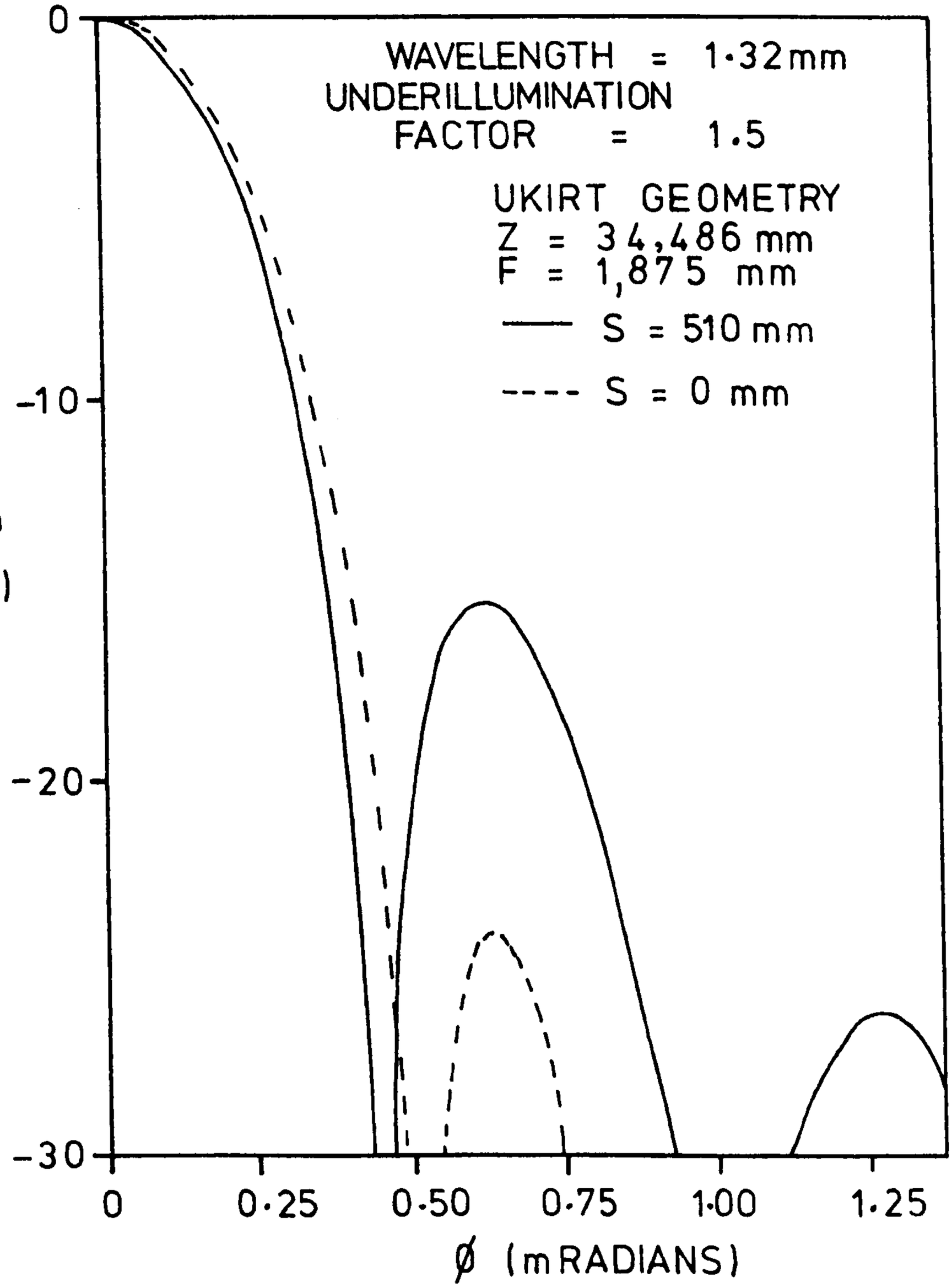

Fig. 17.
Theoretical antenna patterns.

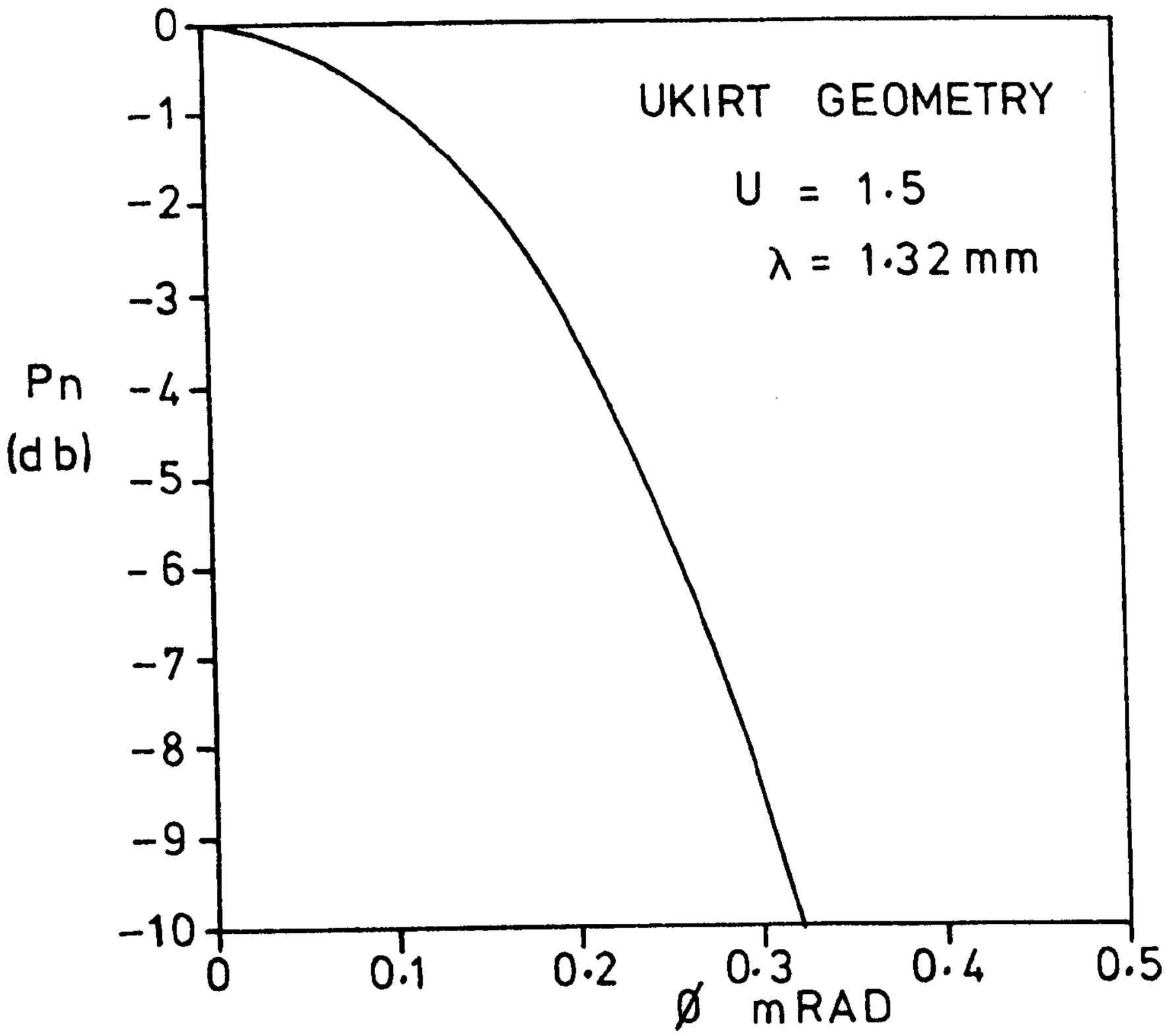

Fig. 18a.

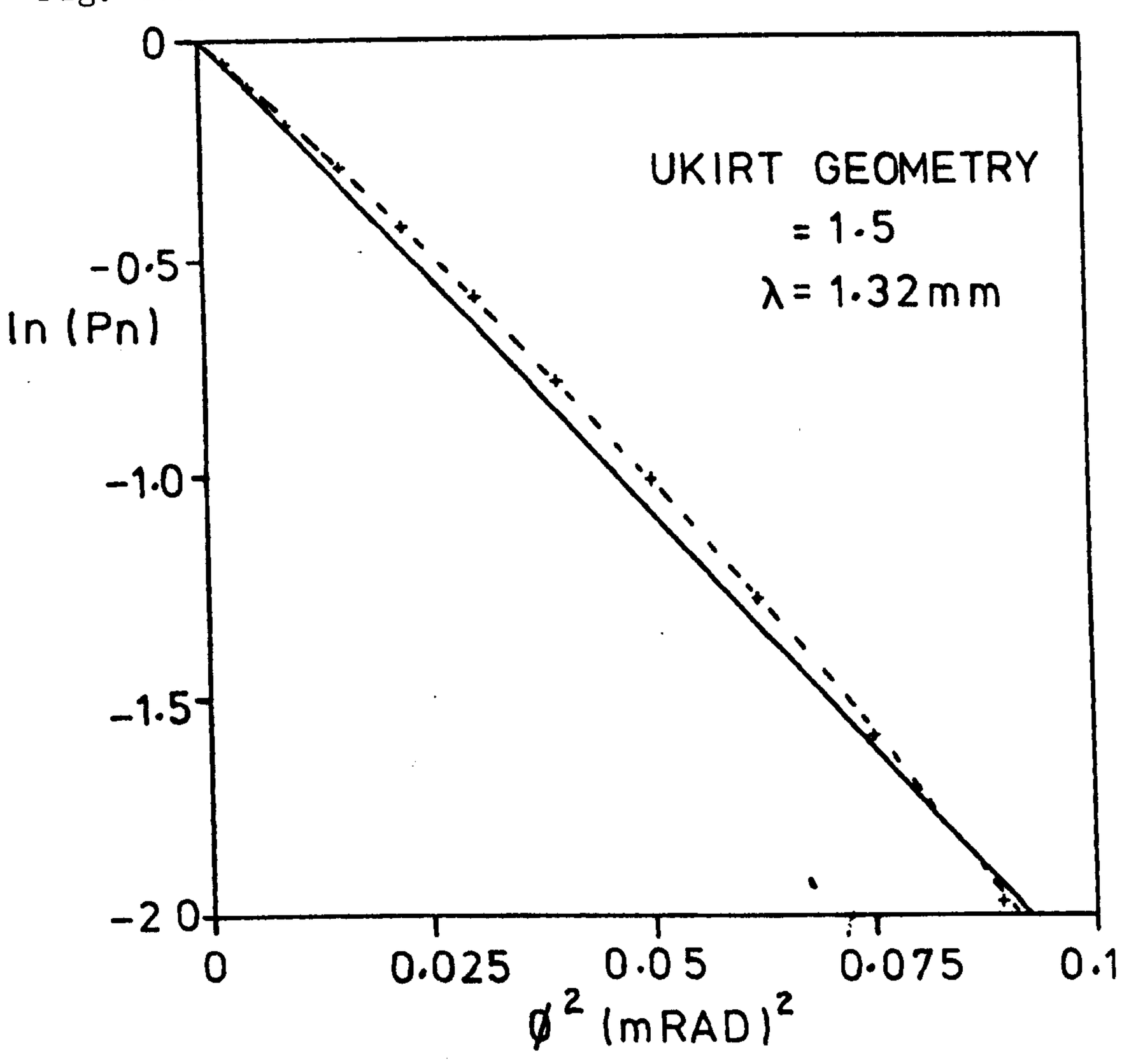

Fig. 18b.

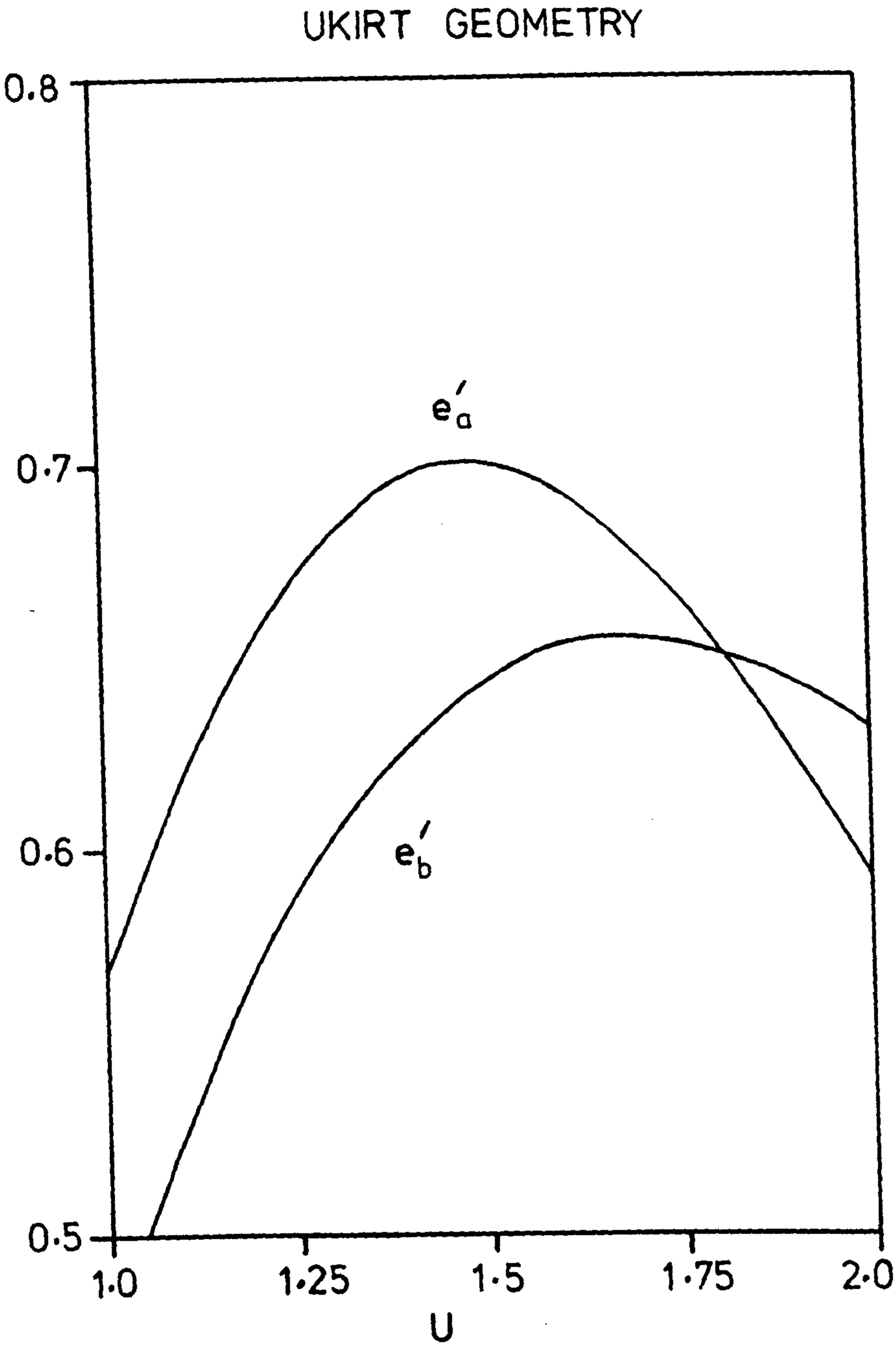

Fig. 19.
Telescope efficiency.

a numerical evaluation of the above integral for the United Kingdom Infra-Red Telescope's effective geometry. The antenna pattern which would result if the centre-stop could be removed is also plotted for comparison. From this it can be seen that the centre-stop reduces the width of the main lobe and raises the level of the first sidelobe by 8 - 9 db.

Table 2.6.1 indicates the variation in antenna pattern which takes place as the underillumination ratio, u, is varied for a telescope of UKIRT geometry at a wavelength of 1.32mm.

Table 2.6.1

u	e_a	e_b	P_f	P_s	β"	α"
1.3	0.979	0.864	0.185	0.118	88.1	43.2
1.4	0.963	0.868	0.141	0.135	89.9	43.8
1.5	0.944	0.866	0.105	0.154	92.2	44.4
1.6	0.923	0.870	0.077	0.173	92.8	45.1
1.7	0.899	0.872	0.056	0.193	93.4	45.9

P_f and P_s are the fractional power coupling into the Gaussian receiver beam from the regions beyond the aperture rim and within the centre-stop respectively. i.e.

$$P_f = \exp(-(\theta_f/\theta_\xi)^2) \quad \ldots.(2.167)$$

$$P_s = 1 - \exp(-(\theta_s/\theta_\xi)^2) \quad \ldots.(2.168)$$

β indicates the location of the first zero in the antenna pattern and hence defines the outer limit of the main lobe. α is the 1/e power half-angle of the Gaussian which is a best fit to the actual antenna pattern in the region $0 \leq \phi \leq 0.3$ mRad (62"arc).

Fig 18a shows the central portion of a typical UKIRT antenna

pattern. Fig 18b compares this(broken line)with the Gaussian (solid line)obtained from the least-squares fitting routine employed to produce the ✂ values quoted in Table 2.6.1. As may be seen from this example, the central portion of the antenna pattern is closely Gaussian under these conditions.

Now the value of u that results in the most effective useage of the telescope will depend to some extent upon the tasks to which the system is to be applied.

From Kraus(ibid), when observing an object whose angular size is negligible in comparison with the size of the main lobe, the maximum detected power will vary in proportion to $e_a(1-(P_f+ P_s))$, and when the object and main lobe sizes are similar this expression may be replaced by $e_b(1-(P_f+ P_s))$.

For convenience we may now define the spillover efficiency, e_s, such that

$$e_s = (1-(P_f+ P_s)) \quad ....(2.169)$$

and the corrected antenna and beam efficiencies may be defined as $e'_a = e_a.e_s$ and $e'_b = e_b.e_s$ respectively.

Fig 19 shows, for the UKIRT geometry at 1.32mm wavelength, the variation of e'_a and e'_b as functions of u. It may be seen that, at u = 1.47 e'_a reaches a maximum value of 0.7 and e'_b = 0.64, and, at u = 1.68 e'_b reaches a maximum value of 0.656 and e'_a = 0.678. Selecting the value of u which maximises either e'_a or e'_b therefore results in the other falling no more than 3% below its maximum possible value. There are, therefore, no compelling reasons for choosing any particular value of u over the approximate range 1.45 to 1.7.

After some consideration it was decided to settle upon the value u = 1.5 as, by selecting u so as to favour maximising e'_a rather than e'_b, some small improvement may be expected in

the system's usefulness in mapping and detecting more distant, more compact sources. At u = 1.5, e'_a is only 2½% below its maximum attainable value and hence the degradation in the system's ability to detect extensive sources is negligible.

3.1. Design, Construction, and Laboratory Tests.

Two Diplexers were designed and constructed as a result of the work discussed in this thesis. The first was a laboratory prototype constructed to enable measurements to be made of the performance of each of the various optical elements in the Diplexer and its performance as an integrated system.

The prototype Diplexer was designed and constructed in the form of a set of optical components mounted onto a common flat baseplate. This physical arrangement was chosen in order to facilitate the examination of performance in a laboratory environment but was felt to be insufficiently robust for use on a telescope. Hence, once the initial laboratory tests upon the prototype were completed, a second Diplexer was designed and constructed for use on UKIRT.

The UKIRT Diplexer, although different in physical construction, is optically very similar to the prototype and laboratory tests upon each of the systems and their individual components gave essentially identical results. In the following sections, therefore, the laboratory tests described and the results obtained refer - unless otherwise stated - to both Diplexers.

3.2. Polariser Grids.

Both the theory and the practical performance of free-standing wire grids have received considerable attention in the literature. (See, for example, Larsen, T., I.R.E. Trans. M.T.T. 191 (1962) for a review of the theory, and Costley, et al Second Int. Conf. Submillimetre Waves, Puerto Rico 1976 for a description of their construction and measured performance.)

For perfectly conducting metal wires of circular cross-section arranged in a plane parallel array we may write(Lamb, H., Proc. London Math. Soc. 29 523 (1898))

$$R_p = \left(1 + \left(\left(2d/\lambda \right) \ln\left(d/\left(2\pi a \right) \right) \right)^2 \right)^{-1} \qquad \ldots.(3.1)$$

$$R_t = \left(2\pi^2 a^2/(\lambda d) \right)^2 \left(1 + \left(2\pi^2 a^2/(\lambda d) \right)^2 \right)^{-1} \qquad \ldots.(3.2)$$

where, if λ is the radiation wavelength, d is the grid constant(wire interval), and a is the radius of the wires, then R_p and R_t are the power reflectivity for incident waves whose electric vectors are respectively parallel and transverse to the wire axies.

For an ideal polariser we would require that $R_p = 1$ and $R_t = 0$. This implies that we may optimise the performance of a wire grid by arranging that $a/\lambda \rightarrow 0$, and $d/\lambda \rightarrow 0$, as this leads to $R_p \rightarrow 1$ and $R_t \rightarrow 0$.

The smallest wire diameter and winding pitch that proved convenient in practice correspond to a = 5 microns and d = 25 microns, for which - at a wavelength of 1.32mm - the above expressions predict $R_p = -0.0003$db and $R_t = -36.5$db.

A number of such grids were manufactured by myself for use in the prototype and UKIRT Diplexers employing a method similar

to that described by Costley et al.(ibid).

These grids consisted of Tungsten wire bonded onto steel frames with CIBA-GEIGY Araldite PZ820/HZ820 thinned down with Toluene. In order to ensure good bonding and an even wire pitch the frames were prepared as indicated in Fig 20.

The steel surface was initially polished flat and smooth. A central strip was then blasted for a few seconds with the finest available grade of sand(particles approx. 25 microns in diameter). The surface was then lightly repolished to obtain a surface profile similar to that illustrated in Fig 20b. The resultant surface should be without any proud roughness that might disturb the wire pitch but has a roughened area that assists in keying the Araldite onto the steel frame. A sand-blasted top-frame was then bonded onto the grid as indicated by Fig 20c.

The transmission and reflection properties of the grids were then determined with an experimental arrangement illustrated in Fig 21.

P1 and P2 represent the positions where two polarisers could be inserted into the beam between a signal source and Golay detector. The source lens/feed-horn combination was arranged so as to produce a quasi-parallel beam whose 1/e-power radius was approximately 15mm. The polarisers were angled at 45° to the beam-axis in order to avoid standing-waves and to mimic more closely the conditions of use within a Diplexer.

Initially only one polariser was placed in the beam and rotated about the beam-axis to determine its maximum and minimum transmissivity. The peak and minimum figures obtained in this way were -0.15 ± 0.01 db and -14.5 ± 0.5 db which implied poor performance. However it was observed that, when the initial

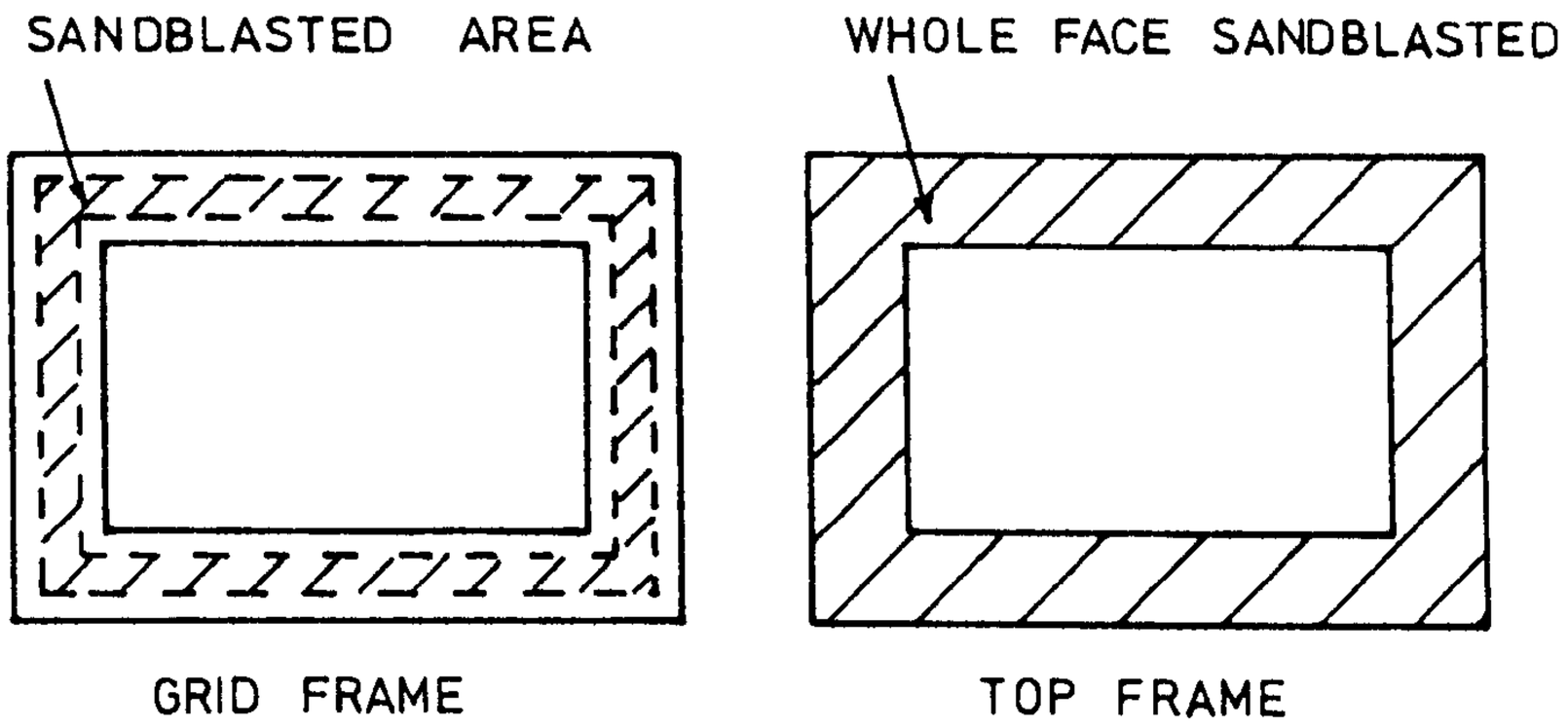

Fig. 20a.

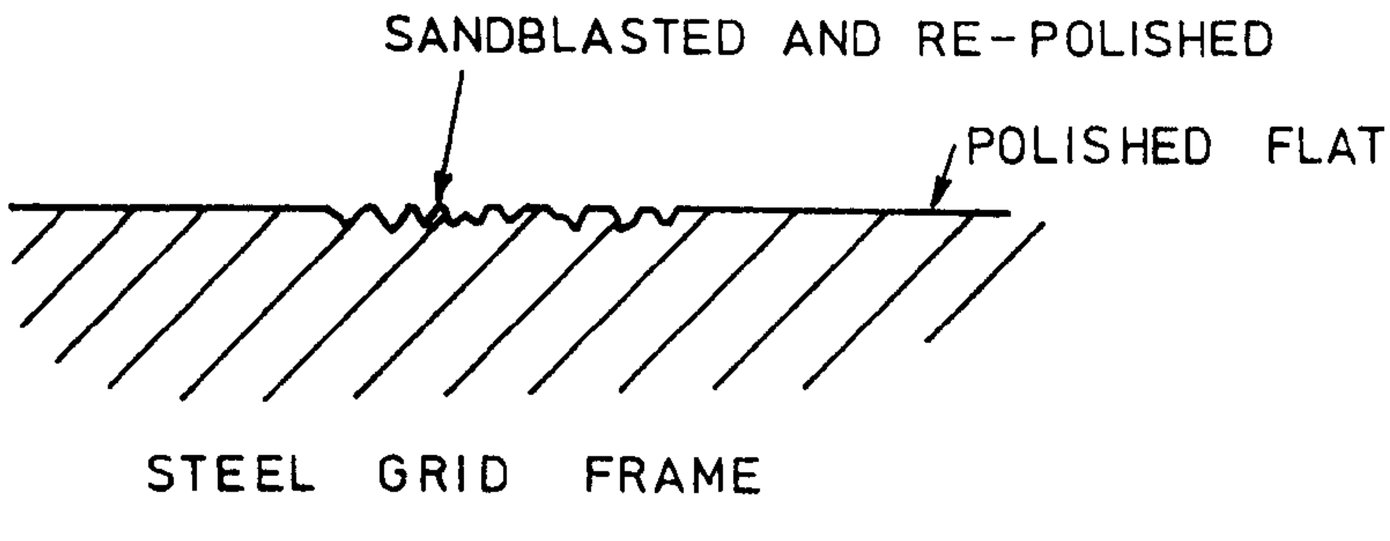

Fig. 20b.

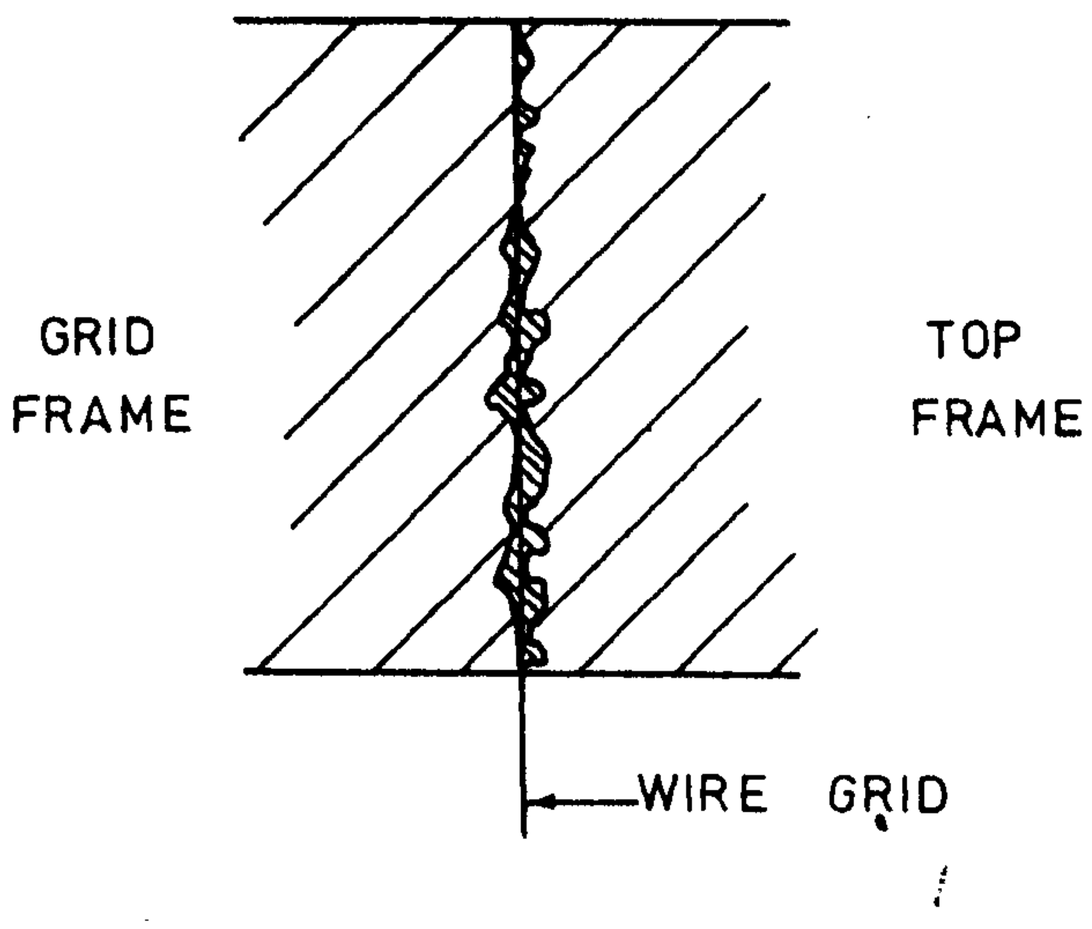

Fig. 20c.

Construction of polarisers.

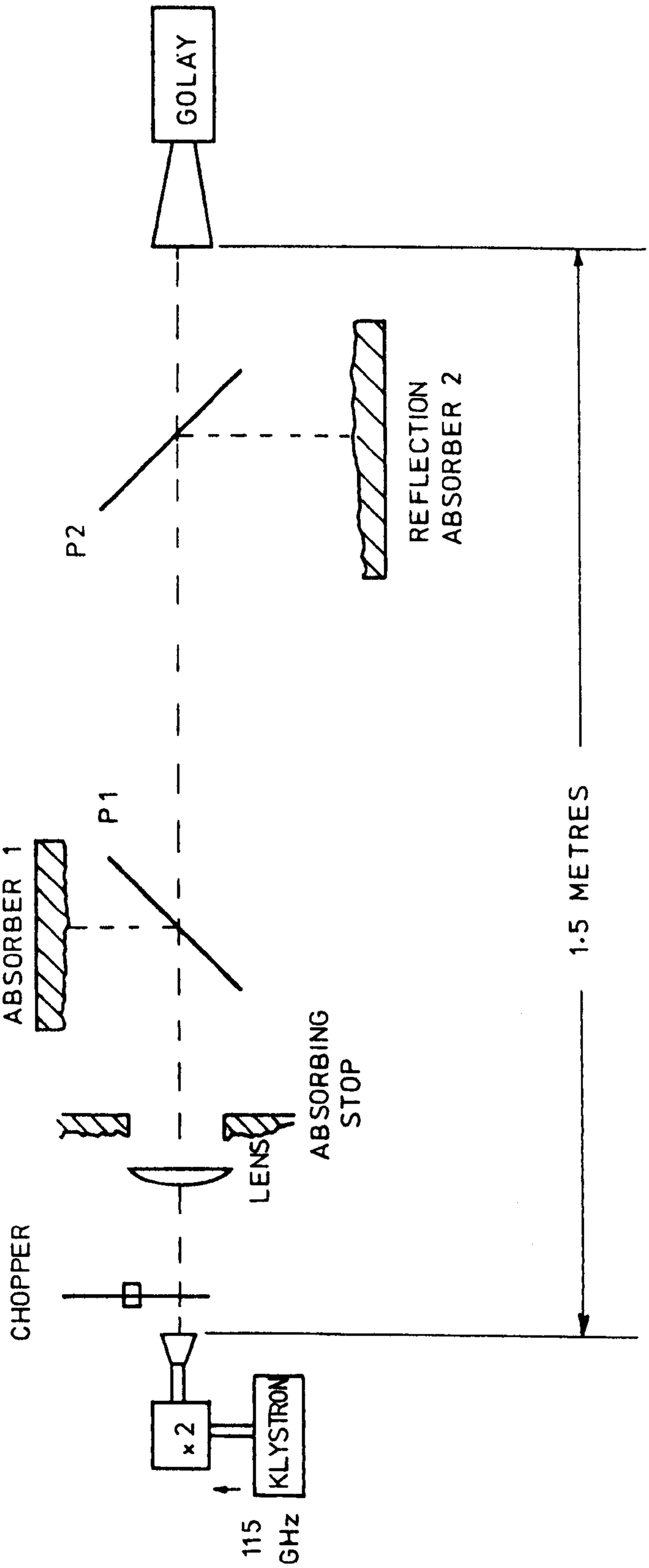

Fig. 21.
Polariser measurement system.

polariser, P1, was aligned for peak transmission, the addition of a second polariser, P2, similarly aligned, produced no measureable change(i.e. less than 0.01 db)in the transmitted power. Furthermore, when P2 was aligned so as to minimise the beam transmission the signal fell below the experimental system's noise floor of -32 db. Identical results were obtained when P1 and P2 were interchanged and when different polarisers were placed in each position.

From the above results it was decided that the power radiated by the signal source was not perfectly plane polarised and P1 was therefore required to ensure that the beam at P2 was satisfactorily polarised. This being done it was concluded that each grid exhibited a transmission loss of less than 0.01 db and a cross-polarisation leakage of less than -32 db at 230 GHz.

Reflection absorber 2 was then replaced with the Golay and the maximum and minimum power obtained by reflection from P2 were compared with the signal reflected by a plane mirror in position P2. Once again it was discovered that the polariser performance was better than the accuracy with which measurements could be made(i.e. a loss smaller than 0.01 db and a spurious reflectivity below -32 db).

Following these measurements it was concluded that the performance of each polariser was entirely satisfactory and probably approached the level predicted by the expressions due to Lamb(ibid).

3.3 Roof-Mirrors.

A roof-mirror consists of two metallic plane reflecting surfaces set at right-angles to each other.

At the surface of a perfect conductor the local electric vector must be perpendicular to the surface, hence the action of a roof-mirror upon a plane-polarised beam must be as illustrated in Fig 22. If, therefore, the plane of polarisation of the incident radiation is at 45° to the direction of the roof line then the incident and reflected beams are orthogonally polarised.

The roof-mirrors for both Diplexers were manufactured in Brass to the design illustrated in Fig 23. Each block was split along the plane AA' and the mirror faces were polished optically flat and smooth. The blocks were then reassembled and Gold-flashed to prevent the mirror surfaces from tarnishing.

Two laboratory tests were made upon the roof-mirrors to check their performance. The optical alignment and surface accuracy were first determined with a He-Ne laser as indicated in Fig 24a. The spot-diameter of the laser beam in the measuring plane was approximately 1.5mm.

Measurements made in this way established that the roof-mirrors were smooth, flat, and aligned to a total rms angular error of less than 8' arc.

The radio-frequency performance of the roof-mirrors was then tested as illustrated in Fig 24b. A harmonic multiplier diode was used in conjunction with a lens/feed-horn combination to produce a quasi-parallel beam whose 1/e power radius was approximately 5mm at a signal frequency of 230 GHz. Another lens/horn combination was then employed to couple this power into a Golay detector via either a plane metallic mirror or

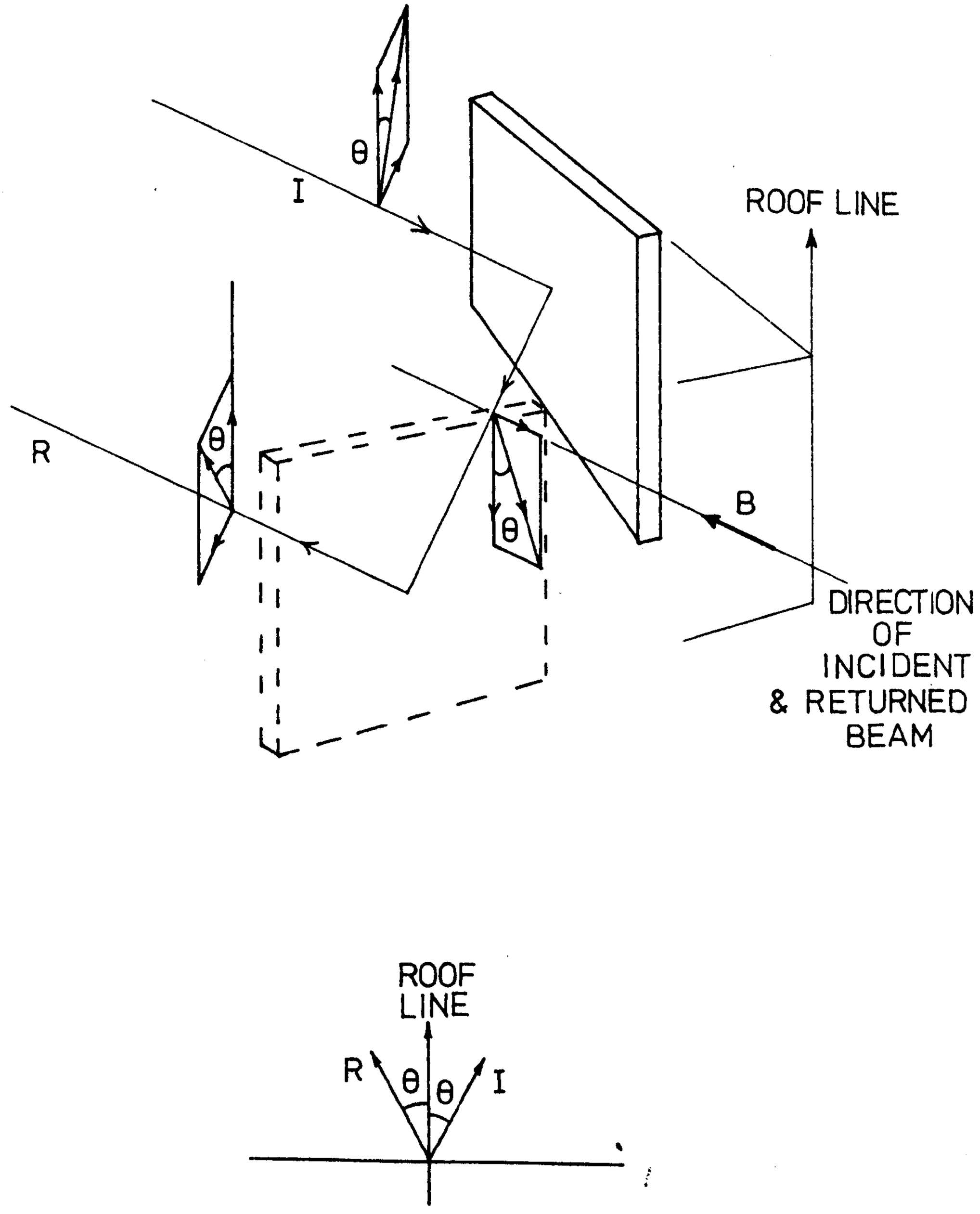

Fig. 22.
Action of a roof-mirror upon plane polarised radiation.

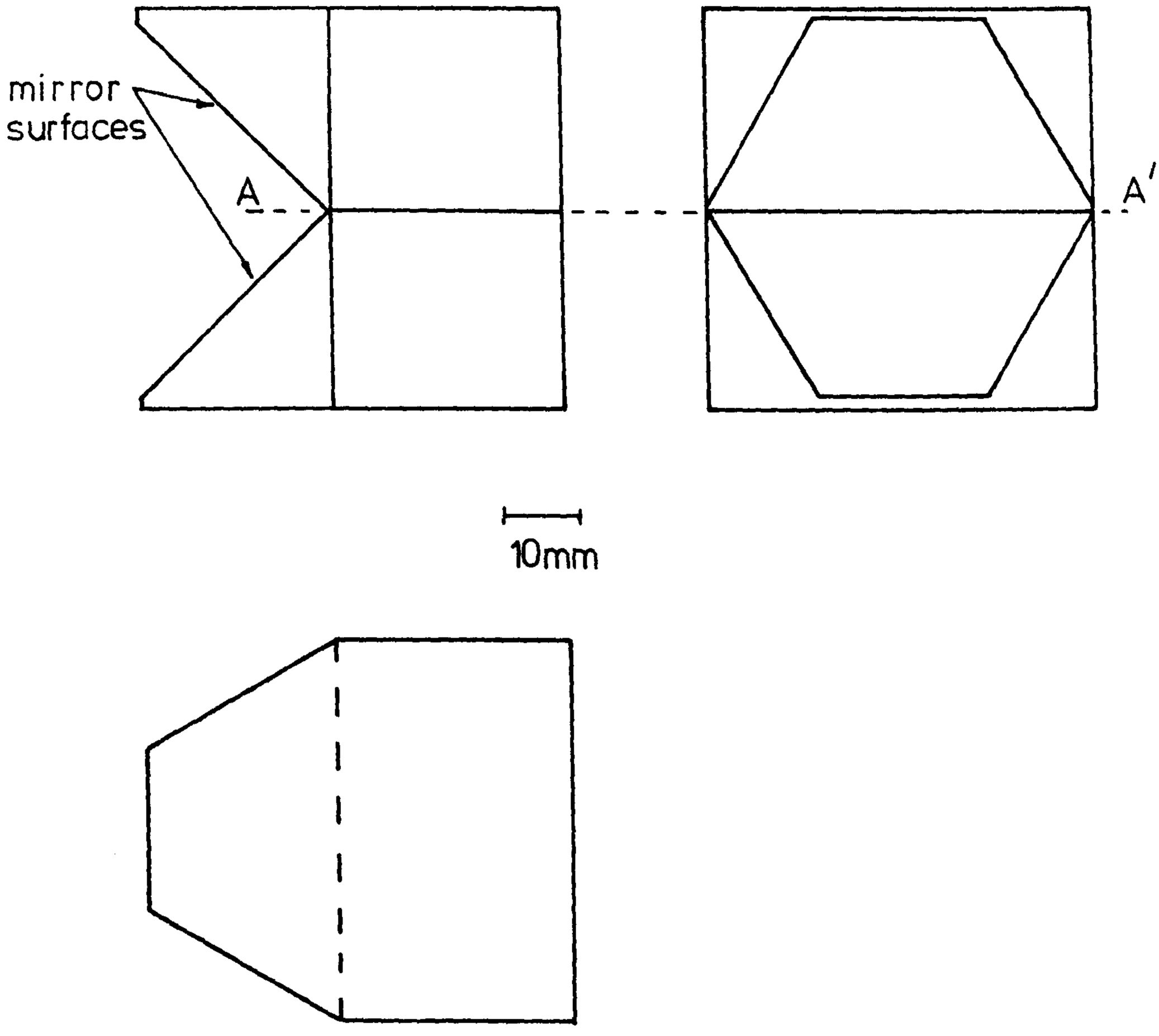

Fig. 23. ROOF MIRRORS

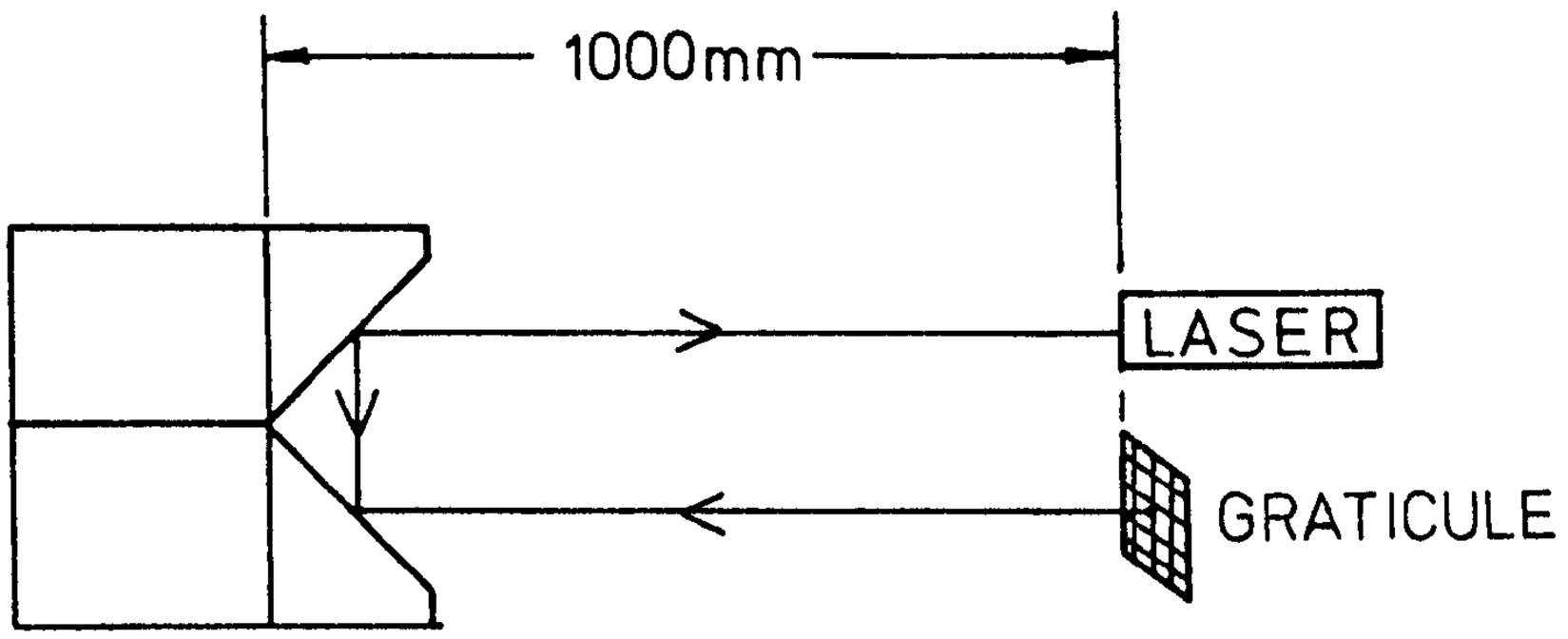

Fig. 24a.
Optical test of surface accuracy
and alignment of roof-mirrors.

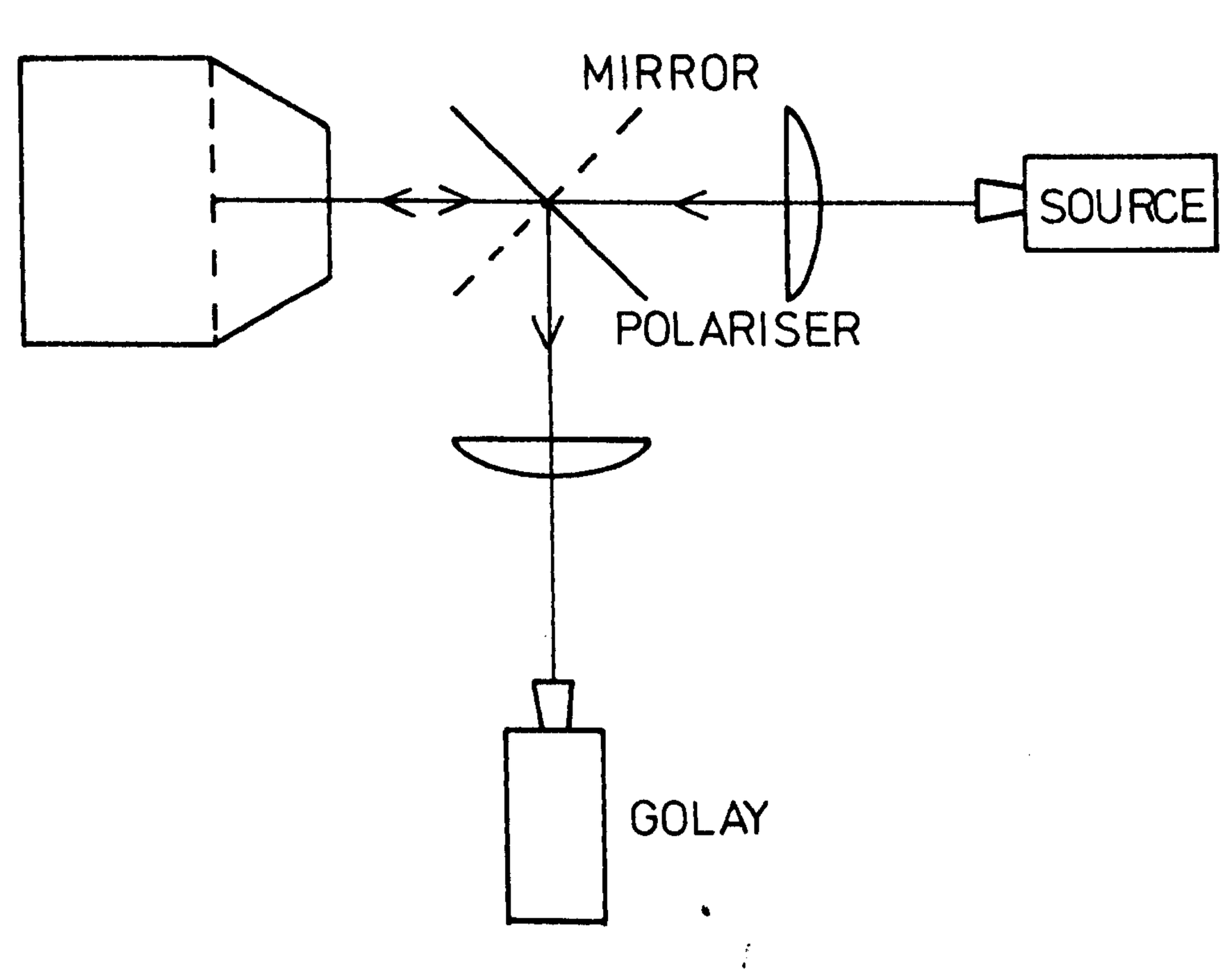

Fig. 24b.
Radio-frequency test of
roof-mirror performance.

a polariser and roof-mirror arranged as shown in Fig 24b.

Hence it was possible to examine the amount of signal lost by the roof-mirror as the polariser's performance was already known. Measurements made in this way established that the loss produced by the roof-mirror was less than -0.02 db.

3.4. Lenses.

The effectiveness with which power may be coupled via a lens depends as much upon the careful choice of a suitable lens material as it does upon the correct design and fabrication of an appropriate surface profile. Indeed, before the lens profile can be calculated it is first necessary to determine the refractive index of the chosen material at the radiation frequency of interest.

The selection of a suitable material is the subject of the following section. The design and construction of the lens geometry and its practical performance are then examined in section 3.4.2.

3.4.1. Measurement and Selection of Lens Material.

A considerable amount has been published on the far-infrared optical properties of a variety of potential lens materials. Of these, the four which have attracted the most interest are Quartz, TPX(an ICI trade-name for a Poly 4-Methyl Pentane-1 Polyolefine), PTFE, and Polyethylene(in both its High-Density (HDPE)and Low-Density(LDPE)forms).

Table 3.4.1 shows a brief but typical selection of data taken from the literature for these four materials. A number of other materials are also tabulated for comparison. This table only contains a small part of the data which has been published to date but it serves to indicate the range of values available in the literature.

The loss angle, d, is defined such that

$$d = \arctan(1.09856\, a/(nf)) \qquad \ldots.(3.3)$$

where f is the radiation freqency in GHz, at which

Table 3.4.1. Published far-infrared Optical Data.

Material (ref.)	HDPE[5]	HDPE[6]	HDPE[7]	HDPE[5]	Quartz[1a]	
Frequency (GHz)	220	3000	1500	1500	900	f
Refractive Index	--	1.55	1.518	--	2.107	n
Loss angle d(mRad)	0.18	--	2.9	0.42	0.37	d

	Quartz[1b]	Quartz[4a]	Quartz[4b]	TPX[2]	TPX[7]	PTFE[6]	Polypropylene[3]
f	900	900	900	1500	1500	1650	1200
n	2.154	2.113	2.156	1.43	1.447	1.46	1.4
d	0.37	0.75	0.05	4.8	13.2	5.3	0.81

	Sapphire[4a]	Sapphire[4b]	Germanium[4]	Silicon[4]	Kapton[7]	Surlyn[7]
f	900	900	900	900	1800	1500
n	3.069	3.415	4.006	3.4155	1.77	1.519
d	1.73	2.95	0.13	0.62	4.6	20.5

	Mylar[7a]	Mylar[7b]
f	1500	1500
n	1.717	1.752
d	24.1	23.6

N.B. The subscripts a and b refer to the ordinary and extraordinary rays respectively. The reference key is given below.

1. Russell, E.E., and Bell, E.E., J. Opt. Soc. Am. 57 341 (1967)
2. Chantry, G.W., et al Infra. Phys. 9 31 (1969)
3. Chantry, G.W., et al Infra. Phys. 11 109 (1971)
4. Loewenstein, E.V., et al Appl. Opt. 12 398 (1973)
5. Ayers, S., et al Proc. IEEE 121 1447 (1974)
6. Alvarez, J.A., et al Infra. Phys. 15 45 (1975)
7. Smith, D.R., and Loewenstein, E.V., Appl. Opt. 14 1335 (1975)

a is the absorption coefficient in db/cm, and n is the refractive index.

From an examination of this table it may be seen that the loss angles measured for HDPE, Quartz, and TPX are quite dissimilar from one report to another. To some extent this may be attributed to experimental errors, but the variations are so great that it seems probable that the optical properties of each material also vary quite considerably from sample to sample. Furthermore, the bulk of the published data has been taken at frequencies significantly higher than the 200-300 GHz range which is the primary interest here. It was therefore felt that some new measurements should be undertaken covering the appropriate frequency range and made upon the actual samples that could subsequently be made into the desired lenses.

Samples of HDPE, LDPE, PTFE, and Polystyrene(PS)were obtained from a variety of sources for testing. Each of the other materials listed in table 3.4.1. were considered and rejected because they were either too expensive, had too high a loss angle, or were strongly birefringent.

TPX is often used for far-infrared lenses as its behaviour at visible wavelengths is similar to its far-infrared performance. This makes TPX lenses particularly easy to align by eye. Here, however, it was felt that the Quasi-Optical system could be designed and constructed with sufficient accuracy that this advantage was irrelevant and TPX was rejected on the grounds of a high loss angle.

Quartz, although possessing a reasonably low loss angle, suffers from a number of disadvantages which, in combination, lead to it being rejected as a potential lens material. In addition to its birefringence Quartz is markedly more expensive

than the plastics with low loss angles. Furthermore, whereas the plastics may be formed by moulding or by cutting on a lathe or mill, Quartz must ground and polished to shape. Quartz lenses hence require significantly more time and expense to manufacture.

A number of samples of the following materials were obtained from the following sources.

B.P. Chemicals Ltd
HDPE: Rigidex-9 Cast Sheet, and Rigidex HO20-54P powder

Polypenco Ltd
HDPE: UHMWPE Extruded Rod(formed from Hercules 1900 UHMW pellets.)
PTFE: Extruded Rod
Crosslinked PS: Q200.5 Cast Rod

Bloor Ltd
HDPE: Extruded Rod

Rapra
LDPE: Pellets, types 1 and 2
HDPE: Pellets, types 1 and 2
PS: Cast Sheet

Hercules inc.
HDPE: 1900 UHMW Powder

Rapra LDPE was sucessfully cast into 100 x 100 x 45 mm blocks by filling a mould with pellets and placing in an oven at a temperature of 140^{o}C for a couple of hours. Oxidation produced a brown skin on the top surface of these blocks which was removed by machining away the top 10mm to leave a 100 x 100 x 35 mm block of homogeneous LDPE. Later samples of LDPE were cast under pressure at 140^{o}C in 5-10 mins in a system flushed with Nitrogen gas in order to prevent oxidation or decomposition. Subsequent measurements of the loss and refractive index showed no consistent differences that correlated with the change in forming process.

Attempts were made to cast HDPE in a similar manner but had to be abandoned as it proved impossible to form acceptable blocks within a reasonable timescale with the facilities available.

Blocks cast at atmospheric pressure were visibly inhomogeneous and remained so despite increases in temperature and casting time. Blocks cast under pressure were more homogeneous but were found to be filled with many small vacuoles. Hence when preliminary measurements indicated that samples of the HDPE extruded rods exhibited low loss angles it was decided that it was unnecessary to continue trying to form HDPE blocks by casting.

I should like to thank Dr D.A.Tod of Queen Mary College's Materials Dept. for his advice and assistance in casting samples of Polyethelene.

Test blocks were machined from each of the available pieces of material. Each block was 40mm in diameter and 10mm thick. The absorption coefficients of the Polyethylene samples were, however, so low that some extra blocks of greater thickness(25mm) were also made and tested to improve the accuracy of the measurements. The end faces of each block were machined smooth, flat, and parallel to a total error of less than 25 microns (typically the error was 5-10 microns).

The far-infrared properties of each of these blocks was then determined with a Michelson Interferometer system at the National Physical Laboratory. I would like to thank Dr J.R.Birch of the NPL for his assistance in performing these measurements.

Figs 25 to 30 show some of the results obtained from the experimental program. Two examples of HDPE and LDPE are shown in order to indicate the degree of variation measured from sample. Fig 25 compares the measured absorption coefficients of typical samples of each material while Figs 26 to 30 show the refractive index and loss angle of various samples plotted as functions of the radiation frequency.

Table 3.4.2 summarises the results of measurements made

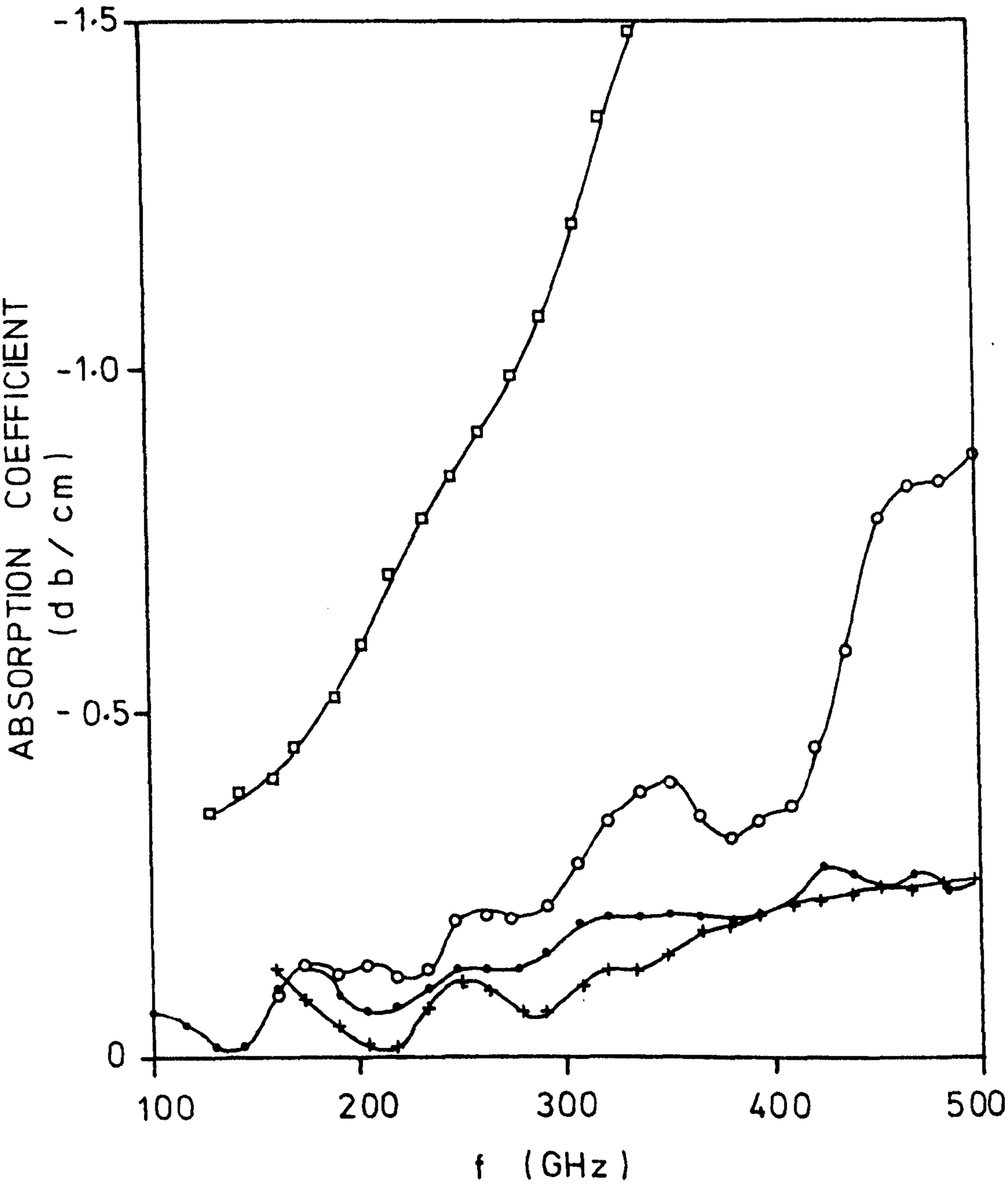

Fig. 25.
Comparison of the absorption coefficients of four different materials.

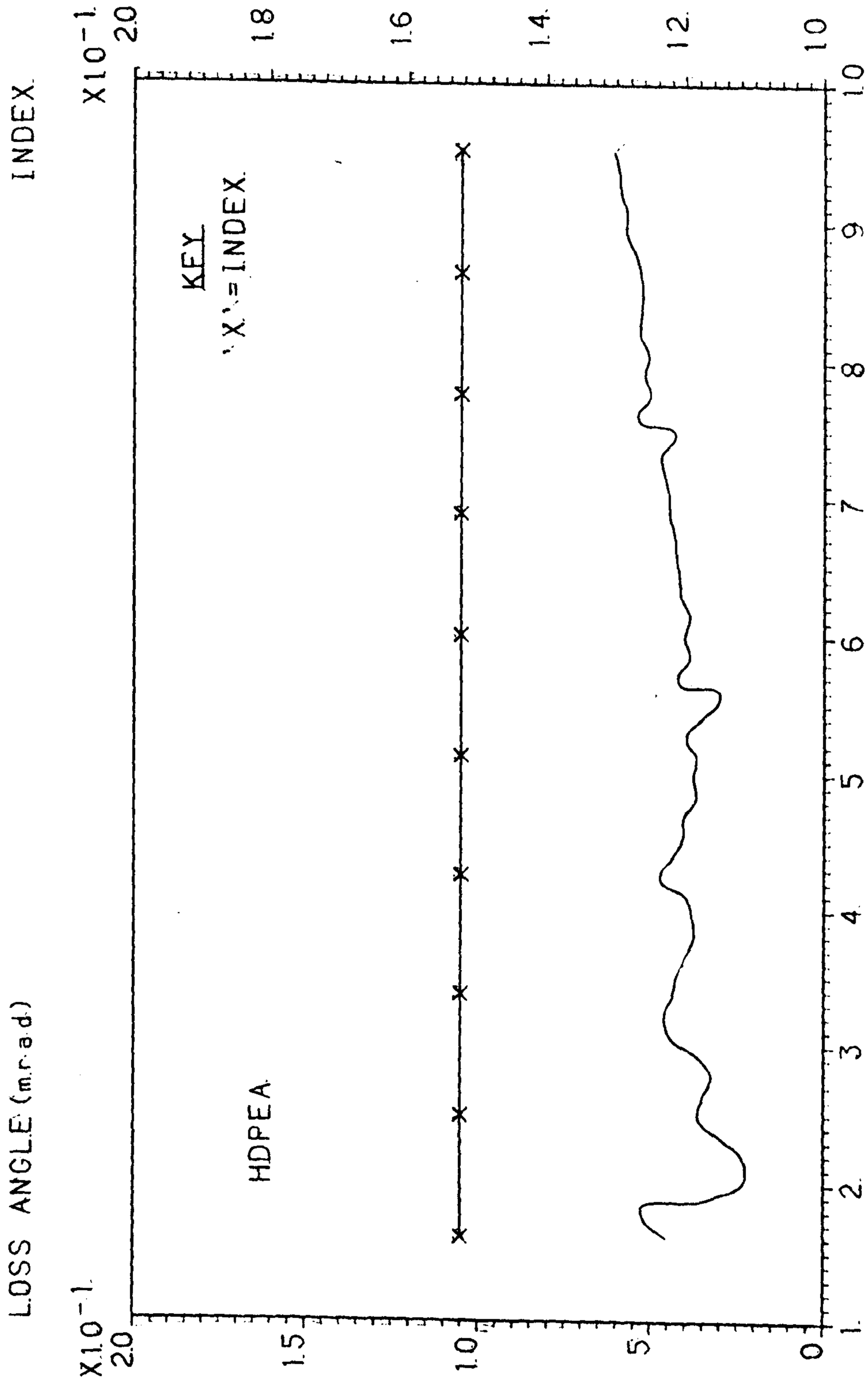
LOSS ANGLE (m.r.a.d)
INDEX
HDPEA
KEY
'X' = INDEX
FREQUENCY (GHz)
X10⁻¹
X10²
20
18
16
14
12
10
9
8
7
6
5
4
3
2
1
1.5
1.0
5
0

Fig 26

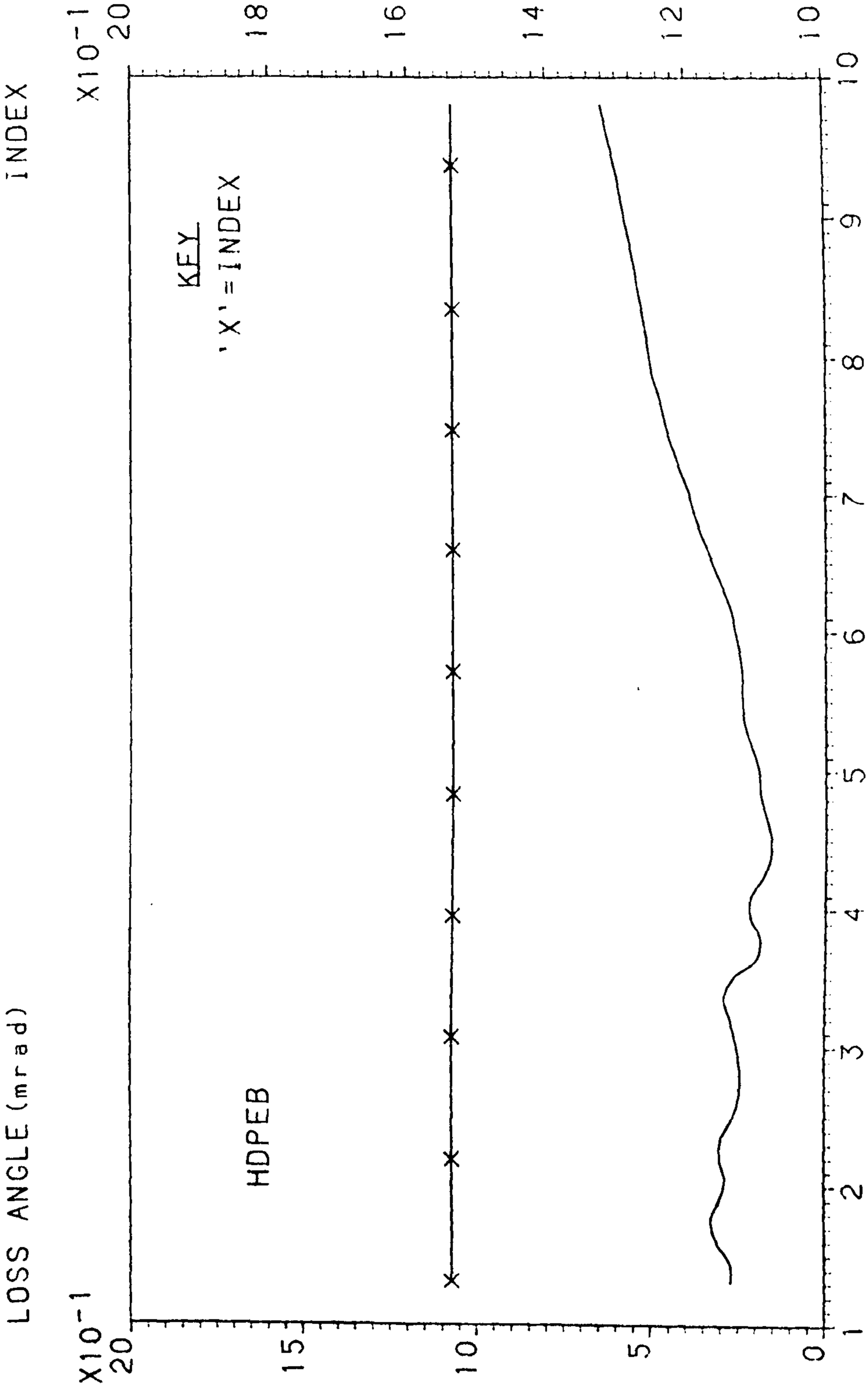
LOSS ANGLE (mrad)
X10⁻¹
20
15
10
5
0
INDEX
KEY
'X' = INDEX
HDPEB
FREQUENCY (GHz)
X10²
10
9
8
7
6
5
4
3
2
1

Fig 27

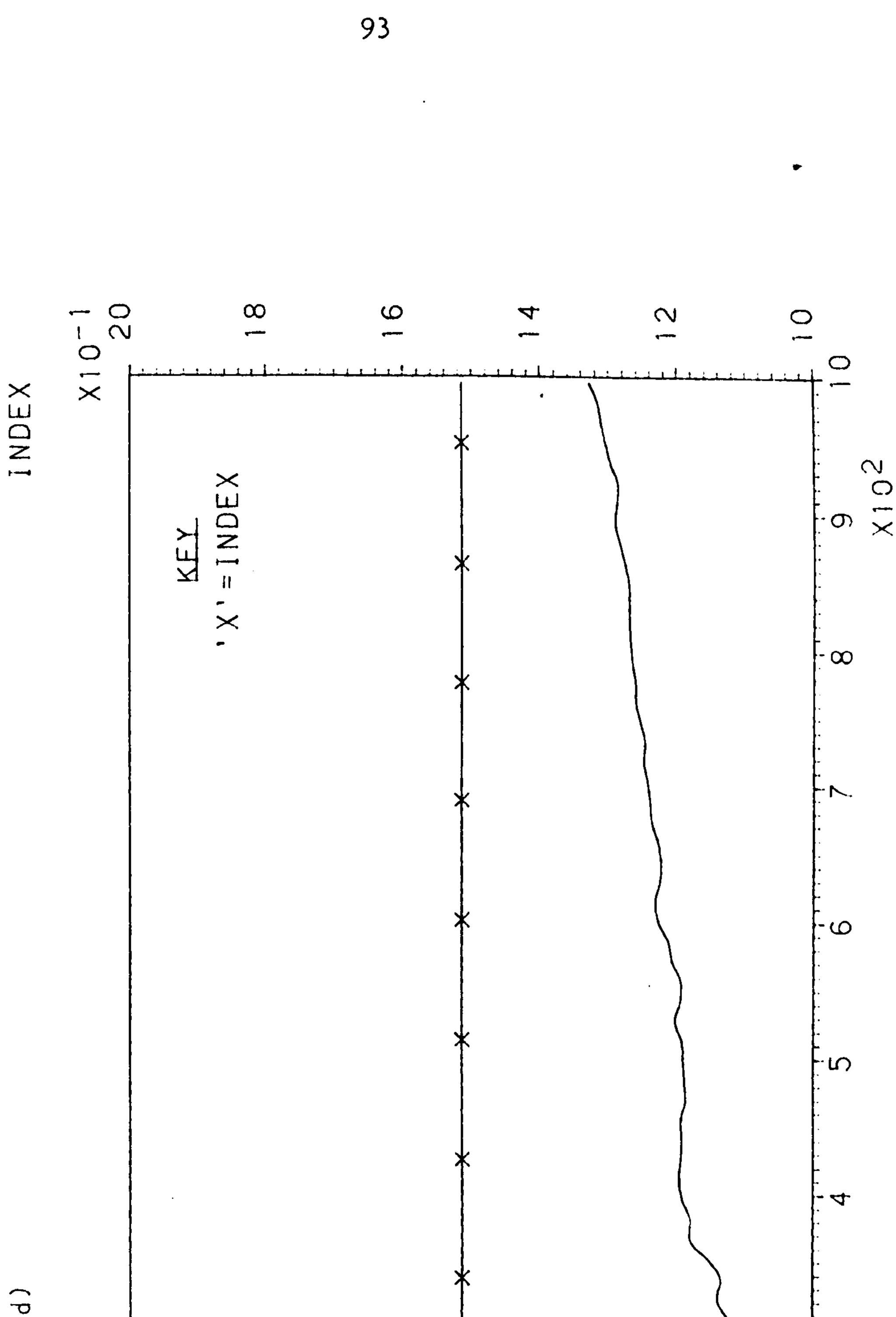
INDEX
X10
KEY
'X' = INDEX
LDPEA
LOSS ANGLE (mrad)
X10⁻¹
20
15
10
5
0
1
2
3
4
5
6
7
8
9
10
X10²
FREQUENCY (GHz)

Fig 28

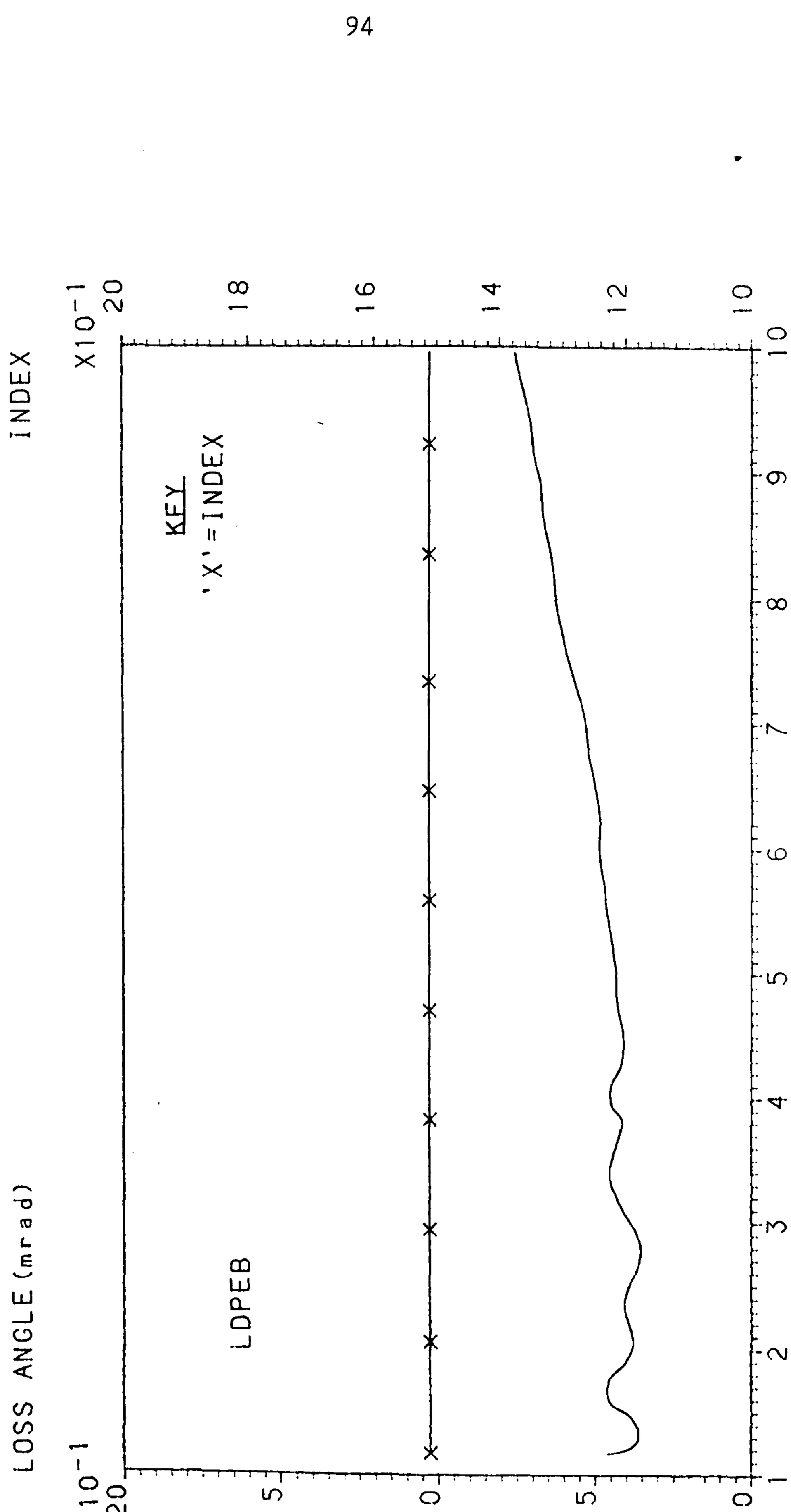
INDEX
X10
20
18
16
14
12
10
KEY
'X' = INDEX
X10²
10
9
8
7
6
5
4
3
2
1
FREQUENCY (GHz)
LDPEB
LOSS ANGLE (mrad)
X10⁻¹
20
15
10
5
0

Fig 29

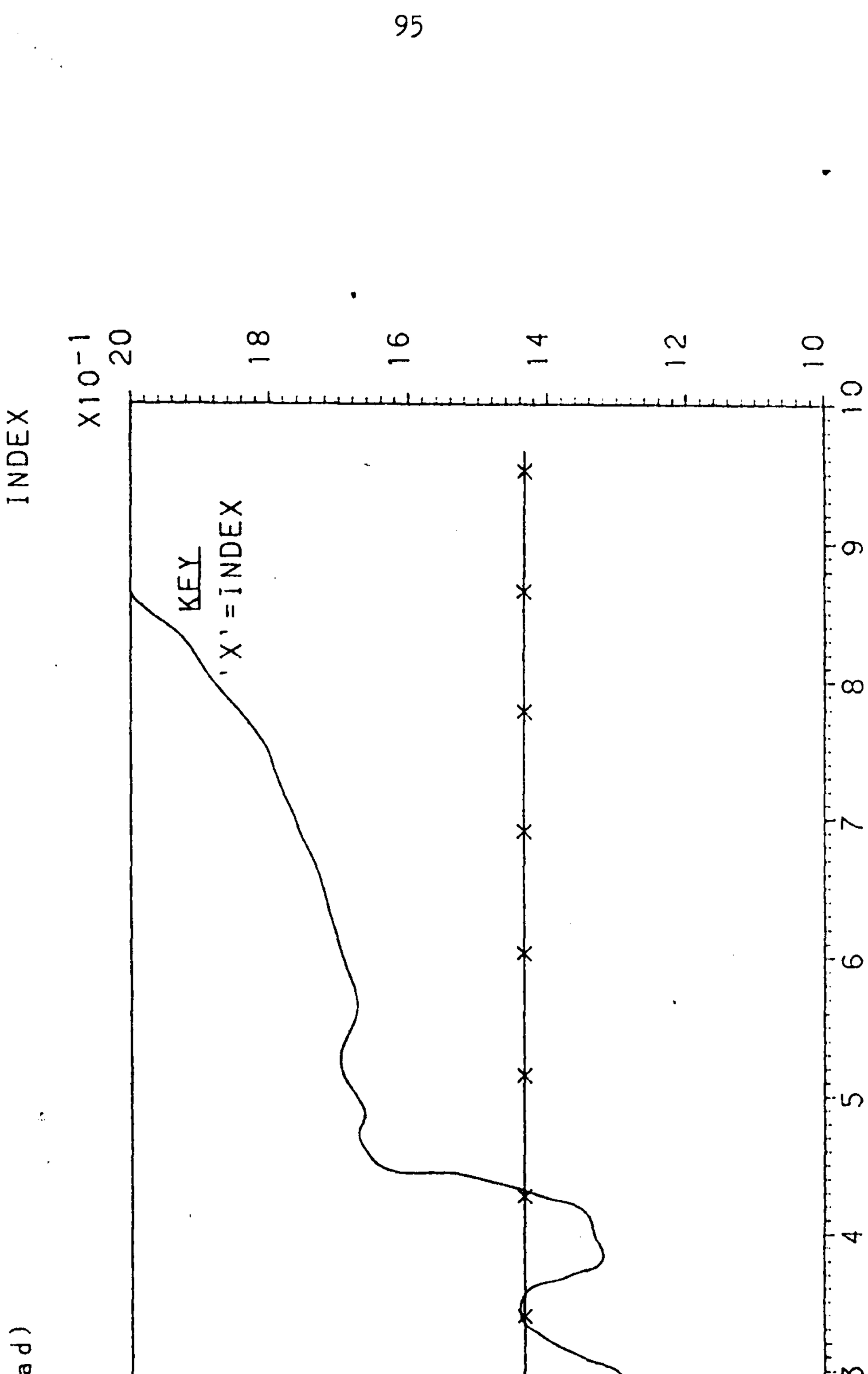
LOSS ANGLE (mrad)
X10⁻¹
20
15
10
5
0
INDEX
X10
20
18
16
14
12
10
KEY
'X' = INDEX
PTFEA
FREQUENCY (GHz)
X10²
10
9
8
7
6
5
4
3
2
1

Fig 30

upon each material. The values quoted in this table are averaged over the frequency range 150-500 GHz. The quoted uncertainties contain, in addition to the experimental errors, both the variations with frequency and from sample to sample.

Table 3.4.2. Measured far-infrared Optical Properties.

Material	HDPE	LDPE	PTFE	PS
n	1.530 ± 0.006	1.513 ± 0.001	1.433 ± 0.001	1.5915 ± 0.001
d(mRad)	0.30 ± 0.10	0.35 ± 0.15	0.81 ± 0.35	3.0 ± 1.0

The values given in the above table are not intended as definative measurements of the far-infrared properties of these materials as the number of samples tested is too small to fully assess the variations which may occur from sample to sample. However, the object of this program of measurements was to identify which of the materials could be employed to make satisfactory lenses for the task at hand. The results obtained indicate clearly that Polyethylene may be expected to absorb distinctly less of the radiation than either PTFE or PS, although the spread in the values obtained is sufficiently large that no clear preference emerges for either HDPE or LDPE. It was therefore decided that HDPE would be chosen as the lens material as it is much easier to machine accurately than LDPE and the finished lens is harder and more durable.

Now, at 250 GHz, d=0.3mRad implies that an HDPE lens 10mm thick will absorb approximately 0.1db($2\frac{1}{2}\%$)of the beam power. This is sufficiently small that it is quite acceptable under most circumstances. HDPE may therefore be regarded as a perfectly acceptable lens material for most applications in the 200-300 GHz frequency range.

3.4.2. Design, Construction, and Testing of Lenses.

A potential disadvantage of the lens is the loss of power coupling which may occur due to reflection at the dielectric interfaces between it and the surrounding medium.

Fig 3la illustrates this effect. Here a ray whose electric vector may be represented at the interface by the complex vector $\underline{A}$ is incident upon the interface between two media whose refractive indices are n_1 and n_2. This gives rise to two rays, one transmitted into the medium of refractive index n_2 and here represented by the complex vector $\underline{T}$, and the other reflected back into the medium of refractive index n_1 and represented by the complex vector $\underline{R}$.

From Born and Wolf(Principles of Optics. Pergamon Press London 4th ed.)page 40, we may write

$$T_p = \frac{2.n_1.\mathrm{Cos}(i)}{n_2.\mathrm{Cos}(i) + n_1.\mathrm{Cos}(t)} \cdot A_p \qquad ....(3.4)$$

$$T_q = \frac{2.n_1.\mathrm{Cos}(i)}{n_1.\mathrm{Cos}(i) + n_2.\mathrm{Cos}(t)} \cdot A_q \qquad ....(3.5)$$

$$R_p = \frac{n_2.\mathrm{Cos}(i) - n_1.\mathrm{Cos}(t)}{n_2.\mathrm{Cos}(i) + n_1.\mathrm{Cos}(t)} \cdot A_p \qquad ....(3.6)$$

$$R_q = \frac{n_1.\mathrm{Cos}(i) - n_2.\mathrm{Cos}(t)}{n_1.\mathrm{Cos}(i) + n_2.\mathrm{Cos}(t)} \cdot A_q \qquad ....(3.7)$$

where i is the angle of incidence, t is the angle of refraction of the transmitted ray, and, from Snell's Law

$$n_1.\mathrm{Sin}(i) = n_2.\mathrm{Sin}(t) \qquad ....(3.8)$$

The subscripts p and q denote the components of each vector which are respectively parallel and perpendicular to the plane

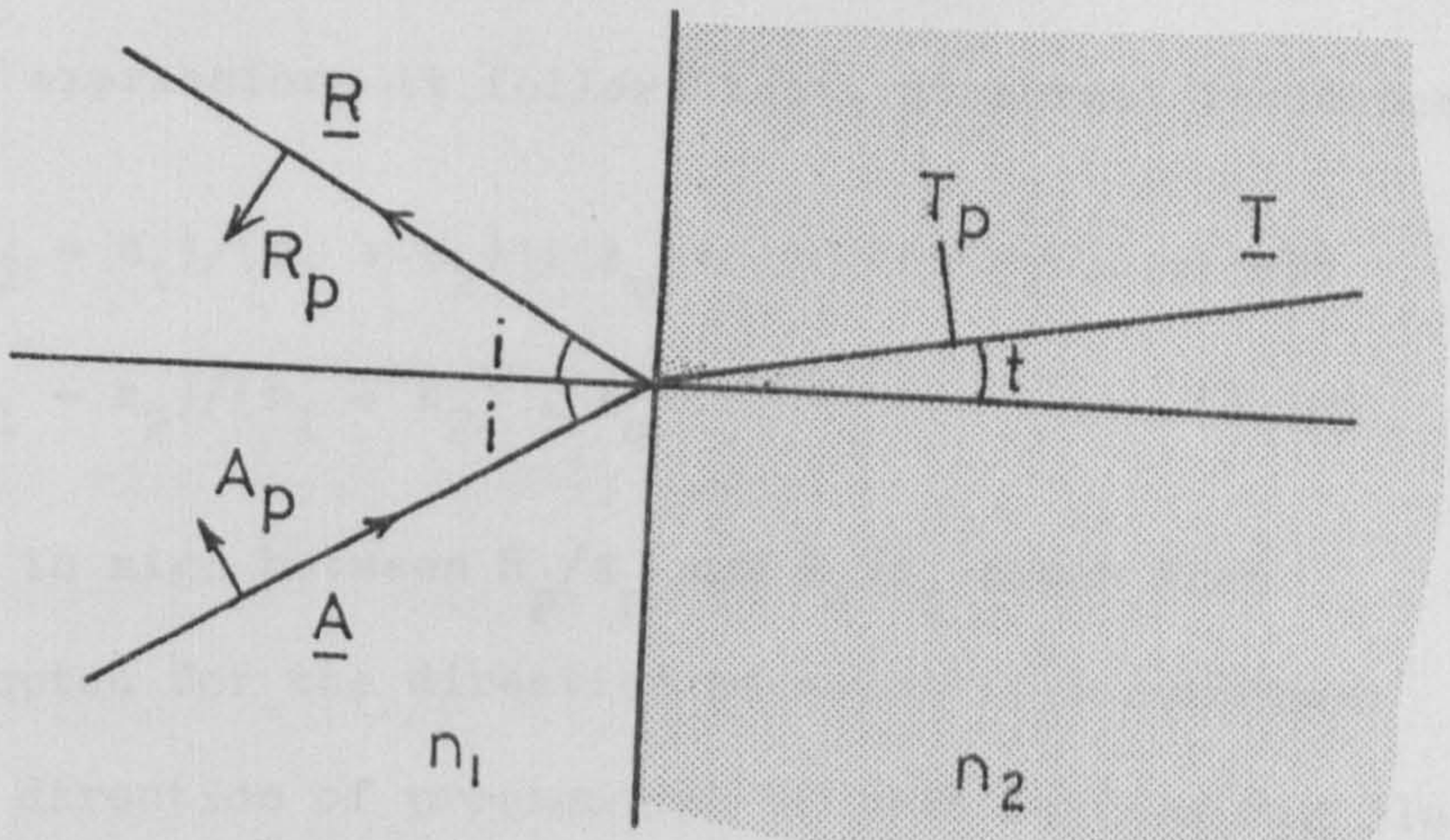

Fig. 31a.
Transmission and reflection at a dielectric interface.

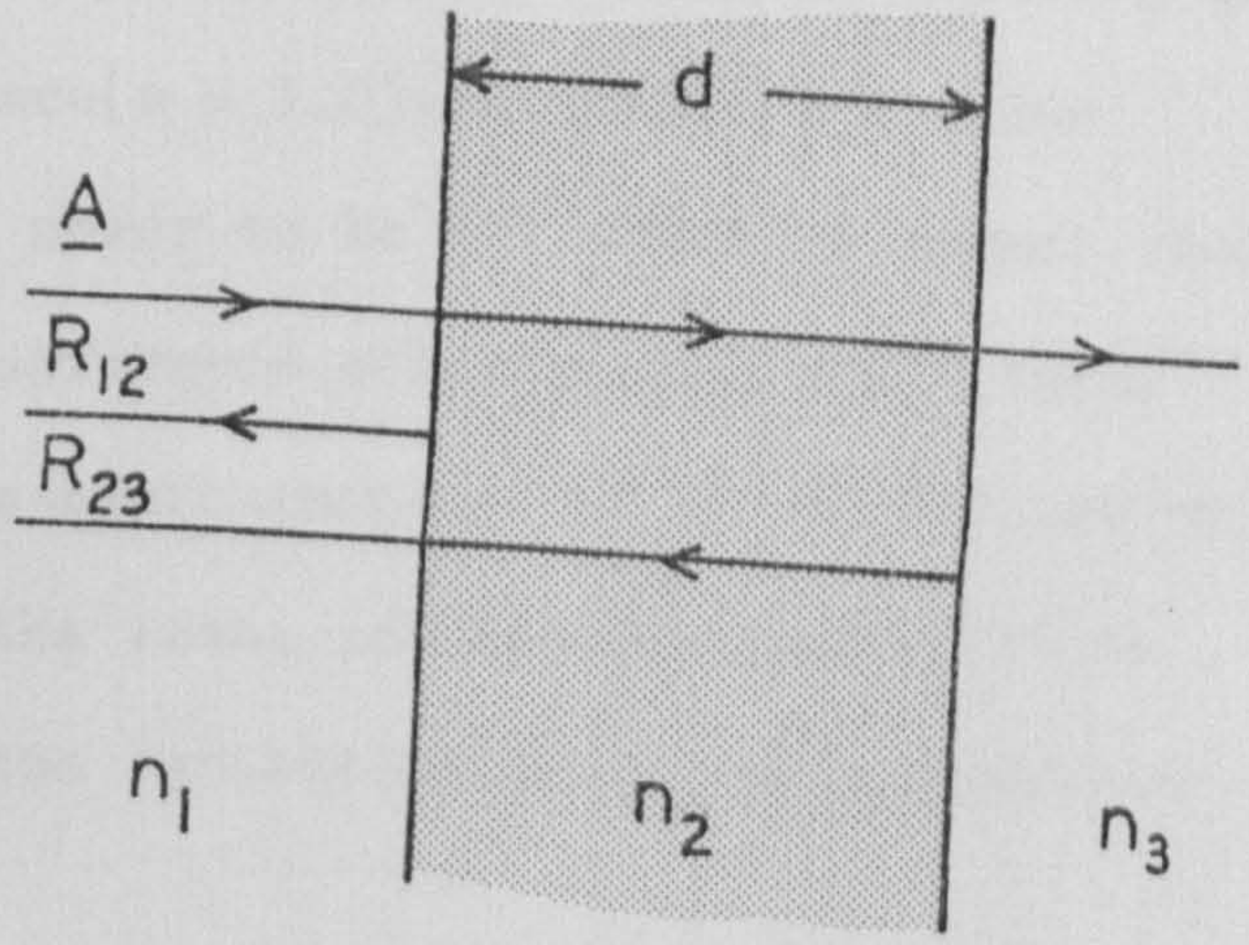

Fig. 31b.
Interference between the reflections from two parallel interfaces.

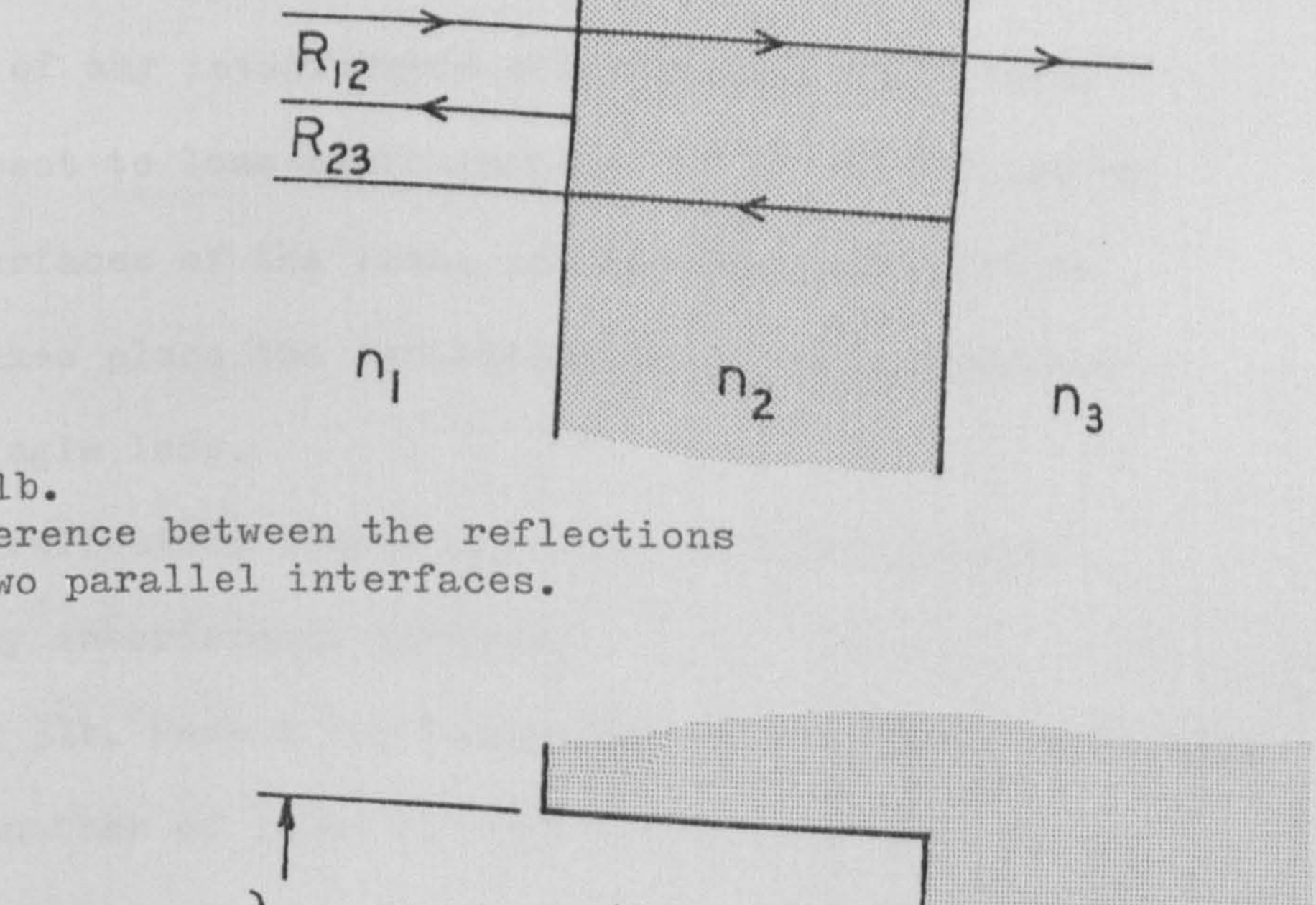

Fig. 31c.
Profile of a blazed surface.

of refraction.

From the above expressions it follows that, at normal incidence

$$R_p = (n_2 - n_1)/(n_1 + n_2) \cdot A_p \qquad \ldots.(3.9)$$

$$R_q = (n_1 - n_2)/(n_1 + n_2) \cdot A_q \qquad \ldots.(3.10)$$

The difference in sign between R_p/A_p and R_q/A_q comes from the convention adopted for the direction of a positive component as seen along the direction of propagation of each ray(see Fig 3la).

The fraction of the incident power of a normal beam which is reflected is therefore equal to $(n_1-n_2)^2/(n_1+n_2)^2$ irrespective of the polarisation of the incident wave. Hence in crossing an interface between free space(n = 1.0)and HDPE(n = 1.53)we may expect 0.23 db of the power to be reflected at normal incidence. In the absence of any interference effects this would imply that we may expect to lose approximately 0.5 db by reflection from the two surfaces of the lens, and if some constructive interference takes place the reflective loss could approach 0.8 db for a single lens.

Fortunately reflection losses may also be reduced quite significantly by interference effects.

Consider Fig 3lb. Here a ray passes from a medium of refractive index n_1 into another of index n_3 via a seperating medium of index n_2. By reference to a paper such as that by E.M.T.Jones and S.B.Cohn(J.Opt.Soc.Am. 26 452 (1955))we may define an overall power reflection coefficient, R^2, for this system such that

$$R^2 = \frac{(R_{12} + R_{23})^2 - 4.R_{12}.R_{23}.\mathrm{Sin}(x)}{(1 + R_{12}.R_{23})^2 - 4.R_{12}.R_{23}.\mathrm{Sin}(x)} \qquad \ldots.(3.11)$$

and

$$x = 2\pi d/\lambda \cdot (n_2^2 - \mathrm{Sin}^2(i))^{\frac{1}{2}} \qquad \ldots.(3.12)$$

where R_{12} and R_{23} are the amplitude reflection coefficients at the boundaries between the media as indicated in Fig 31b, λ is the radiation wavelength in free space, d is the thickness of the seperating layer, and i is the angle of incidence of the ray passing from the first region into the seperating layer.

From the above expressions it may be seen that $R^2 = 0$ if either $R_{12} = R_{23}$ and $\mathrm{Sin}^2(x) = 1$ or if $R_{12} = -R_{23}$ and $\mathrm{Sin}^2(x) = 0$. Hence the reflected power is zero provided either

$$n_2 = \sqrt{n_1 \cdot n_3} \qquad \ldots.(3.13)$$

and

$$d = \frac{\lambda \cdot (2I+1)}{4.(n_2^2 - \mathrm{Sin}^2(i))^{\frac{1}{2}}} \qquad \ldots.(3.14)$$

or

$$n_1 = n_3 \qquad \ldots.(3.15)$$

and

$$d = \frac{\lambda \cdot I}{2.(n_2^2 - \mathrm{Sin}^2(i))^{\frac{1}{2}}} \qquad \ldots.(3.16)$$

where I is an arbitrary integer.

The surface reflections of a lens may therefore be, in principle, reduced to zero at a specified wavelength by coating the lens with a layer of the appropriate thickness and refractive index.

In the case of an HDPE lens for use at a wavelength of about 1.2 mm we would require a material possessing a negligible absorption coefficient and a refractive index of 1.237 which could be coated onto the polyethylene in a layer approximately 0.24 mm thick. However, rather than spend time and effort searching for a suitable material and devising a way to coat it onto the HDPE it was decided to consider an alternative method

which offered more immediate promise of producing a reflection-cancelling region.

Jones and Cohn(ibid)discuss the reduction in surface reflections that may be produced by either embedding a reflective layer within the lens material or by machining a regular array of grooves onto the lens surface. D.G.Bodnar and H.L.Basset(Proc. I.E.E.E. AP-23 841 (1975))also consider the effects of grooves upon the surface reflectivity.

Of these two methods the technique of grooving the lens surface is most simple to apply to Polyethylene and it was adopted for the lenses produced as a result of the work described in this thesis. This technique is commonly referred to as 'blazing' the lens.

In order to experimentally examine the effect upon the surface reflectivity of blazing,three test plates were made from sheets of HDPE Rigidex-9. The first two were made from a single sample which was machined into a plane parallel sheet 3.15mm thick. This sample was then divided into two 80 x 80 mm squares, one of which was placed in a lathe and its major faces blazed with a concentric circular pattern of grooves whose contours are as shown in Fig 31c with a characteristic free space wavelength, λ, of 1.28 mm(this corresponds to a frequency of approximately 230 GHz).

A final test piece was then made, 80 x 80 mm square and 2.65 mm thick - i.e., approximately 3.15 - 2x0.26 mm thick.

The performance of each plate was examined at 95 and 190 GHz using an Impatt source and a Golay detector. The results of these tests are shown in Table 3.4.3. The transmission measurements were carried out in a similar manner to those conducted on the polarisers as discussed earlier in this thesis but with the plates angled at 20° to the beam direction to avoid standing

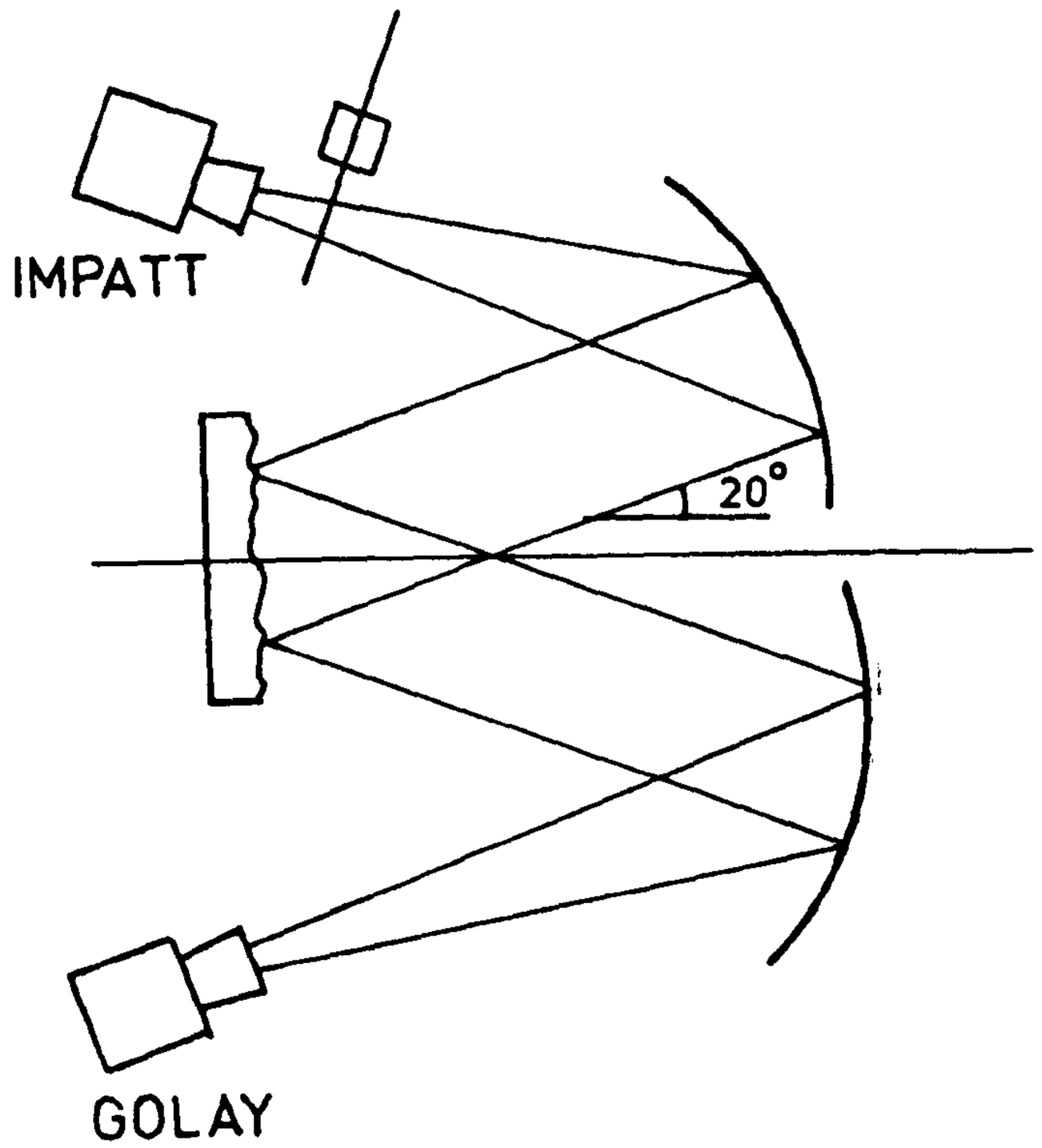

Fig. 32.
Test plate measurement system.

waves. The reflection measurements were carried out as indicated in Fig 32 with a beam whose 1/e power radius was about 10 mm and whose electric vector was perpendicular to the plane of reflection.

Table 3.4.3. Blazed Plate Tests

	Transmission 190 GHz	Reflection 190 GHz	Reflection 95 GHz
3.15 mm Plane	- 0.45 db	- 14.0 db	-10.0 db
2.65 mm Plane	- 0.44 db	- 14.0 db	- 16.0 db
3.15 mm Blazed	- 0.09 db	- 19.5 db	- 11.0 db
Estimated Error (from noise level)	± 0.1 db	± 3.0 db	± 0.5 db

The reflectivities quoted in Table 3.4.3 are referenced to the signal detected when a polished metal mirror replaced the HDPE test plates. In passing through the HDPE test plates we may expect less than 0.1 db of the radiation to be lost by absorption, it is, however, probable that most of the measured transmission loss for the blazed plate is due to absorption rather than reflection.

Unfiltered, over 99% of the Impatt's output was at 95 GHz, but this power could be more than adequately supressed by replacing the low-frequency feed horn with another designed for use in the 170 - 220 GHz band as the waveguide attached to this horn strongly rejected the fundamental oscillation.

Unfortunately, the remaining radiation did not consist solely of a single component at the harmonic frequency of 190 GHz but was contaminated by two anharmonic components.

The frequency of the fundamental oscillation could be

measured to an accuracy of ± 0.02 GHz by the use of a wavemeter and hence the frequency of the second harmonic was well known. The frequencies of the anharmonic components were measured with considerably less accuracy(± 5.0 GHz)using an Ebert Grating(descibed in a Thesis by P.H.Knapp, University of London, 1965)and a Fabry Perot resonator made from two inductive meshes. The measured frequencies of the anharmonic components were 205 and 240 GHz and the measured power ration of the 190:205;240 GHz components was 5:1:2(all ± 0.5 units). This uncertainty makes it difficult to compare the high-frequency reflectivity measured with that which may be predicted on the basis of the expressions quoted earlier in this section. Reflection measurements were therefore also made with the Impatt unfiltered. This provides an essentially pure source(to the -20 db level)and also greatly increases the available signal power, improving the accuracy with which measurements could be made.

For a frequency of 95 GHz and 20° angle of incidence equations 3.6 to 3.11 predict a reflected power level of -8.4 db from the 3.15 mm plate and -14.8 db from the 2.65 mm one. These figures are respectively 1.6 db and 1.2 db greater than those measured and hence it is possible that there is a systematic error of about 1.4 db in the measured results. Irrespective of this, however, the blazed plate displays a lower reflectivity and a higher transmissivity than either of the plane plates when examined with the composite high-frequency signal.

When performing the transmission measurements a pair of wire-grid polarisers were used to search for any cross-polarisation generated by the circular symmetry of the plazed pattern. No such effect was detected above the measuring system's -24 db noise floor and it was concluded that this was not a significant

problem.

From the results given above it was concluded that blazing the lens surfaces could be expected to produce a small but useful improvement in the lens transmission over a reasonable spectral range centred upon the free space wavelength for which the blazing is cut.

In practice two complete sets of lenses were manufactured, one blazed for a free space wavelength of 1.2 mm, the other unblazed. This was for two reasons: i) in this way it could be established that the blazed surfaces did not degrade the system performance in any way; ii) the unblazed lenses could be used for radiation wavelengths where the chosen blazing might be expected to increase the surface reflectivity.

Each of the lenses produced as a result of the work described in this thesis is of a plano-convex form. The method by which they were designed may be illustrated by reference to Fig 33a. Here the lens profile is represented by a variable, t, which is a function of the distance, h, from the lens axis and the focal length, f, of the curved surface.

In terms of simple geometric ray optics the focal length of such a surface is such that

$$t = \frac{f(1 - \mathrm{Cos}(\theta))}{u.\mathrm{Cos}(\theta) - 1} \qquad \ldots.(3.17)$$

(see, for example, Cornbleet,S., Microwave Optics, Academic Press, London 1976)where θ is as shown in Fig 33a, and $u = n_2/n_1$.

Such a lens will ideally couple two beams whose phasefront radii of curvature are R_1 and R_2 at the lens surface, where

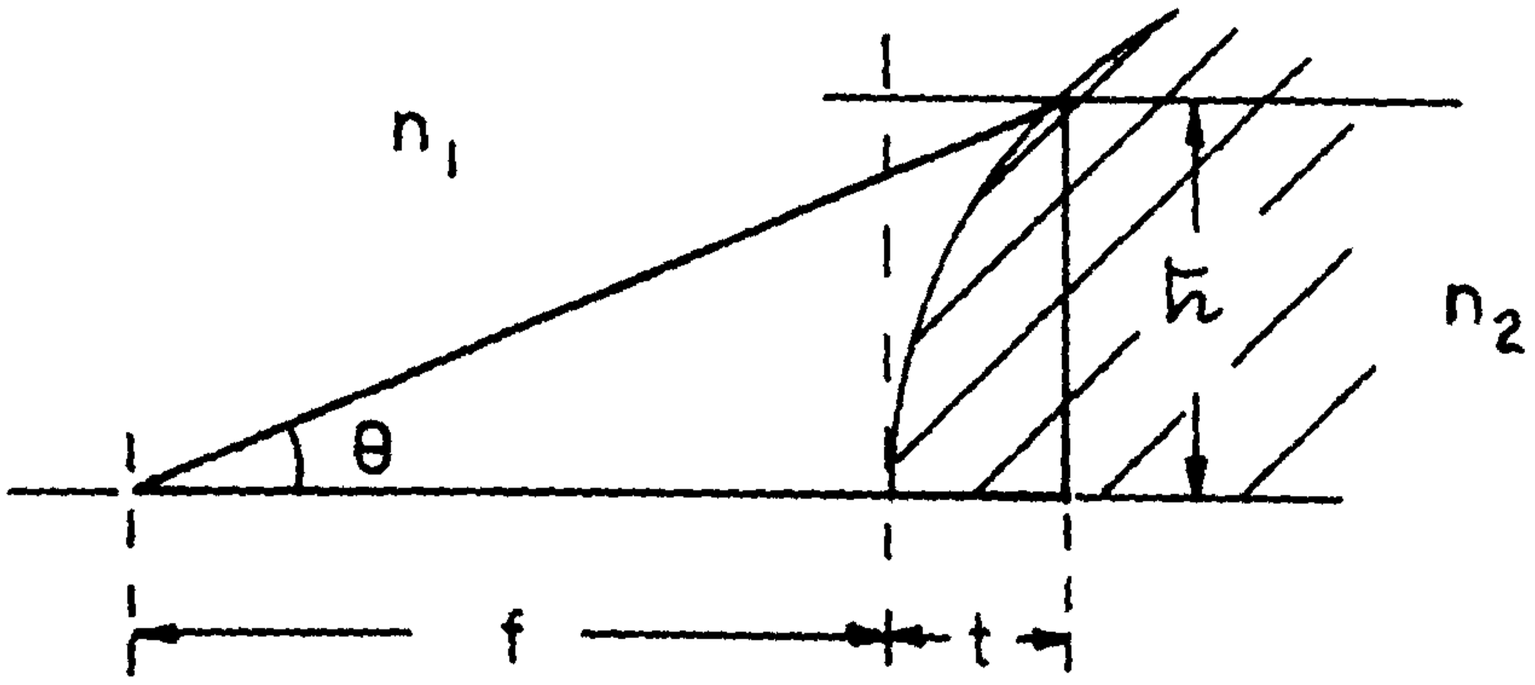

Fig. 33a.
Single sided geometric ray lens.

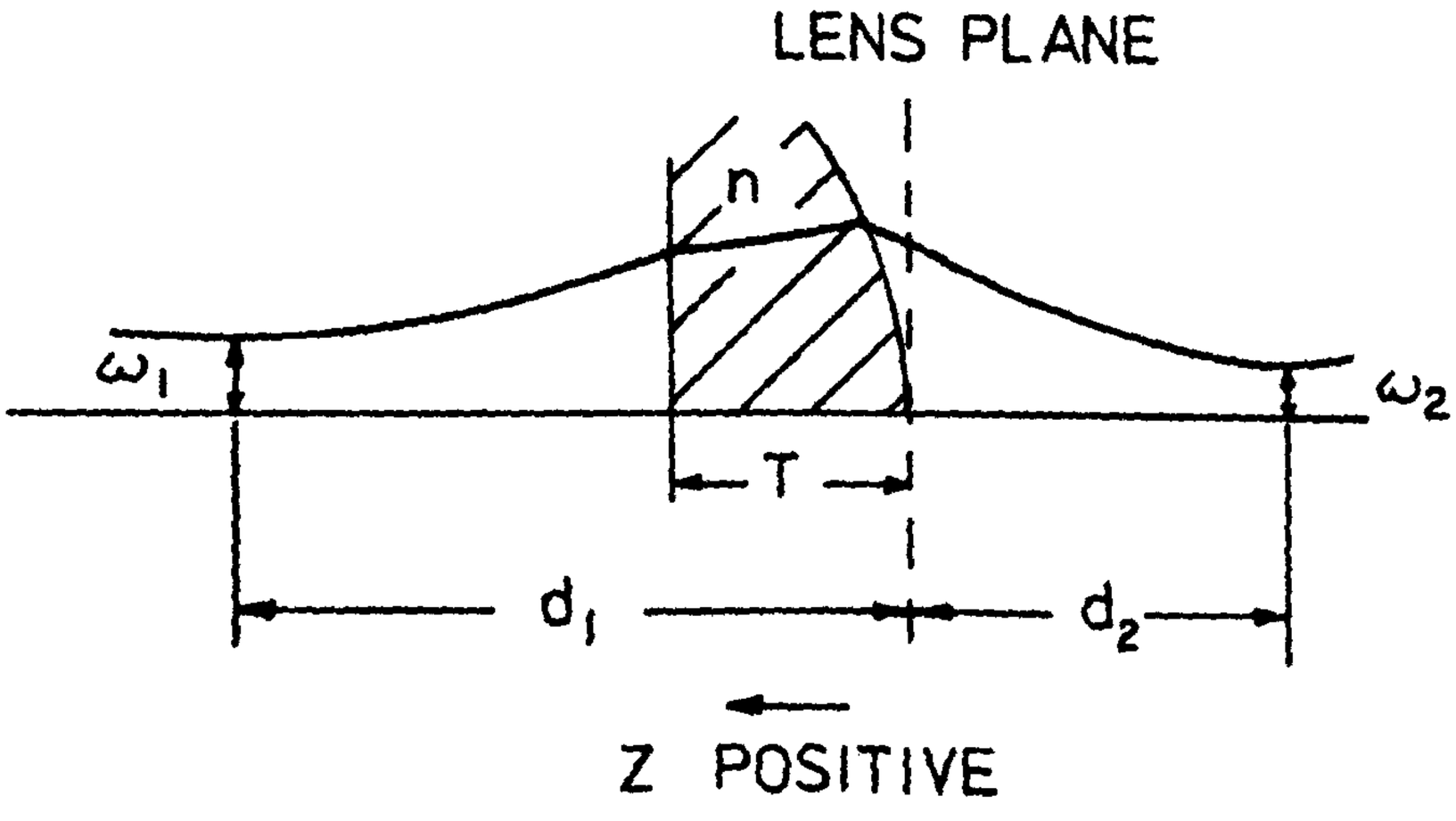

Fig. 33b.
Double sided Gaussian ray lens.

$$1/R_2 = 1/R_1 - 1/f \qquad \ldots.(3.18)$$

provided that t is very much smaller than either R_1 or R_2 at every point on the lens surface, and the beam sizes are equal at the lens plane(defined by t = 0).

Now, from Fig 33a we may write

$$\mathrm{Cos}(\theta) = \left(1 + h^2/(f+t)^2\right)^{-\frac{1}{2}} \qquad \ldots.(3.19)$$

and, by combining this with expression 3.17 we may obtain

$$0 = t^2(u^2-1) + 2tf(u-1) - h^2 \qquad \ldots.(3.20)$$

As we require that t = 0 when h = 0 we may therefore write

$$t = \frac{\left|(f^2(u-1)^2 - (u^2-1)h^2)^{\frac{1}{2}}\right| - f(u-1)}{(u^2-1)} \qquad \ldots.(3.21)$$

Now in general the plane face of a plano-convex lens will also act upon the beam, changing the radius of curvature of its phasefront as illustrated in Fig 33b.

Consider a ray which passes through the waist plane at a distance from the beam axis equal to the waist radius, w_1, and which is everywhere perpendicular to the local phasefront. The seperation between such a ray and the beam axis will be equal to the beam radius, w, and may be obtained from the expression

$$w^2 = w_1^2 + \frac{z^2\lambda^2}{\pi^2 w_1^2} \qquad \ldots.(3.22)$$

From this it follows that

$$w \frac{dw}{dZ} = \frac{Z\lambda^2}{\pi^2 w_1^2} \quad \ldots.(3.23)$$

which, by reference to Kogelnik and Li(ibid)may be re-written as

$$\frac{dw}{dZ} = \frac{w}{R} \quad \ldots.(3.24)$$

Now the angle of incidence of this ray upon the plane interface, i, is such that

$$i = \arctan\left[\left.\frac{dw}{dZ}\right|_{Z=(T-d_1)}\right] \quad \ldots.(3.25)$$

i.e.

$$i = \arctan\left[\frac{w(T-d_1)}{R(T-d_1)}\right] \quad \ldots.(3.26)$$

we may also write a similar expression for the refracted ray

$$r = \arctan\left[\frac{w}{R'}\right] \quad \ldots.(3.27)$$

where r is the angle of refraction, $w = w(T-d_1)$, and R' is the phasefront radius of curvature at the plane interface of the gaussian beam containing the refracted ray.

By the application of Snell's law

$$\mathrm{Sin}\left(\arctan\left[\frac{w}{R}\right]\right) = u.\mathrm{Sin}\left(\arctan\left[\frac{w}{R'}\right]\right) \quad \ldots.(3.28)$$

at the interface, which, for a paraxial beam may be satisfactorily approximated by

$$\frac{w}{R} = u.\frac{w}{R}, \qquad \ldots.(3.29)$$

hence

$$R' = u.R \qquad \ldots.(3.30)$$

From the above argument it may be seen that the effect of the plane face is to increase the beam's radius of curvature by the factor u at the face plane. Given the new value, R', and knowing w the refracted beam can be uniquely defined and it's size and radius of curvature at the lenses curved face may be obtained. In practice, for a thin lens, the values u.R and w may be used as the beam will change very little in passing through the lens.

A computer program was written to perform the necessary calculations and write out the surface profile as an array of values. The program required w_1, d_1, and T values in order to determine the effective values of w and R_1 at the lens plane. It then calculated the appropriate values of f and d_2 that would enable the lens to couple this beam into another defined in terms of its 1/e - power angle. As written the program assumed a refractive index u = 1.53, a radiation wavelength of 1.2 mm, and that it is the beam (w_1, R_1)that enters the lens via its plane face.

Table 3.5.1 illustrates the results obtained from this program for the UKIRT Diplexer. This was designed on the basis of an internal beam-waist w = 14.2 mm located midway between the mixer and local oscillator port lenses. The lens L1 is designed to couple the Diplexer to the mixer and local oscillator feed horns. L2 is designed to couple the Diplexer to the telescope optics with an underillumination factor of 1.5.

Table 3.5.1. UKIRT Lens Data

Lens	w_1	d_1	T	θ_e (RAD)	w	d_2	f
L1	14.2	251	15	-0.103	15.6	-100	98.0
L2	14.2	236	10	-0.037	15.5	-262	294.0

(All the linear dimensions in the above table are in mm. Negative values imply a beam-waist location on the side of the lens closest to the curved face.)

From the measurements described earlier in this section we may predict that, if blazed satisfactorily, the combined losses due to beam trunkation, reflection, and absorption at a frequency of 250 GHz will be -0.25 ± 0.1 db at each of the above lenses.

The performance of the lenses was examined as a part of the program of measurements made upon the assembled Diplexers and hence will be discussed in section 3.6.

3.5. Construction and Performance of Feed Horns.

The feed horns employed to couple the waveguide mixer and harmonic multiplier were designed with the assistance of a numerical routine published by Loefer, et al(Microwaves 15(5) 58 (1976)). The geometry chosen was of a conical form with an aperture radius of 5.2 mm and a cone half-angle of 12°. The theoretical behaviour of such a horn has been discussed in section 2.5 and will not be considered further here.

The dimensions quoted were chosen as horns of this size and shape had been sucessfully used as a part of a number of previous recievers and were known to produce an essentially paraxial beam approaching a circularly symmetric Gaussian form.

Both corrugated and smooth-walled feed horns were manufactured for use in the prototype Diplexer system. The corrugated horns were made by electroplating copper onto an aluminium mandril which was then dissolved away. Since the corrugated mandrils demand a considerable amount of time and effort on the part of the machinist this is a wasteful process as each mandril must be destroyed in order to free the copper horn. Smooth-walled horns, however, may be grown on to a stainless steel mandril from which the horn may be pulled free. This is a much more efficient process as the mandril can be made more easily than the corrugated form and, with care, may be used to grow a number of identical feed horns.

In practice the only difference in behaviour between the two types of horn that could be seen above experimental error limits was in the radiated beam angle. It was discovered that the smooth-walled horns radiated power into a main lobe with a slightly smaller beam angle than that produced by the corrugated

horn. This difference was, however, so small that the two types of horn could be interchanged on the prototype Diplexer without a measureable effect upon its performance. On the basis of the obtained results it was decided to use smooth-walled horns on the UKIRT Diplexer system.

Figure 34 shows the far field pattern of one of the smooth-walled horns used on the prototype and UKIRT Diplexers. The best-fit Gaussian to the patterns radiated by these horns was for a 1/e - power half-angle of 0.103 $\pm$ 0.003 Radians at a frequency of 230 GHz. The measured patterns were obtained by attaching the horns to the output waveguide of a harmonic multiplier block mounted on a rotation table. A Golay detector placed approximately 2000 mm from the axis of rotation was then used to measure the power radiated as a function of the angle of rotation. The collecting area of the Golay system subtended an angle of 0.005 Radians as seen from the feed horn.

By using a wire grid polariser over the Golay detector it was established that the cross-polarisation component radiated by the feed horns was below the measurement system's -16 db noise floor.

The insertion loss and effective VSWR of the feed horns were determined as part of the tests performed upon the assembled Diplexers and, as such, will be discussed in the following section.

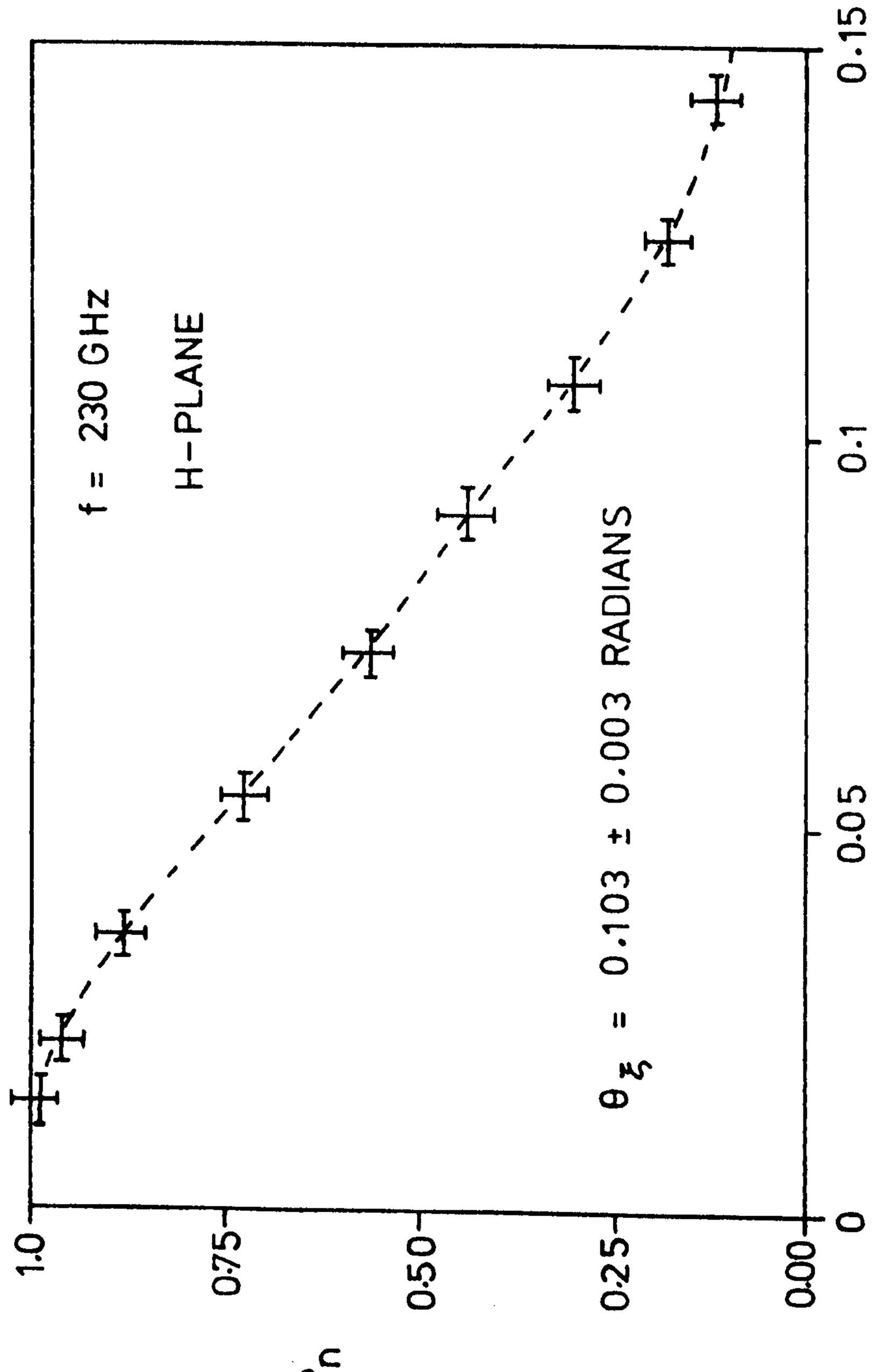

Fig. 34.
Typical measured feed horn pattern.

3.6 Laboratory tests upon the performance of the assembled Diplexers.

The first tests carried out upon the assembled Diplexers were to measure the efficiency with which power could be coupled through them. This was done with a waveguide radiometer system similar to that indicated in Figure 35a. Here the local oscillator power for the mixer is injected via the side-port of a -10 db waveguide coupler. The direct port of the waveguide coupler was then attached to the feed horn at one of the Diplexer's output ports.

By supplying the mixer with local oscillator power in this way we are able to place test loads of known temperature(Eccosorb sheet at either ambient or liquid Nitrogen temperature)at various points throughout the optics without preventing it from reaching the mixer. Hence we can examine the absorption and reflection losses in each optical element and of the system as a whole.

The side-port loss of the waveguide coupler was measured to be -9 $\pm$ 1 db at 230 GHz. Due to this loss the maximum available multiplier output power produced only about 150 microwatts at the mixer. This relatively low level produced a significant degradation in the mixer performance, but the radiometer still functioned well enough to make the make the measurements described here.

By comparing the signal from Eccosorb loads at various points throughout the system it was established that the absorptive and reflective losses in each lens was -0.25 $\pm$ 0.1 db and that the total loss of the lenses, polarisers, and roof-mirrors was -0.6 $\pm$ 0.1 db. Interchanging the blazed and unblazed lenses

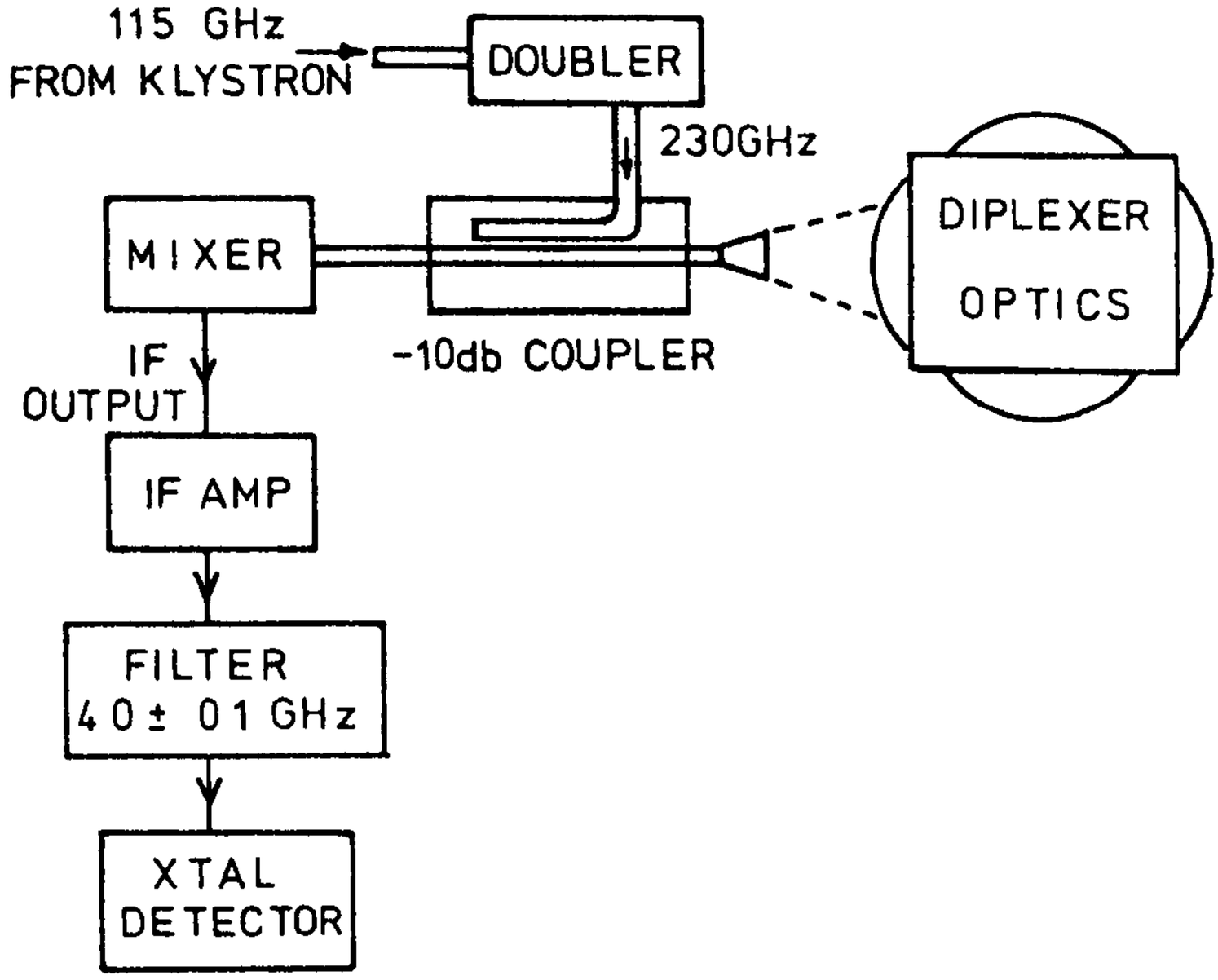

Fig. 35a.
Waveguide radiometer.

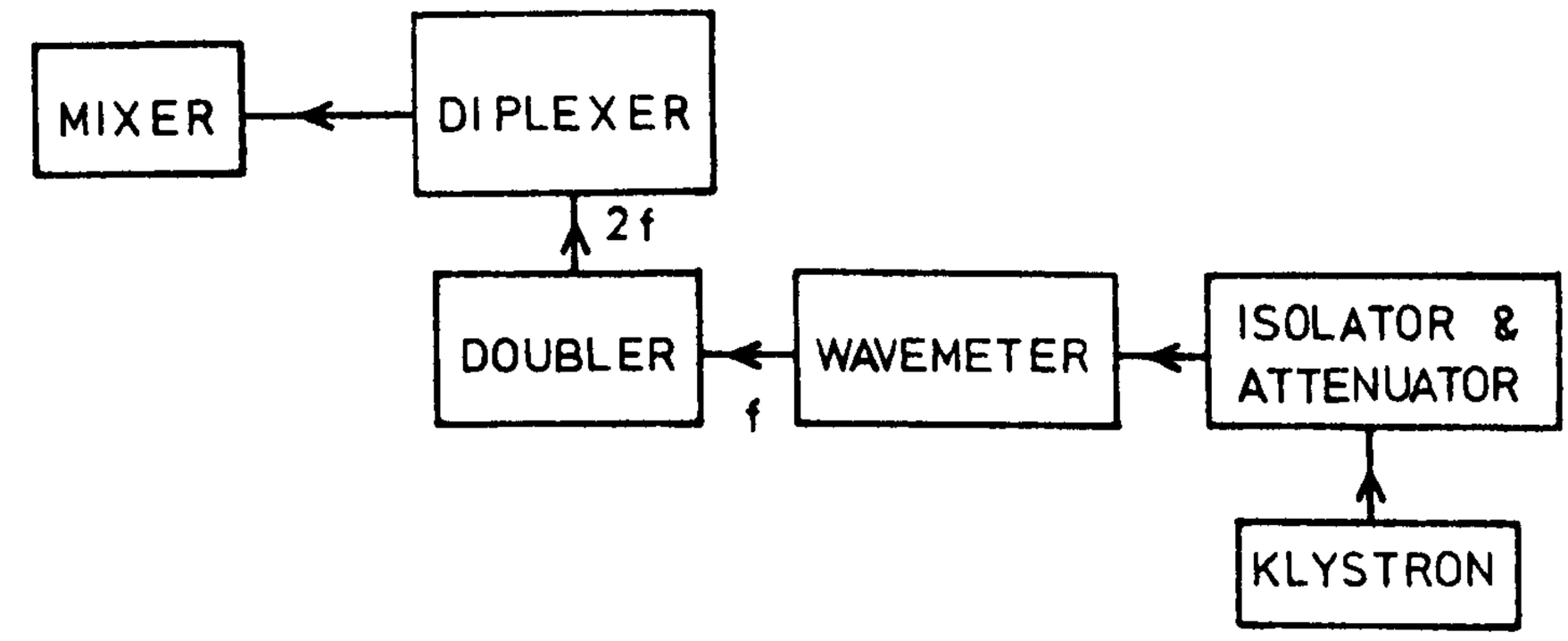

Fig. 35b.
Arrangement for frequency response measurements.

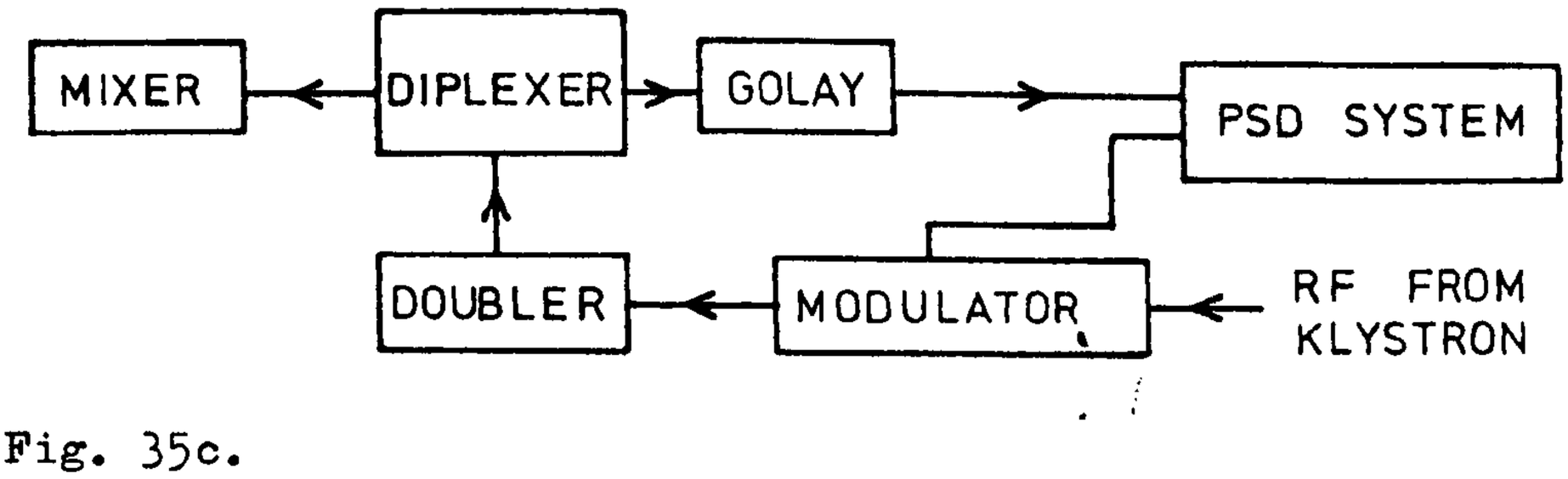

Fig. 35c.
Arrangement for reflection measurements.

produced no measureable alteration in the system losses(i.e. less than 0.1 db). All of the above figures were obtained at a local oscillator frequency of 230 GHz.

The next set of tests performed were designed to measure the frequency response and the efficiency with which a Gaussian beam could be coupled through the Diplexer. The arrangement for these tests was as indicated in Figure 35b.

The klystron frequency was measured with a wavemeter and the power transmission of the Diplexer was normalised at each frequency by comparison with the power level observed when either of the roof-mirrors was blocked off with Eccosorb.

From Born and Wolf(ibid), page 259,

$$P = P_1 + P_2 + 2(P_1.P_2)^{\frac{1}{2}}.\mathrm{Cos}(d) \qquad \ldots.(3.31)$$

where P_1 and P_2 are the power levels observed if one or the other of the roof-mirrors is blocked off and P is the total power observed when summing the contributions of both beams with a relative phase shift, d. The normalised power output, P_n , may therefore be obtained from.

$$P_n = P/(2(P_1 + P_2)) \qquad \ldots.(3.32)$$

Figure 36 shows the measured frequency response of the prototype Diplexer for one input/output port pair with the movable mirror set to the centre of its range of adjustment ($\pm$ 8.0 mm). The klystron employed for these measurements could be made to oscillate in a high-power mode only up to 116 GHz. Above this frequency a low-power mode had to be used, hence the power measurements made in the 232 - 238 GHz region are

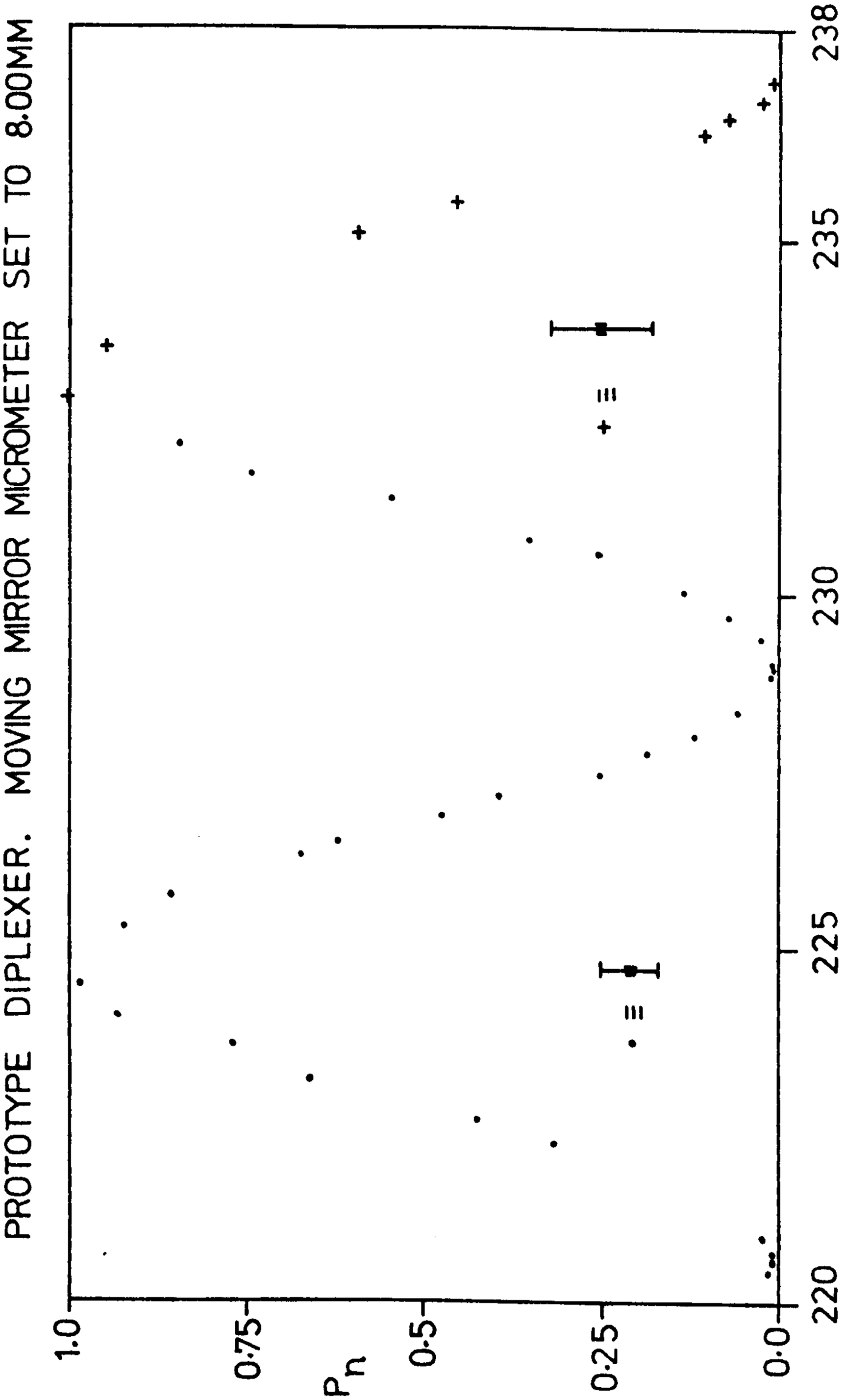

Fig. 36.
Typical Diplexer frequency response.

less accurate than those covering the 200-232 GHz range.

As may be seen from this illustration the frequency response is essentially sinusoidal with a period of 8.2 ± 0.1 GHz. This corresponds to an optimum intermediate frequency of 4.1 GHz and a path difference of 36.5 mm. The ± 8 mm range of mirror movement therefore enables the selection of any optimum intermediate frequency in the range 7.3 to 2.85 GHz. The results shown are for a port pair that would be efficiently coupled at a zero path difference. The behaviour of each port pair was examined, both as a function of frequency and of the position of the adjustable mirror, and each of the Diplexers were found to behave as would be expected on the basis of the theoretical analysis described earlier in this thesis.

In order to assess the losses produced by the feed horns the mixer bias current generated by a given doubler was compared with that generated when the mixer and doubler were directly coupled waveguide-to-waveguide. From this comparison it was estimated that the total loss between the waveguide flanges was -1.7 ± 0.2 db. Allowing for the losses in the rest of the system this implies that each feed horn loses -0.6 ± 0.2 db.

The beams within the Diplexer were determined to be correctly polarised and could be shown to be quasi-parallel as the same signal level was produced by blocking off either of the roof-mirrors. The measured loss is therefore most probably due to reflection or absorption effects at the feed horns.

In was observed on a number of occasions that by moving the mixer/feed horn assemblies a small amount along the beam axis it was possible to modulate the power coupled into the mixer diode. The amount of this modulation was found to depend upon the choice of mixer block and the worst apparent VSWR observed was 1.25:1 .

It was, however, observed that the doubler bias current also varied as the horn-to-horn distance was changed. Since this implies that the power output of the doubler may also may be changing it is not possible to infer a specific value for the reflectivity from the measured VSWR. This variation in the doubler bias current does, however, serve to imply that the two diodes are well coupled by the Diplexer optics as - if the coupling losses were high - it would not be possible to return enough power from the mixer to affect the doubler's bias conditions.

Now the local oscillator power delivered to the mixer may be peaked by adjusting the mixer/feed horn position, but any reflections directed to the telescope port may lead to standing waves which degrade the system's spectral response. A number of tests were therefore undertaken in order to assess the reflectivity of the mixer, its feed horn, and of the Diplexer as a whole. Measurements were made by coupling a Golay detector to the telescope port, modulating the local oscillator as shown in Figure 35c, and observing the power that emerged under various conditions. The depth of modulation was kept sufficiently small (less than 0.5db)that the mixer's match was not affected by the change in the incident power level.

The unused output port was terminated with a sheet of Eccosorb at ambient temperature, and a flat, polished metal plate was placed over the mixer lens so as to reflect the local oscillator power back into the system before it could reach the lens. The moving mirror position was then adjusted to maximise the signal seen by the Golay detector. Under these conditions the Diplexer acts as a bidirectional -3 db coupler, and the observed signal may be used as a reference level for subsequent reflectivity measurements.

The metal plate was then removed and it was found that the mixer current did indeed indicate that the available local oscillator power at the diode had fallen by 3 db.

Under these conditions, and with the mixer's back-plunger adjusted for the maximum mixer bias current, the observed reflected signal was - 13.5 db below that seen with the metal mirror in place. When the mixer's feed horn was covered with a sheet of Eccosorb the observed signal fell to -21.2 db.

The moving mirror was then readjusted to maximize the mixer bias current, hence returning the Diplexer to its normal mode of operation. The signal level at the telescope port was then re-measured with Eccosorb over the mixer feed horn and was found to be unchanged. From this it may be inferred that the Diplexer directed no more than -24 db of the input local oscillator power to either of its input ports irrespective of its tuning.

With the Diplexer adjusted for normal operation the power reflected by the mixer and its feed-horn could not be seen at the telescope port above that reflected by the Diplexer itself but the data from which the illustrated frequency response was drawn indicates a maximum interport rejection figure of -23 $\pm$ 2 db. This value is similar to that obtained for the amount of local oscillator power reflected by the Diplexer into the telescope port. This similarity could be a consequence of both effects being produced by the same, small misalignment within the interferometer system.

The above results were obtained using the Prototype Diplexer at 230 GHz and are typically accurate to $\pm$ 1.0 db. Tests performed on the UKIRT Diplexer revealed a similar performance but with a slightly lower interport leakage figure of -29.0 $\pm$ 2.0 db.

In order to try and establish whether the observed mixer-port

reflection was due to the feed horn or not, the reflectivity of the mixer used in the above tests was examined via a waveguide -10 db coupler in place of the Diplexer. The reflectivities measured in this way varied over the range -4.0 to -6.0 db (depending upon the position of the mixer's back plunger)which is clearly much higher than measured via the Diplexer. It is therefore possible that the -10 db coupler is not itself well matched to the mixer waveguide and hence the above figures do not necessarily represent the inherent reflectivity of the mixer when coupled via the feed horns.

Over a period of time four different mixers and feed horns were tried on the two Diplexer systems and it was found that the apparent local oscillator VSWR depended rather more on the choice of mixer than the choice of feed horn, but it would not be possible on the basis of these observations to make a reliable estimate of the reflectivities of either the mixers or feed horns.

It was realised during the course of the above measurements that the amount of power reflected by a given mixer/feed horn combination could, in principle, be reduced by the application of destructive interference in much the same way as was the case for dielectric lenses. Some experiments were therefore carried out by stretching thin sheets of Mylar over open spacer rings placed in front of the feed horn aperture and observing the resultant change in the apparent VSWR and peak mixer current.

The mixer used for the tests described above was not available when these experiments were undertaken and so a different, but similar, mixer was used.

The mixer/feed horn combination used for these experiments gave an apparent VSWR of 1.21 $\pm$ 0.02 when used with the UKIRT

Diplexer at a frequency of 226.2 ± 0.2 GHz. After some experimentation it was discovered that placing a Mylar sheet 0.25 ± 0.05 mm thick 1.65 ± 0.1 mm in front of the horn aperture it was possible to reduce the apparent VSWR to 1.08 ± 0.02 and increase the peak level local oscillator power at the mixer diode by 0.7 ± 0.1 db. The system noise temperature also fell, implying that the signal coupling from the telescope port had been increased by a similar amount.

Now the optimum reduction in the overall reflectivity will be produced when the reflections from the Mylar sheet and the mixer/feed horn assembly are arranged to be 180° out of phase and are of a similar magnitude. Hence we may expect that the reflectivity of the Mylar sheet and the mixer/feed horn assembly should be similar when the VSWR has been significantly reduced. Using the above thickness, and assuming that the refractive index of Mylar is 1.72(as given in Table 3.4.1), we can use expressions 3.9 to 3.12 to estimate that the reflectivity of the Mylar sheet was -9.5 ± 1.4 db.

From the experiments described above it was concluded that this technique could be used to improve the performance of a system where the mixer/feed horn assembly exhibited a significant reflectivity and it was therefore intended that a suitable matching sheet would be included within the final UKIRT system. However, the program of research and development carried out by D. Vizard at the Appleton Laboratory, Slough, led to a marked improvement in the performance of subsequent mixers. One of the results of this was that later mixers exhibited a much lower reflectivity than those used during the initial experiments, and by the time the final system was assemble in Hawaii the apparent VSWR was no more than 1.05. Hence in the

final receiver the Mylar matching sheet proved to be unnecessary and was therefore omitted.

The final series of laboratory tests carried out upon the UKIRT Diplexer system were to measure the beam pattern produced at the telescope port. This was done with the receiver arranged in its final configuration within the telescope mount. The source used in these tests was an expanded polystyrene bucket filled with a combination of liquid Nitrogen and Eccosorb sheet. Except for a window area 10 mm square the outside of the bucket was covered with an additional sheet of Eccosorb at ambient temperature. As the expanded polystyrene walls are reasonably transparent to radiation with a wavelength around one millimetre the bucket will appear as a cold load 10 mm square. By noting the level of signal detected as a function of the window position the telescope port beam pattern could be determined.

The beam pattern was measured twice, firstly in a plane 3000 mm from the telescope port lens, then in a plane 800 mm from the lens. In each case the beam was found to be directed along the correct axis to within the experimental error(0.004 mRadians)and to be circularly symmetric with an essentially fundamental Gaussian form. By the use of a set of computer routines which allow for the finite window size it was estimated that the observed beam best fitted a beam whose 1/e amplitude radius, w, was 160 $\pm$ 20 mm in the far plane and 31 $\pm$ 1.5 mm in the near plane.

Now the telescope lens was designed to produce a beam whose waist is 260 mm from the lens plane and has a radius of 7.4 mm. Hence we can predict that the beam sizes in the far and near planes should be 154 mm and 31.2 mm respectively. The measured and predicted beam sizes are therefore in satisfactory agreement.

4. System Calibration and Performance on UKIRT

The receiver, of which the Quasi-Optical system described in this thesis is a part, was tested, calibrated, and commissioned on UKIRT during the last two weeks of June 1980. The system noise temperature on UKIRT was measured at the telescope port of the Diplexer to be 3800 $\pm$ 200 ^{o}K(single sideband)over the 230-250 GHz range.

The optical performance of the whole system including the telescope was determined by observations of the atmosphere and the planet Jupiter. At least once every night during the commissioning period the apparent sky temperature was measured as a function of the zenith angle. These measurements were calibrated against the emission from two Eccosorb loads, one at ambient temperature, the other immersed in boiling liquid Nitrogen.

As the Mauna Kea Observatory is at an altitude of 14,000 ft the boiling point of Nitrogen will be slightly different from that measured at sea level. At the Observatory altitude the atmospheric pressure is approximately 600 mb and the Boiling Temperature of liquid Nitrogen it, therefore, 73.3 ^{o}K rather than 77.35 ^{o}K as at sea level.

If it is assumed that the atmosphere above the observing site is homogeneous, has a physical temperature T_{sky}, and that the optical depth when looking to the zenith is D, then the apparent emission temperature, T, when observing the sky at an angle, z, from the zenith direction is given by the expression

$$T = T_{sky}.(1 - \exp(-D.\mathrm{Sec}(z))) \qquad \ldots.(4.1)$$

In practice a real receiver/telescope system may be expected to see some radiation from its local surroundings due to emission, scattering, and other effects within the system. To allow for this we may write that the observed apparent sky temperature, T_z, is defined as

$$T_z = C.T_e + (1-C).T_{sky}.(1 - \exp(-D.\mathrm{Sec}(z))) \quad \ldots.(4.2)$$

where C represents the fractional sensitivity of the receiver to radiation from the local surroundings whose temperature are T_e.

Now, provided D.Sec(z) is quite small compared with unity, then 4.2 may be approximated by

$$T_z = C.T_e + (1-C).T_{sky}.D.\mathrm{Sec}(z) \quad \ldots.(4.3)$$

hence C and D may both be inferred from the variation of T_z with Sec(z) provided T_e and T_{sky} are both known.

T_e is simply the ambient temperature inside the dome, and during the observations discussed in this section T_e was measured to be 277 $\pm$ 2 ^{o}K.

In the absence of any direct method of measuring T_{sky} it becomes necessary to choose a suitable value by assumption from either indirect measurement or by argument. At 230 GHz the dominant source of atmospheric emission is water vapour. As this will tend to crystallize out at temperatures below 273 ^{o}K we might expect than $T_{sky} \gtrsim 273\ ^{o}$K. It must be expected that there will be both water vapour and small ice crystals in the upper air that will continue to emit and absorb radiation below this temperature, but it will here be assumed that the majority

of the observed emission comes from water vapour which is not supercooled. If it is also accepted that the atmosphere immediately above the observing site will, in general, be no warmer than the air temperature measured at ground level we may estimate that $277\ ^{o}K > T_{sky} \gtrsim 273\ ^{o}K$. Hence for the purposes of subsequent calculations the value $T_{sky} = 273\ ^{o}K$ has been adopted as a satisfactory estimate.

Table 4.1 Results of Sky-Dip Observations.

DATE	$C.T_e(^{o}K)$	$(1-C).D.T_{sky}(^{o}K)$	C	D	$T_v(^{o}K)$
23rd	58.8	23.7	0.21	0.11	30.0
24th	51.9	33.5	0.19	0.15	41.3
* 24th	66.8	29.9	0.24	0.14	39.4
* 24th	48.1	36.5	0.17	0.16	44.0
25th	56.2	27.1	0.20	0.12	33.9
26th	68.9	27.4	0.25	0.13	36.6
27th	71.2	23.2	0.26	0.12	31.4
28th	65.7	17.1	0.24	0.08	22.4
29th	78.3	30.2	0.28	0.15	42.0
30th	72.3	33.8	0.26	0.17	45.7
+ 30th	73.5	32.4	0.26	0.16	43.8

(* These measurements at intervals of approximately 2 hrs.)

(+ This observation was made to the West within half an hour of the previous measurement. All other measurements were made by dipping South.)

If, as is possible, T_{sky} was lower than assumed then the actual optical depth of the sky will be reater than calculated. This in turn leads to the temperatures calculated for any astronomical source being smaller than the actual value as insufficient allowance will be made for atmospheric absorption.

The sky-dip data collected during the period of observation is summarised in Table 4.1. Except where otherwise stated each

of the sky-dips shown was taken approximately one hour after Sunset, just prior to the planetary observations discussed later in this section, and each was completed in a period of less than 15 minutes. The tabulated results were obtained by a linear regression to an expression of the form $y = mx + k$ where $y = T_z$, $m = (1-C).D.T_{sky}$, $x = Sec(z)$, and $k = C.T_e$, assuming that $T_e = 277\ ^oK$, and $T_{sky} = 273\ ^oK$. Each of the observed points is within $2\ ^oK$ of the best-fit line. T_v is the apparent sky temperature that would be seen when looking to the zenith if C were zero. i.e.

$$T_v = D.T_{sky} = m.(1 - k/T_e)^{-1} \qquad ....(4.4)$$

From the tabluated figures it may be seen that during the observing period the mean value of $C = 0.23 \pm 0.05$ and $T_v = 37 \pm 7\ ^oK$.

The next measurements to be made were of the antenna pattern. Figure 37 illustrates the signal power recorded as a function of the Right Ascension and Declination offset angle between the beam axis and the centre of Jupiter's disc. The best-fit Gaussian to the observed pattern has a 1/e - power half-angle of 46.6 "arc with a statistical uncertainty of $\pm$ 1 "arc. The positional errors on the Right Ascension offset points are approximately $2\frac{1}{2}$ times greater than the Declination offset ones due to the movement of Jupiter across the celestial sphere. At the time of observation Jupiter was moving 21 "arc in Right Ascension and $8\frac{1}{2}$ "arc in Declination every hour. The pattern sidelobes were not detected above the measurement noise floor and hence must be at least -14 db below the signal sensitivity at the beam axis.

If the angular semi-diameter of Jupiter was very small

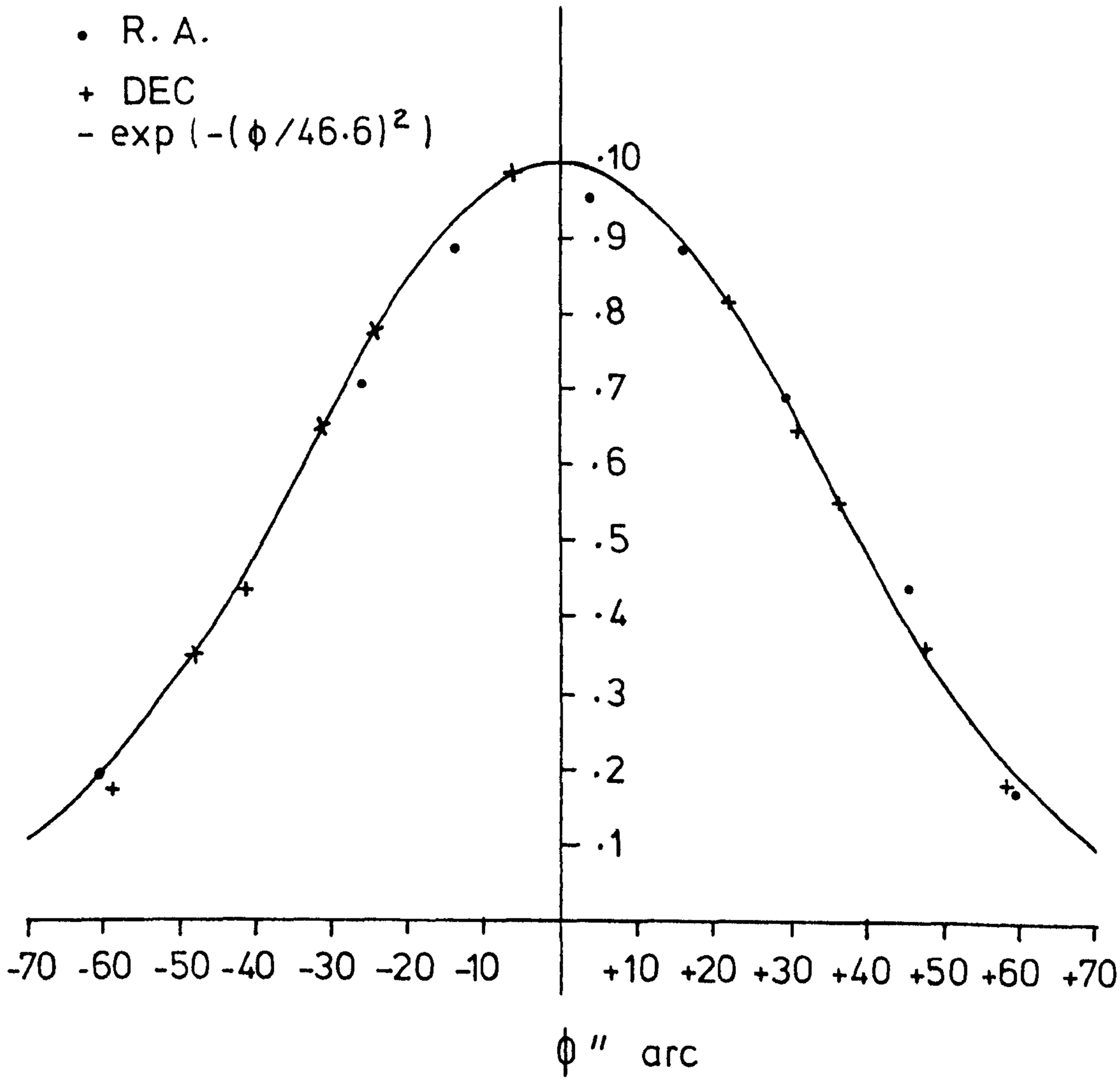

Fig. 37.
Measured telescope pattern.

compared with the beam-size then Figure 37 could be regarded as the point-source antenna pattern. However, over the period of observation the semi-diameter of Jupiter was approximately 16 "arc which is only about one-third of the observed beam-size. It is therefore necessary to estimate what effect this finite source extent has upon the measured beam pattern.

The manner in which this was done may be illustrated by reference to Figure 38. This represents a disc of uniform brightness whose radius is, a, and whose centre is a distance, d, from the axis of a circularly symmetric Gaussian beam whose 1/e - power radius is, b.

The incremental power coupled from a strip, δc, as illustrated, is proportional to

$$\exp(-(c/b)^2).(\mathrm{Erf}((d+e)/b) - \mathrm{Erf}((d-e)/b)) \quad ....(4.5)$$

where

$$e = (a^2 - c^2)^{\frac{1}{2}} \quad ....(4.6)$$

and Erf represents the Error Function.

The relative power coupling for given values of a, b, and d, may therefore be obtained by summing this expression over the range $-c < a < c$.

At a wavelength of 1.32 mm, and with an underillumination ratio of u = 1.5, the UKIRT main lobe should best fit a Gaussian whose 1/e - power half-angle is 44.5 "arc. Hence, if a = 16 "arc then we may anticipate that a/b should be approximately 0.35.

A computer program was written to calculate the apparent beam pattern as a function of a/b and it was found that, when $a/b \simeq 0.35$ the resultant pattern could be closely approximated by a Gaussian whose 1/e - power half-angle is 1.028*b. On

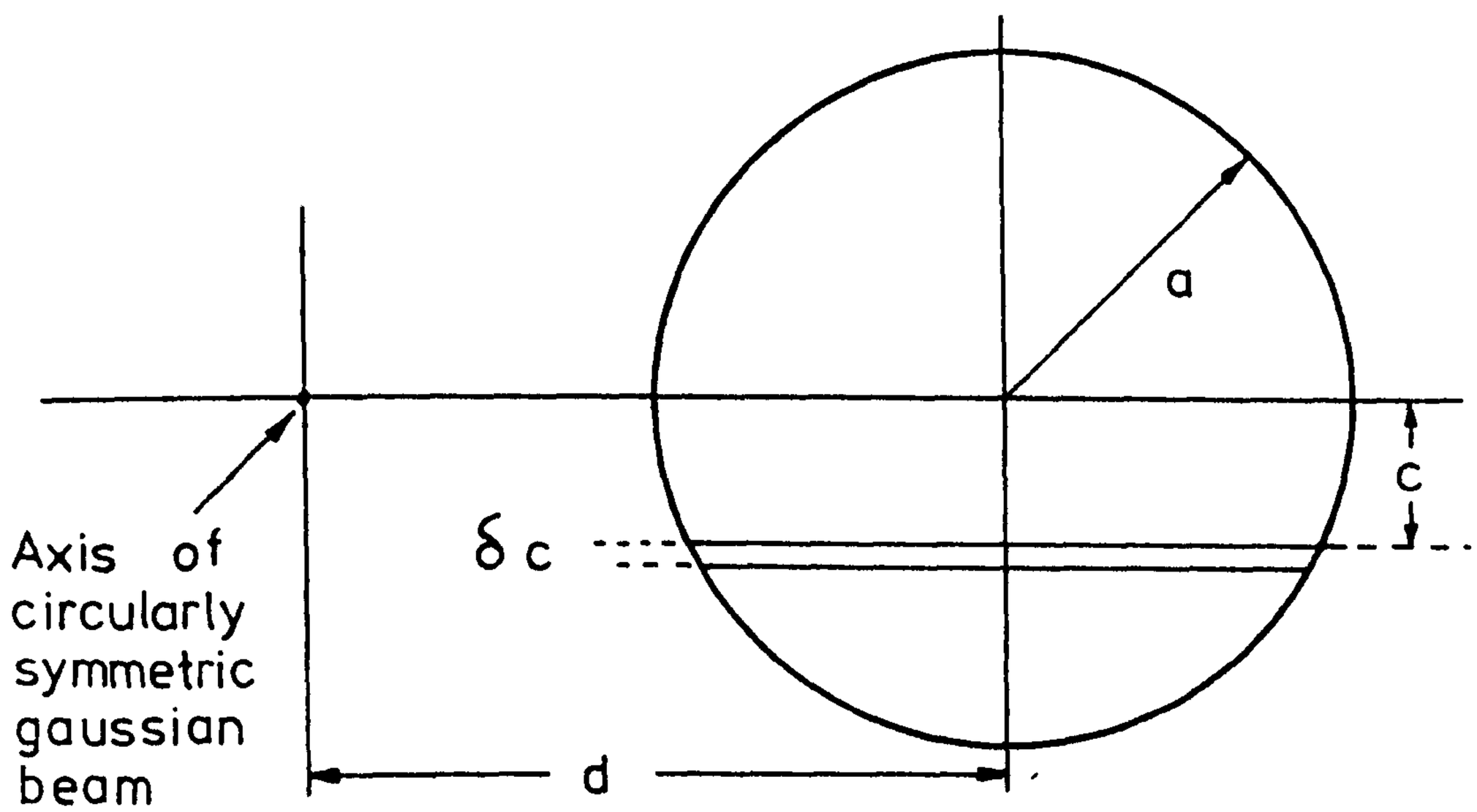

Fig. 38. DISC OF RADIUS a OFFSET A DISTANCE d FROM THE BEAM AXIS.

this basis the measured beam shape implies that the 1/e - power half-angle of the corresponding antenna pattern is 45.3 $\pm$ 1.0 "arc. Hence the measured and predicted antenna patterns are in agreement to within the experimental error of 2½%.

Having established that the Quasi-Optical system was effectively producing the desired antenna pattern it was then necessary to establish that power was being efficiently coupled between the antenna pattern and the receiver.

Consider once more the situation when observing the sky emission at a known zenith angle. We may expect that in such a case that all the radiation entering the receiver via the antenna pattern and the spillover around the secondary will come from a region of the sky not far from that covered by the main lobe. The signal contributed in this way may therefore be attributed to a single region of the sky whose brightness temperature is T.

Figure 39a represents the situation when such a measurement is being made. e_c is an efficiency figure which represents the fraction of the receiver beam that does not see the cassegrain centre stop. e_o is an efficiency figure which contains the losses due to absorption, scattering, and other losses within the optical system between the receiver calibration plane and the sky. It is assumed that both the centre stop and the optical system are at the common environmental temperature, T_e.

We may therefore write that the observed sky temperature, T_z, is such that

$$T_z = e_o.e_c.T + (1 - e_o.e_c).T_e \qquad \ldots.(4.7)$$

i.e.

$$C = 1 - e_o.e_c \qquad \ldots.(4.8)$$

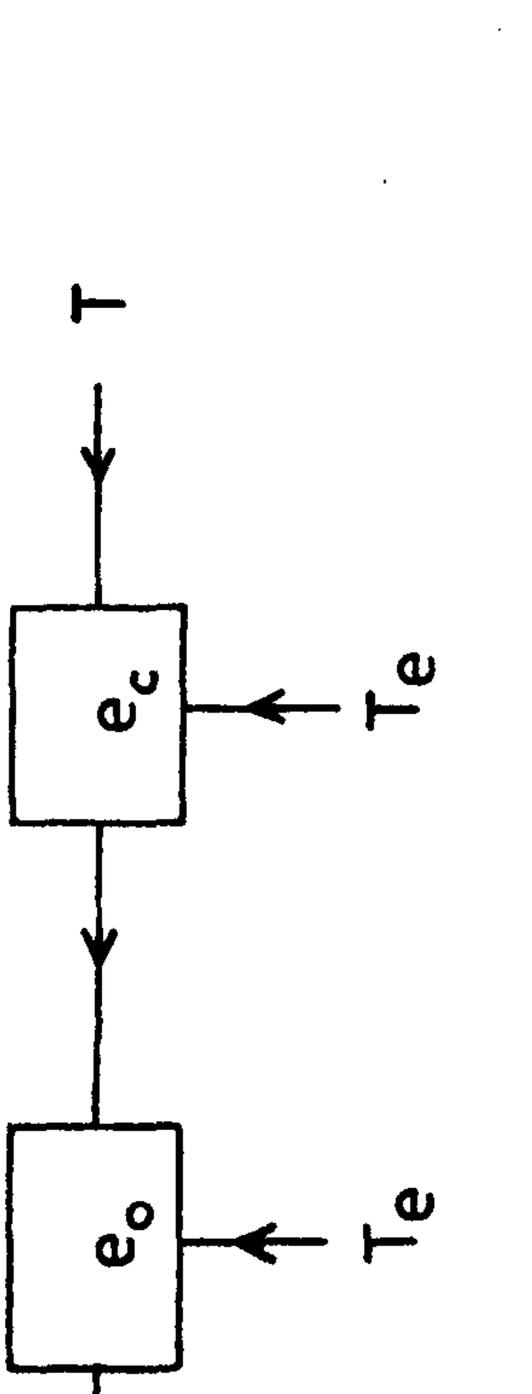

SKY – EMISSION OBSERVATIONS

Fig. 39a

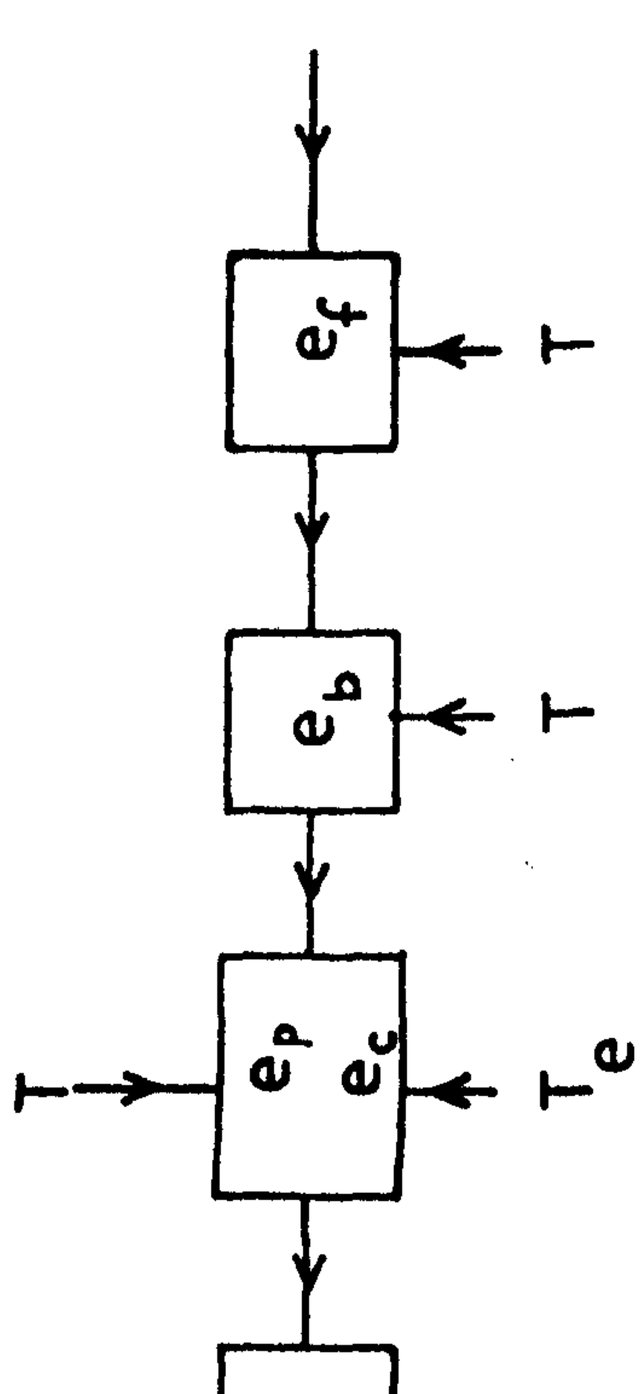

PLANETARY OBSERVATIONS

Fig. 39b

From the work described in section 2.6 we may expect that, if u = 1.5, and the radiation wavelength is 1.32 mm then, from Table 2.6.1. $e_c = (1-P_s) = 0.85$, and the observed value of C = 0.23 implies that $e_o = 0.90$.

A number of measurements were also made of the apparent brightness of the planets Jupiter and Saturn. These may also be used to check the calibration of the overall system performance.

Consider now Figure 39b. Here e_o and e_c are as defined above, $e_p = (1-P_f)$ is the fraction of the receiver beam that does not spill over the edge of the secondary onto the sky, e_b is the beam efficiency, and e_f represents the efficiency with which the source fills the main lobe of the antenna pattern.

With an essentially Gaussian main lobe the expression

$$e_f = \frac{(1 - \exp(-(a/b)^2))}{(1 - \exp(-(c/b)^2))} \qquad \ldots.(4.9)$$

provides a satisfactory approximation where, a, is the angular radius of the source, b, is the 1/e - power half-angle of the main lobe, and, c, is the angle from the beam axis to the first null in the antenna pattern.

From the program used in section 2.6 to predict the theoretical shape of the antenna pattern it was calculated that, for a telescope of the UKIRT geometry under the conditions discussed above, c/d = 2.076, hence if we assume the measured value of b = 45.3 "arc is correct then c = 94.0 "arc. We may therefore write

$$e_f = 1.0137 * (1 - \exp(-(a/45.3)^2)) \qquad \ldots.(4.10)$$

where, a, is in "arc.

Now, from Figure 39b we may write

$$T_c = T_e.(1-e_o.e_c) + T.e_o.e_c + T_x.(e_o.e_b.e_f.(e_c+e_p-1)) \quad ....(4.11)$$

If the telescope is pointed such that the centre of the source is at the beam axis then we may write

$$T_x(\text{Source}) = T + T_p.\exp(-D.\text{Sec}(z)) \quad ....(4.12)$$

where T_p is the temperature of the planetary source and T is the apparent brightness temperature of the sky in the direction of observation.

If the telescope is now re-directed to observe a position on the sky a few main lobe diameters from the planetary source the contribution due to T_p vanishes and $T_x(\text{Sky})$ is equivalent to T. Hence the measured change in T_c when nodding the telescope on and off the source, T_d, may be given by

$$T_d = T_p.\exp(-D.\text{Sec}(z)).(e_o.e_b.e_f.(e_c+e_p-1)) \quad ....(4.13)$$

By observing the apparent sky temperature, T_z, just off source, we may use the measured values of C and T_e to obtain T from expression 4.7, and, as

$$T = T_{sky}.(1 - \exp(-D.\text{Sec}(z))) \quad ....(4.14)$$

it follows that

$$T_d = T_p.(1-(T/T_{sky})).(e_o.e_b.e_f.(e_c+e_p-1)) \quad ....(4.15)$$

This method was employed for estimating the sky absorption as it is probable that the optical thickness of the atmosphere will vary both with time and direction in a way that is not fully described by the sky dip measurements given in Table 4.1. The quoted values of T are based upon T_z measurements made by looking essentially in the source direction at the time of each planetary observation. They may therefore be taken as a more reliable guide than the measurements of D to the actual sky absorption in the line of sight during the observations.

It was not possible to open the dome until just before Sunset in order to avoid thermal stress affecting the telescope's alignment. As both Jupiter and Saturn were at that time only a few hours behind the Sun this means that the planetary observations were made when each planet was near to setting. The relatively high values of T listed in the tables of planetary data reflect the large zenith angles at which the observations were made.

By consulting the explanatory notes for the Astronomical Ephemeris we may say that the equatorial and polar semi-diameters of Jupiter, a_e, and a_p, are such that

$$a_e = 98.47/d \quad ; \quad a_p = 91.91/d$$

where d is the distance between Jupiter and The Earth in Astronomical Units, and each semi-diameter is in "arc.

The radius, a, of the circular disc which would subtend the same solid angle as this ellipse is, therefore, given by

$$a = (a_e.a_p)^{\frac{1}{2}} = 95.13/d \qquad \ldots.(4.16)$$

From the work described in section 2.6 we may say that, under the conditions relevant here, that $e_c = 0.85$, $e_b = 0.86$

and e_p = 0.89, hence - given values for T_d, T, and d - we may obtain a value for the planetary temperature, T_p.

Table 4.2 lists the results of the observations made upon the planet Jupiter. The values for d were obtained from the Astronomical Ephemeris.

Table 4.2. Observations of the planet Jupiter.

DATE	d (a.u.)	a "	e_f	T_d (^oK)	T (^oK)	T_p (^oK)
24th	5.8131567	16.36	0.1240	7.4	95.2	160.4
25th	5.8270792	16.32	0.1234	6.9	100.8	155.0
26th	5.8408945	16.28	0.1228	7.4	91.3	158.5
27th	5.8546006	16.25	0.1224	6.0	107.4	140.9
30th	5.8950421	16.14	0.1209	6.2	125.2	165.4
Estimated Error		$\pm$ .02	$\pm$5%	$\pm$0.25^oK	$\pm$5^oK	$\pm$12^oK

The mean value of T_p which may be obtained from the above results is 156 ^oK with a scatter of $\pm$ $9\frac{1}{4}$ ^oK.

A number of measurements of planetary temperatures at various wavelengths have been published. Some of the more recent of these have been collected into a survey covering the 0.1 mm to 10 mm wavelength range by Whitcomb, et al (Icarus 38 75 (1979)). Each of the results obtained at wavelengths shorter than 2 mm have been obtained by a bolometric comparison of the planet under observation with Mars, and it was then assumed that the Martian temperature was as predicted from a theoretical model published by Wright(Astrophys. J. 210 250 (1976)).

From the survey mentioned above the three most recent measurements of Jupiter's temperature at wavelengths close to 1.3 mm are: 162 $\pm$ 8 ^oK at 0.8 mm wavelength(Whitcomb, et al, ibid); 168 $\pm$ 8 ^oK at 1.0 mm wavelength(Werner, et al, Icarus 35 289 (1978)); 159 $\pm$ 9^oK at 1.4 mm wavelength(Courtin,et al, Astron. Astrophys. 60 115 (1977)). Averaging these figures produces a

value of $T_p = 163 \pm 8\ ^{o}K$.

The value of T_p produced by averaging the results given in Table 4.2. was obtained by calibration against local reference sources whose temperatures were known. Hence the value obtained - unlike those described by Whitcomb, et al(ibid) - does not depend upon an assumed temperature for Mars. The result does, however, rely upon the values calculated for e_p, e_c, e_b, e_f, and the value of e_o obtained from the sky dips listed in Table 4.1. As such, the value obtained for T_p may be regarded as a novel radiometric measurement based upon being able to accurately predict the system performance rather than calibrating it by reference to a source of assumed temperature outside the atmosphere.

A number of observations were also made of the planet Saturn. The results of these are collected in Table 4.3.

Table 4.3. Observations of the planet Saturn.

DATE	T_d (^{o}K)	T (^{o}K)	a "	e_f	T_p (^{o}K)
24th	2.0	100.2	8.17	0.0324	172.8
25th	1.5	94.6	8.16	0.0324	125.4
26th	1.5	90.1	8.14	0.0322	123.0
27th	1.5	98.3	8.13	0.0321	129.2
29th	1.6	99.1	8.10	0.0319	135.8
30th	1.2	111.5	8.08	0.0317	114.5
Est. Err.	$\pm$.25^{o}K	$\pm$5^{o}K	$\pm$0.01	$\pm$5%	$\pm$25^{o}K

The results listed in this table were obtained in the same way as those given in Table 4.2.

From the observations it may be concluded that $T_p = 133 \pm 25\ ^{o}K$ for Saturn at a wavelength of 1.32 mm. The uncertainty in this figure is much greater than is the case for Jupiter as the detected signal, T_d, is relatively small. This is mainly due to the smaller angular diameter of the source. At the time

the observations were made the Earth was close to its passage through the plane of Saturn's rings(transit occurred on 23rd July 1980)and hence the contribution due to the rings may be regarded as negligible. The result obtained above appears to be in satisfactory agreement with the value of $T_p = 145 \pm 7$ ^{o}K published by Werner, et al(ibid)following observations at 1 mm wavelength.

In addition to the planetary observations discussed above, observations were also made of a number of molecular clouds at various radiation wavelengths. The data collected during these observations are at present being examined by R. Padman and R.E. Hills of the Cavendish Radioastronomy Observatory, Cambridge, and L. Little of the University of Kent at Canterbury. Papers are in preparation as a result of this work.

Figure 40 illustrates the typical form of the output data from one of the four channels of the digital autocorrelator employed with the receiver to obtain spectral information. The graph shows the effective velocity distribution of CO molecules along a line of sight into the radio source M17.

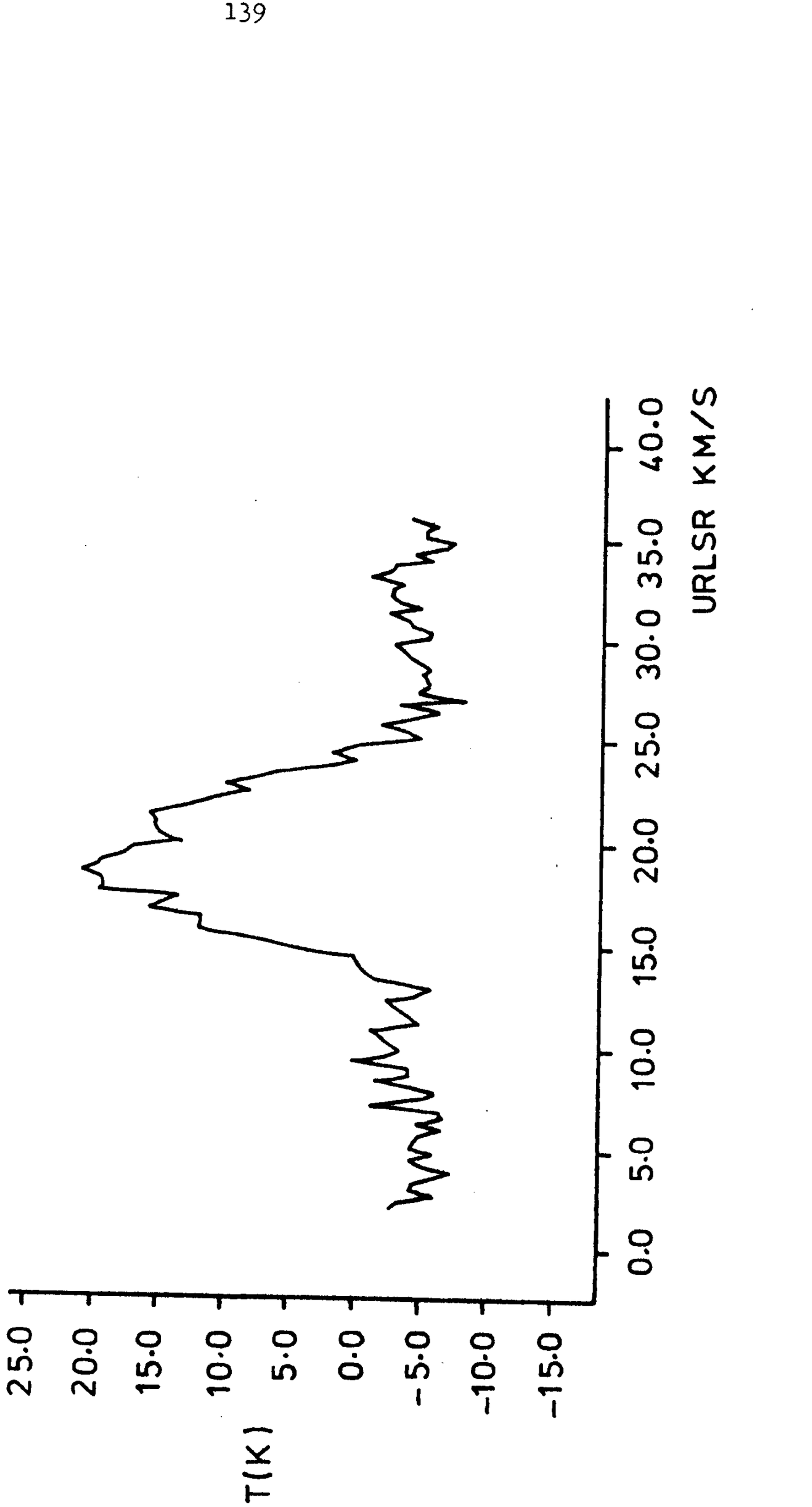

Fig. 40.
CO spectrum from M17.

5. Conclusion.

In order to be able to design a satisfactory Quasi-Optical receiver system it was first necessary to develop the theory of Gaussian beam modes in an appropriate way. Once this was done a Quasi-Optical system was designed to achieve the desired optimum performance. Two such systems were designed and constructed, and their performance was examined both in the laboratory and on the UKIRT. In this way it was established that the systems performed essentially as intended, and from the results given in sections 3 and 4 of this thesis it may be inferred that the Gaussian theory developed in section 2 provides an adequate description of the manner in which such a system operates upon a coherent paraxial beam.

It was then possible to employ the Quasi-Optical receiver system on UKIRT to obtain temperatures for sources whose angular dimensions were known without recourse to a reference source outside the atmosphere. This method was used as described in the previous section of this thesis to obtain temperatures for Jupiter and Saturn which are in agreement with those published by other workers as a result of bolometric comparisons with the planet Mars. A number of observations of molecular clouds were then successfully undertaken using the receiver, and the results of these observations are currently being prepared for publication.

Following the work described in this thesis the Quasi-Optical system initially desgined for use on UKIRT has been also used as part of a radiometer system assembled to measure the atmosperic extinction at 1.3 mm wavelength above Roque De Los Muchachos, La Palma. These measurements were made as part of the site-testing

for the Millimetre-Wave Telescope. The results of these observations are expected to be published in due course.

A third Quasi-Optical system has also been designed by the use of the methods described in section 2 to operate upon paraxial beams with less than half the radius of those passing through the two systems described above. This compact system has been produced in order to explore just how small such a Quasi-Optical system can be made whilst maintaining a satisfactory performance. In this way it is also hoped to investigate the limits to the range of application of the Gaussian beam mode approach.

References.

Alvarez, J.A., et al Infra. Phys. 15 45 (1975)

Arnaud, J.A., I.E.E.E. MTT-22 486 (1974)

Arnaud, J.A., Beam and Fibre Optics. Academic Press, New York, 1976

Aubry, C., & Bitter, D., Elect. Lett. 11 154 (1975)

Ayers, S., et al Proc. I.E.E. 121 1447 (1974)

Barrow, W.L., & Chu, L.J., Proc. I.R.E. 27 51 (1939)

Barrow, W.L., & Lewis, F.D., Proc. I.R.E. 27 41 (1939)

Bodnar, D.G., & Bassett, H.L., I.E.E.E. AP-23 841 (1975)

Born, M., & Wolf, E., Princples of Optics. Pergamon Press, London, 4th Ed., 1970

Boyd, G.D., & Gordon, J.P., Bell System Tech. J. 40 489 (1961)

Boyd, G.D., & Kogelnik, H., Bell System Tech. J. 41 1347 (1962)

Chantry, G.W., et al Infra. Phys. 9 31 (1969)

Chantry, G.W., et al Infra. Phys. 11 109 (1971)

Clarricoats, P.J.B., & Saha, P.K., Proc. I.E.E. 118 1167 (1971)

Clarricoats, P.J.B., & Saha, P.K., Proc. I.E.E. 118 1177 (1971)

Costley, A.E., et al I.E.E.E. Proc. 2nd Int. Conf. Submillimetre Waves & their Applications. Dec. 1976

Courtin, R., et al Astron. Astrophys. 60 115 (1977)

Cronin, N.J., et al Infra. Phys. 18 731 (1978)

Erdyli, A., et al Tables of Integral Transforms. Vol. 1, Bateman ms Proj., McGraw-Hill, New York, 1954

Erickson, N.R., I.E.E.E. MTT-25 865 (1977)

Fox, A.G., & Li, T., Bell System Tech. J. 40 435 (1961)

Goubau, G., & Scwering, F., I.R.E. Trans. AP-9 248 (1961)

Jones, E.M.T., & Cohn, S.B., J. Opt. Soc. Am. 26 452 (1955)

King, A.P., Proc. I.R.E. 38 249 (1950)

Kogelnik, H., Proc. Symp. Quasi-Optics. Polytechnic Press, New York, 333 (1964)

Kogelnik, H., & Li, T., Proc. I.E.E.E. 54 1312 (1966)

Kraus, J.D., Radio Astronomy. McGraw-Hill, London, 1966

Lamb, H., Proc. London Math. Soc. 29 523 (1898)

Larsen, T., I.R.E. Trans. MTT-10 191 (1962)

Lewis, E.A., & Casey, J.P., J. Appl. Phys. 23 605 (1952)

Loefer, G.R., et al Microwaves 15(5) 58 (1976)

Loewenstein, E.V., et al Appl. Opt. 12 398 (1973)

Martin, D.H., & Lesurf, J.C.G., Infra. Phys. 18 405 (1978)

Martin, D.H., & Puplett, E., Infra. Phys. 10 105 (1969)

McKnight, R.V., & Moller, K.D., J. Opt. Soc. Am. 54 132 (1964)

Ohtera, I., & Ujiie, H., I.E.E.E. AP-23 858 (1975)

Payne, J.M., & Wordman, M.R., Rev. Sci. Ins. 49 1741 (1978)

Peck, E.R., J. Opt. Soc. Am. 52 253 (1962)

Russell, E.E., & Bell, E.E., J. Opt. Soc. Am. 57 341 (1967)

Schelkunoff, S.A., Electromagnetic Waves. Van Nostrand, New York, 1943

Smith, D.R., & Loewenstein, S.V., Appl. Opt. 14 1335 (1975)

Thomas, B. MacA., I.E.E.E. AP-26 367 (1978)

Werner, M.W., et al Icarus 35 289 (1978)

Whitcomb, S.E., et al Icarus 38 75 (1979)

Wright, E.L., Astrophys. J. 210 250 (1976)